UNIVERSITY OF OKLAHOMA

GRADUATE COLLEGE

EFFECT OF PRESSURE DEPLETION ON HYDROCARBON RECOVERY IN NATURALLY FRACTURED RESERVOIRS

A DISSERTATION

SUBMITTED TO THE GRADUATE FACULTY

in partial fulfillment of the requirements for the

degree of

Doctor of Philosophy

By

ABEL CHACON
Norman, Oklahoma
2006

UMI Number: 3238432

ProQuest Information and Learning Company
300 North Zeeb Road
P.O. Box 1346
Ann Arbor, MI 48106-1346

EFFECT OF PRESSURE DEPLETION ON HYDROCARBON RECOVERY IN NATURALLY FRACTURED RESERVOIRS

A DISSERTATION APPROVED FOR THE
MEWBOURNE SCHOOL OF PETROLEUM AND GEOLOGICAL ENGINEERING

BY

Dr. Djebbar Tiab, Chair

Dr. Chandra Rai

Dr. Samuel Osisanya

Dr. Jean-Claude Roegiers

Dr. Roger Slatt

DEDICATION

To my lovely wife, Gloria, and my dear son, Abel Eduardo.

To my grandmother (Gregoria), my parents (Octavia and Juan), my sister, (Maribel), and my brothers (Juan Antonio and Julio (RIP)).

ACKNOWLEDGEMENTS

I wish to express my gratitude to Dr. Djebbar Tiab for his continuous support, encouragement and guidance during my graduate studies at the University of Oklahoma. I would also like to thank Dr. Chandra Rai, Dr. Samuel Osisanya, Dr. Jean-Claude Roegiers, and Dr. Roger Slatt for their valuable contributions and willingness to serve as members of my doctoral committee.

I am, of course, indebted to the Distance Learning Programs (Algerian Program) at the Mewbourne School of Petroleum and Geological Engineering for its generous financial support during my years of study at the University of Oklahoma.

This research was carried out in part using hardware and software provided generously by the following companies: BP America (computing resources, and PIE®), Petroleum Experts (MBAL®), and Kappa Engineering (Saphir®).

Furthermore, I would like to thank the Society of Exploration Geophysicists (SEG), the Society of Petroleum Engineers (SPE), Editions Technip, Gulf Publishing Company, Elsevier, Dr. Djebbar Tiab, Dr. Robert W. Zimmerman, Dr. Roger Slatt, Dr. Carl Sondergeld, and Dr. Chandra Rai for their written permissions to reproduce material copyrighted to them in this dissertation.

Special recognitions go to my friends, Fabio Alberto González, Doris González, Brian Arias, Dora Restrepo, Tomás Correa, Oscar Uribe, Katharine Moncada, and Freddy Humberto Escobar for their continuous support and encouragement to finish my doctoral studies.

Finally, I would also like to acknowledge the assistance and support provided by Jeff Wedgwood, my supervisor at BP America.

TABLE OF CONTENTS

LIST OF TABLES

LIST OF FIGURES

ABSTRACT

This study analyzes the effects of stress on several properties of naturally fractured reservoirs (NFRs), e.g. fracture and matrix compressibility, fracture and matrix porosity, permeability in NFRs, and its implications on hydrocarbon recovery.

Modeling and current methods to identify and characterize NFRs from seismic and well test data are briefly discussed. In NFRs fluids are stored inside the matrix pore space and inside the fractures of the rock. The parameter indicating the volumetric fraction of fluids deposited inside the fractures is the storage capacity ratio, which is the function of the fracture and matrix porosity, and fracture and matrix compressibility. Since it is very difficult to obtain these values, it is generally assumed that the matrix and the fracture compressibilities are equal, which induces a big uncertainty in the estimation of the storage capacity ratio as well as an inaccurate estimation of the volume of fluids inside the fractured rock.

The link between well test analysis, the material balance equation, and the elastic properties of the rock resides in the fluid storage capacity. Thus, in this study, the influence of stress on the mechanical behavior of the fractured rock, and its effect on the rock properties such as permeability, porosity and compressibility is analyzed using the bulk modulus and normal compliance of the fracture which are elastic

properties. The influence of stress on the mechanical behavior of the fractured rock and its effect on several rock properties can be obtained from core analysis or multi-component seismic interpretation, which is linked to well test analysis and the material balance equation through the storage capacity ratio equation. Furthermore, an example using real data from a pressure buildup test explaining the proposed well test analysis technique is included. In addition, a method to compute the fracture and matrix compressibility from the integration between well test analysis and the mechanical behavior of the rock is also presented.

Finally, the effects on hydrocarbon recovery due to differences in fracture and matrix compressibilities, and the effect of changes in the in-situ effective stress of the rock caused for depletion are incorporated into the material balance equation.

1 INTRODUCTION

Well test analysis has been one of the most basic tools to characterize and quantify properties such as permeability, storage capacity ratio and the interporosity flow parameter in naturally fractured reservoirs. This study, which is a reservoir characterization issue that integrates several geosciences such as: Petrophysics, Rock Mechanics, Seismic, Geophysics, Reservoir Engineering, and Production Engineering to research the effect of stress on several rock properties: permeability, compressibility, and porosity of naturally fractured reservoirs.

The document has been divided into six sections. The first section, Chapter One, presents the basis for classifying, detecting and modeling naturally fractured reservoirs. The second section, chapters two and three, presents contributions in fracture porosity and fracture permeability determination, and the stress influence on those properties. The third section, Chapter Four, presents a brief summary on the current available well test analysis techniques for naturally fractured reservoirs. The fourth section of this study, Chapter Five, describes the main concepts to develop a proposed pressure transient analysis technique to determine the reservoir fracture characterization parameters. Furthermore, the link between the elastic properties, well test analysis and the stress influence are also discussed in detail. Chapter Six, which is the fifth section of this study, presents a real pressure build up example in which a step by step procedure explains the developed pressure transient analysis technique. In the last section, Chapter Seven, the material balance equation is solved for gas, undersaturated, and saturated naturally fractured reservoirs. As a result, new plotting schemes were developed to compute the original hydrocarbons in place and study the effects of depletion on the recovery factor in NFRs using production data, and the storage capacity ratio obtained from pressure transient analysis.

1.1 CLASSIFICATION OF NATURALLY FRACTURED RESERVOIRS

The following paragraphs present a brief summary of the classification that Tiab and Donaldson[1] compiled in their Petrophysics book.

1.1.1 Geological Classification of Naturally Fractured Reservoirs

This classification is based upon fracture patterns corresponding to paleostress conditions and strain distribution in the reservoir at the time of the fracturing process.

1.1.1.1 Classification Based on Stress/Strain Conditions

Stearns and Friedman[2] classified the fractures in: a) shear fractures, when the stresses in the principal directions are compressive, and b) extension fractures, when they are formed perpendicular to the minimum stress direction.

1.1.1.2 Classification Based on Paleostress Conditions

This classification is based on geological conditions such as: **a) tectonic fractures**, their orientation, distribution and morphology are associated with local tectonic events; **b) regional fractures**, which do not show evidence of offset across the fracture plain and are always parallel to the bedding surfaces, and; **c) contractional fractures**, which result from bulk volume reduction of the rock.

1.1.2 Engineering Classification of Naturally Fractured Reservoirs

Based on the extent to which fractures have altered the porosity and permeability of the reservoir matrix, Nelson[3] identified the following four types of naturally fractured reservoirs: **a) type 1**, fractures provide all the reservoir storage capacity and permeability; **b) type 2**, the matrix already has very good permeability, and the fractures improve the average reservoir permeability; **c) type 3**, the matrix has negligible permeability but contains almost all of the hydrocarbons, and; **d) type 4**, the fractures are filled with minerals, which generally these reservoirs are uneconomic to develop and produce.

Belharche[4] presented the following table, which summarizes Nelson's[3] classification:

Table 1.1. Engineering classification of naturally fractured reservoirs.

Reservoir type	Problems and opportunities
Type 1: Productivity essentially derived from fracture porosity and permeability alone.	• It is necessary to have fracture intensity or high fracture porosity for economic reservoir. • May result in early water breakthrough the timing of which is governed by fracture height and vertical connectivity. • Water influx is often accompanied by rapid oil decline. • Fractures may generate production from otherwise unproductive rock. • Determination of fracture porosity is critical in determining recovery.
Type 2: Fractures provide essential reservoir permeability. Hydrocarbons stored in matrix and fractures but fractures provide the means to flow (i.e. permeability).	• Primary and secondary recovery efficiency is highly dependent upon how well the matrix is exposed to the fracture network. • Possible early water breakthrough and rapid oil decline. • Development patterns must consider the reservoir heterogeneities (e.g. matrix-fracture communication may vary aerially). • Fracture intensity and dip must be known before pursuing development. • Fractures improve productivity from poor deliverability reservoirs. • Determination of fracture permeability and heterogeneity is critical in accessing effective parameters and recovery potential.
Type 3: Productivity of a permeable matrix is enhanced with the additional fracture permeability.	• There can be unusual responses in secondary recovery. • Drainage area can often be elliptical. • It may be difficult to recognize or detect the fracture system. • Fractures may enhance already commercial opportunities. • Determination of fracture permeability and heterogeneity is critical (as for Type 2 reservoirs).
Type 4: Fractures do not contribute to porosity or permeability, but barriers act as flow.	• Recovery is poor due to severe reservoir compartmentalization. • If properly planned, field development could be optimized. • Can have very poor secondary recovery because of compartmentalization.

1.2 MODELING OF NATURALLY FRACTURED RESERVOIRS

The increased exploration and development of fractured reservoirs, which has been helped with the development of more powerful computers, have driven engineers to mathematically model naturally fractured reservoirs. This chapter has a brief description of the most models utilized during the last five decades to describe the flow through dual porosity media.

1.2.1 Single Porosity Models

These models are used to simulate reservoirs where all the storage capacity is assumed to reside in the fractures; such as in type 1 naturally fractured reservoirs. They also can be applied in fractured reservoirs where interporosity flow between a porous matrix and the fractures is an important factor. For example, Argawal *et al*.[5] simulated with a single porosity model, a giant fractured reservoir in the North Sea by selecting an appropriate model for fluid exchange between the matrix and the fracture, while preparing the pseudorelative permeability curves using a dual porosity model.

1.2.2 Dual Porosity Models

These models are used to simulate reservoir systems composed of two different types of porosity, matrix and fracture that coexist in a rock volume. It is usually assumed that the matrix consists of a set of porous rock systems that are not connected to each other, have a low transmissibility and have a high storage capacity. Furthermore, it also assumes that the fracture system has low storage capacity, high transmissibility and it interconnects the porous media. Normally, it is assumed that the matrix provides the fluids to the fractures, and the fractures transport the fluids to the well. As shown in Figure 1.1, different idealizations of the matrix/fracture geometry have been proposed such as the sugar cube model by Warren and Root[6], parallel horizontal fractures by Kazemi[7] and match-stick column models by Reiss[8]. The multi-porosity model proposed by Abdassh and Ershaghi[9] is a variation of the dual porosity model, which assumes a fracture set that interacts with two groups of matrix blocks with different porosities and permeabilities.

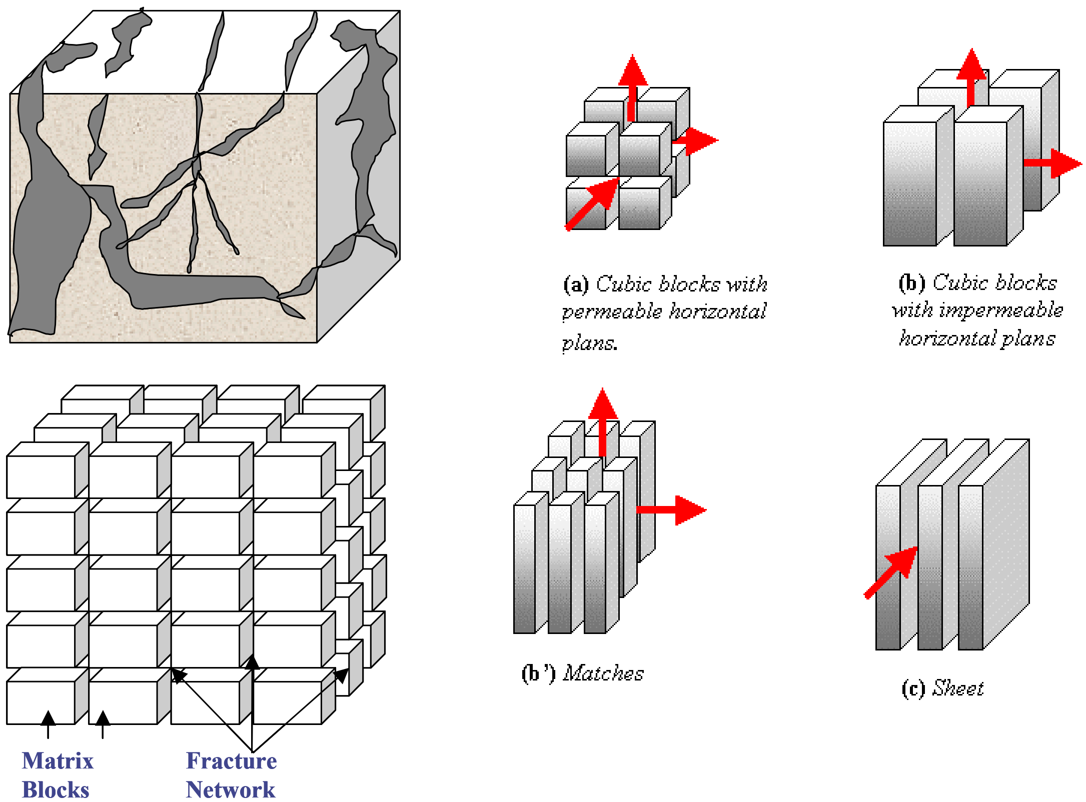

Figure 1.1. Dual porosity models.
(Source of the figure: references 6, 7 and 8)

Several techniques have been developed to detect and characterize naturally fractured reservoirs. The most prominent techniques are based on seismic interpretation, mud log data, core analysis, well logging and well test analysis. The following paragraphs present a brief description of each technique.

1.2.3 Detection from Seismic Data

The detection from seismic data takes advantage of physical properties such as splitting of the shear waves due to polarization of the shear sound waves and azimuthal anisotropy due to aligned fractures.

Figure 1.2 presents an example of a seismic profile taken from the Emeraude Field (offshore Congo). The seismic profile distortion around Well N shows that this portion of the reservoir is naturally fractured. Core, production, and pressure transient analyses evidences show that Well N, is located in a highly naturally fractured zone of the reservoir and has a high productivity (PI=175m^{3}d/bar). However, wells M and O do not present evidence that they are located in a fractured portion of the reservoir, and thus have lower productivity indexes (24 and 10m^3/d/bar respectively) than Well N.

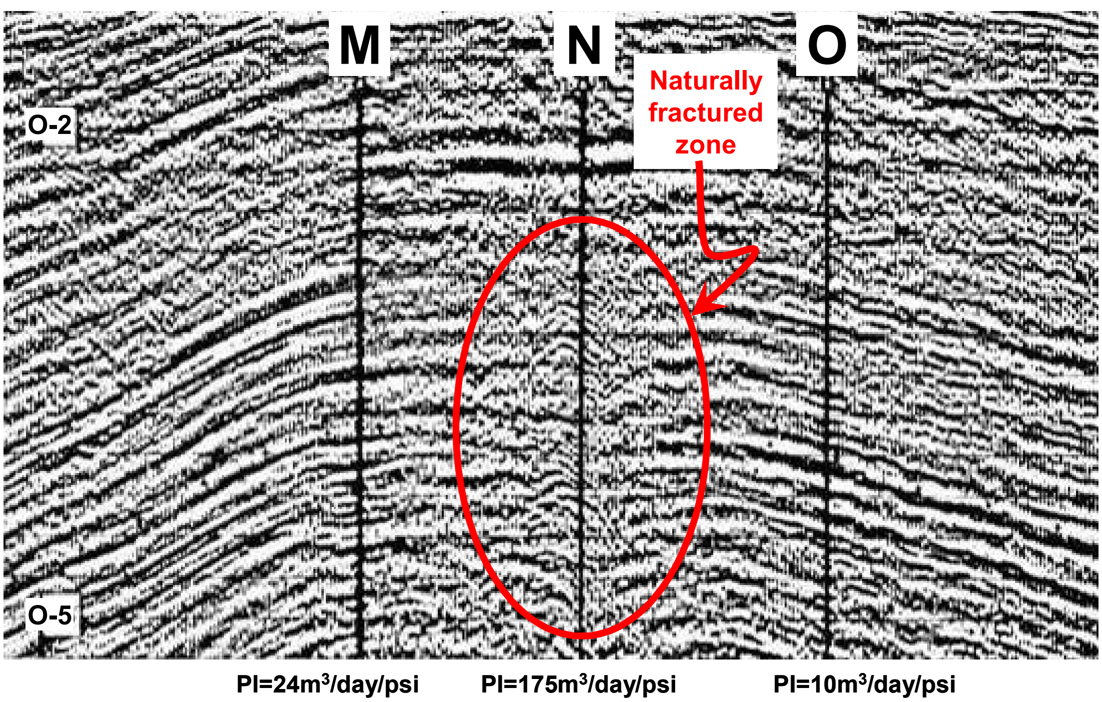

Figure 1.2. Example of seismic profile detecting fractures (Emeraude Field, Congo). (After Reiss[8])

1.2.3.1 Shear Wave Splitting

Shear wave velocities in anisotropic media split into two waves, fast and slow s-waves as shown in Figure 1.3. The fractional difference between the velocities of split shear waves at vertical incidence (Thomsen's coefficient γ) is close to the crack density. Technologies developed during the last few decades are designed to obtain γ from the difference in shear-wave travel times and normal incidence amplitudes.

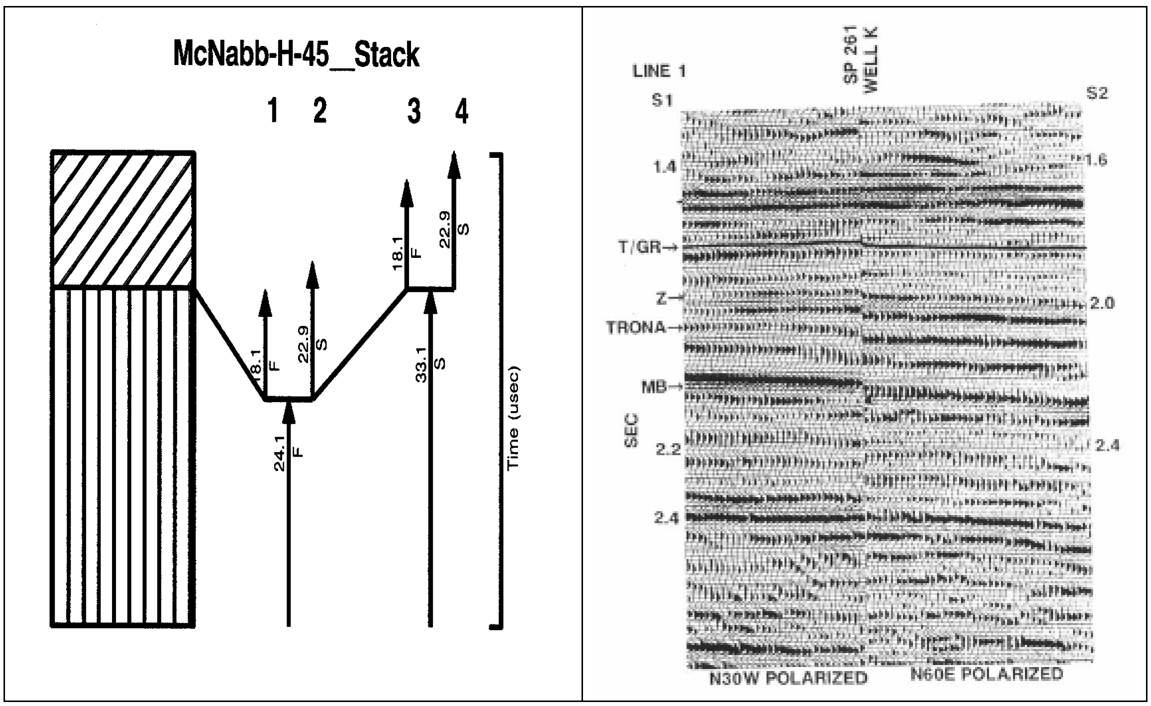

Figure 1.3. Splitting of the shear wave.
(Left, Sondergeld and Rai [10]) Inhomogeneous anisotropy. (Right, Lynn et al.[11]) S1 and S2 sections from S-wave reflection line 1, well K, showing first arriving shear wave polarized N30W.

The difficulty to acquire high quality shear data and its cost make it very important to obtain additional fractured reservoir information from 3-D P-wave data.

Amplitude variation with offset (AVO) is as a useful technique for characterization because it provides local information at the target horizon.

1.2.4 Using Amplitude Variation with Offset (AVO) for Fracture Detection

In 1988 Thomsen[12] presented a detailed analysis for the azimuthal anisotropy because of the presence of aligned fractures. Following Thomsen's analysis, Rüger and Tsvankin[13] presented a complementary study in which AVO was used to characterize naturally fractured reservoirs. Those studies can be summarized as follows:

1.2.4.1 Canonical Reflexion of the SH-Wave

The canonical reflection of the SH-wave survey can be represented as shown in Figure 1.4.

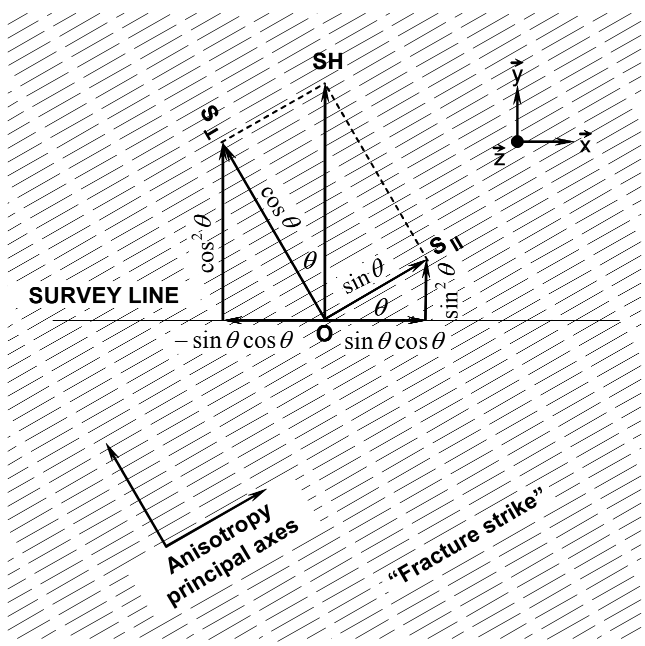

Figure 1.4. Map view of the canonical reflection problem for a SH-wave survey oblique to the anisotropy. (Thomsen[12]).

1.2.4.2 Reflection Coefficients and AVO

Considering the first order model of azimuthal anisotropy, which is conventionally used in shear wave birefringence experiments, and assuming parallel vertical fractures embedded in a homogeneous isotropic matrix, the model of horizontal transverse isotropy (HTI) presented in Figure 1.5 is obtained:

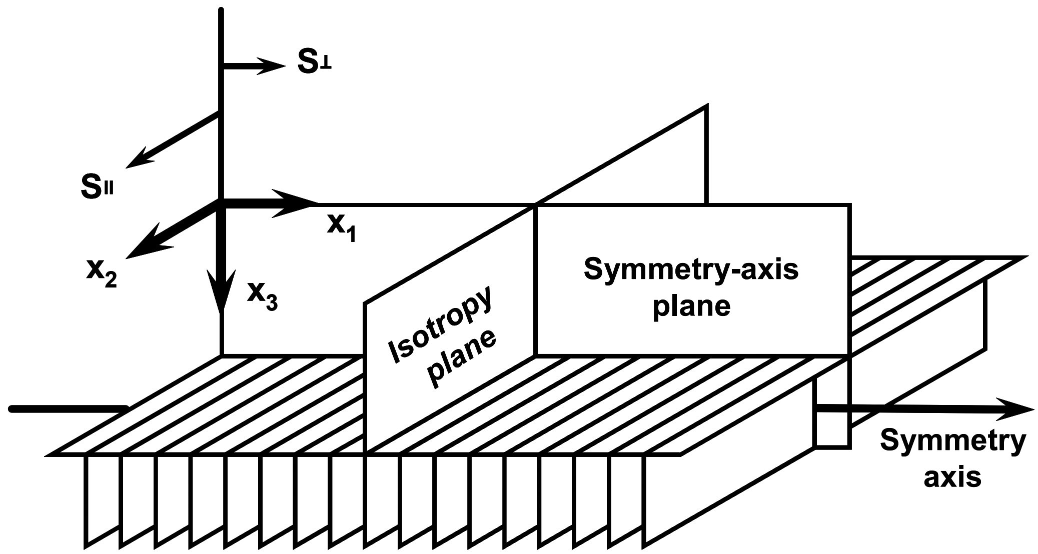

Figure 1.5. Sketch of an HTI model.
As indicated by the arrows, shear wave polarized parallel and normal to the isotropy plane have different velocities (Rüger and Tsvankin[13])

As indicated by the arrows, azimuthal anisotropy has a first order influence on shear waves that split into two components traveling with different velocities as shown in Figure 1.3.

1.2.4.3 P-waves in the Horizontal Transverse Isotropy (HTI) Media

From the HTI model presented in Figure 1.5, it is observed that waves confined to the plane normal to the symmetry axis (isotropy plane) do not experience any angular variation. However, in Figure 1.6 for all other vertical planes, the velocity does change with incidence angle, and it can vary with azimuth, complicating the interpretation.

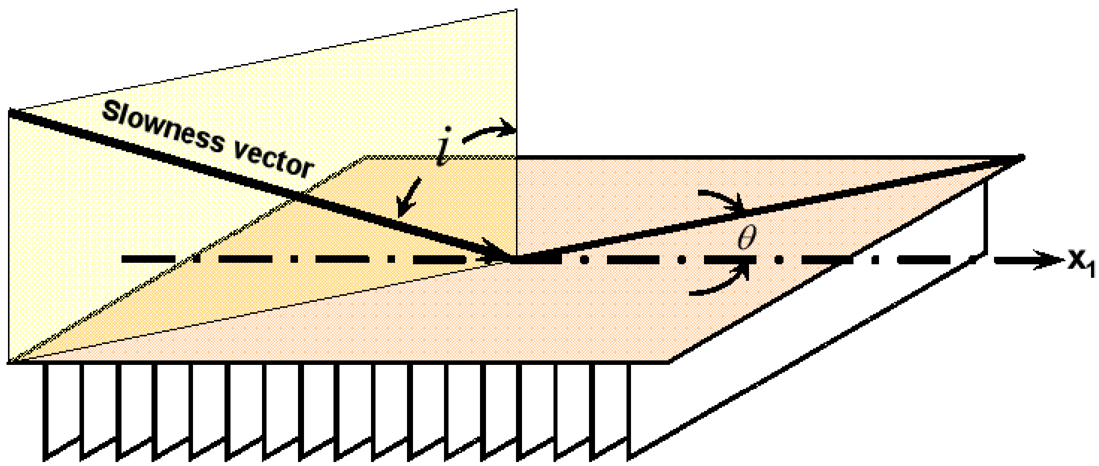

Figure 1.6. Horizontal transverse isotropy (HTI) model.
The angle between the slowness vector of the incident wave and vertical is denoted as i. The azimuthal angle ϕ is defined with respect to the symmetry axis pointing in the x_1-direction (Rüger and Tsvankin[13])

Figure 1.7 represents the p-wave propagation in the vertical plane containing the symmetry axis. Continuous and dashed white lines represent anisotropic and isotropic wave fronts.

It is very important to be aware that waves confined normal to the symmetry axis (isotropy plane) do not show any angular velocity variation.

Rüger and Tsvankin[13] found that AVO and normal moveout (NMO) in HTI are best described by adapting Thomsen's notation for transverse isotropy with a vertical symmetry axis (VTI media), instead of using the generic Thomsen's coefficients for HTI.

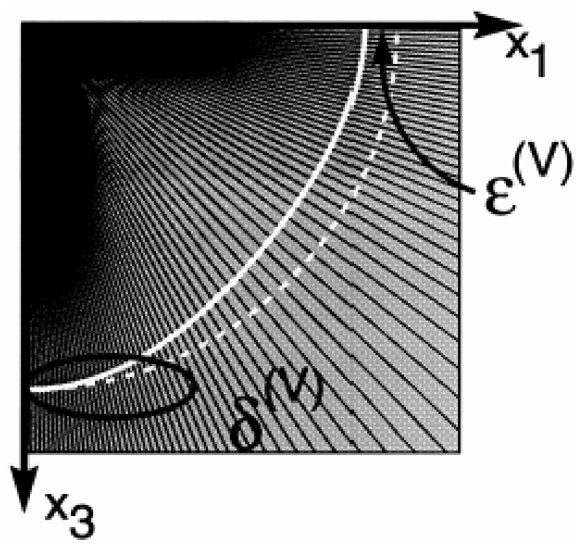

Figure 1.7. P-wave propagation in the symmetry axes plane of HTI media. Seismic rays are shown in black; the continuous and dashed white curves represent the anisotropic and isotropic wave fronts, respectively (Rüger and Tsvankin[13]).

1.2.4.4 Analysis of P-Wave Reflectivity

The reflectivity coefficient has the following form:

$$R_p(i,\phi) = \frac{1}{2}\frac{\Delta Z}{\overline{Z}} + \frac{1}{2}\left\{\frac{\Delta\alpha}{\overline{\alpha}} - \left(\frac{2\overline{\beta}}{\beta}\right)^2 \frac{\Delta G}{\overline{G}} + \left[\Delta\delta^{(V)} + 2\left(\frac{2\overline{\beta}}{\beta}\right)^2 \Delta\gamma\right]\cos^2\phi\right\}\sin^2 i + \frac{1}{2}\left\{\frac{\Delta\alpha}{\overline{\alpha}} + \Delta\varepsilon^{(V)}\cos^4\phi + \Delta\delta^{(V)}\sin^2\phi\cos^2\phi\right\}\sin^2 i\tan^2 i \tag{1.1}$$

Where:

$R_p(i,\phi)$ = reflectivity index as a function of the incidence and azimuthal angles.

i = incidence polar angle.

ϕ = azimuthal phase angle with the symmetry axis.

$Z=\rho\alpha$ = vertical p-wave impedance.

$G=\rho\beta$ = vertical shear modulus.

α = vertical p-wave velocity.

β= fast S-wave.

γ= shear wave splitting parameter.

$\varepsilon^{(V)}$ and $\delta^{(V)}$= Thomsen-style anisotropic coefficients, the superscript "*V*" emphasizes that the coefficients are computed with respect to the vertical and correspond to the equivalent vertical transverse isotropy (VTI) model that describes wave propagation in the symmetry-axis plane.

For an azimuth of 90^{o}, Equation 1.1 yields into the reflectivity coefficient in the isotropy plane.

1.2.4.5 P-Wave AVO Inversion

Equation 1.1 can be rewritten as:

$$R_p(i,\phi) = A + \left\{B^{iso} + B^{ani}\cos^2\phi\right\}\sin^2 i + \left\{C^{iso} + C^{ani_1}\cos^4\phi + C^{ani_2}\sin^2\phi\cos^2\phi\right\}\sin^2 i\tan^2 i \tag{1.2}$$

Equation 1.2 reveals that the existence of six coefficients determines the dependence of R_p on the incidence and azimuthal angle. Since it is difficult to extract reliable information from the term, $\sin^2 i \cos^2 i$, a two-term analysis concentrated in the AVO gradient that determines the low angle reflection response is done.

The AVO gradient measurement at an azimuth ϕ_j can be written as:

$$B(\phi_j) = B^{iso} + B^{ani}\cos^2(\phi - \phi_{sym}) \tag{1.3}$$

This equation determines that a minimum of three azimuthal measures of the AVO gradient are needed to find the orientation and AVO gradient. If the direction of the symmetry axis is known (from s-wave splitting analysis), Equation 1.3 becomes linear. In addition, with only two independent measurements of B, B^{iso} and B^{ani} can be obtained by plotting B vs. $\cos(\phi\text{-}\phi_{sym})$; the intercept of the straight line gives B^{iso} and the slope B^{ani}.

1.2.4.6 Combination of AVO and Moveout Data

The $\delta^{(V)}$ parameter in the gradient B^{ani} can be found from azimuthally dependent p-wave moveout data by comparing equations 1.1 and 1.2.

The normal moveout (NMO) velocity in a horizontal HTI layer is defined by:

$$V_{nmo}^2 = \alpha^2 \frac{1+2\delta^{(V)}}{1+2\delta^{(V)}\sin^2\phi} \tag{1.4}$$

Equation 1.4 describes an ellipse in the horizontal plane, where ϕ is the azimuth of the common mid point (CMP) line with respect to the symmetry axis. The equation contains three unknowns; therefore, three measurements of V_{nmo} for the vertical velocity, the axis orientation, and the parameter $\delta^{(V)}$ are required to solve it.

P-wave moveout can identify the crack orientation and obtain the parameter $\delta^{(V)}$ that is required for the AVO inversion, which gives two azimuthal measurements which is enough to obtain the AVO gradient and the shear-splitting parameter γ.

1.2.5 Detection from Mud Log Data

Dyke *et al.*[14] presented a discussion on reservoir characterization of naturally fractured reservoirs from mud log data. In Figure 1.8, Dyke *et al.*[14] concluded that loss of circulating fluid and increases in penetration rate during drilling are indicators that a cavernous formation has been penetrated.

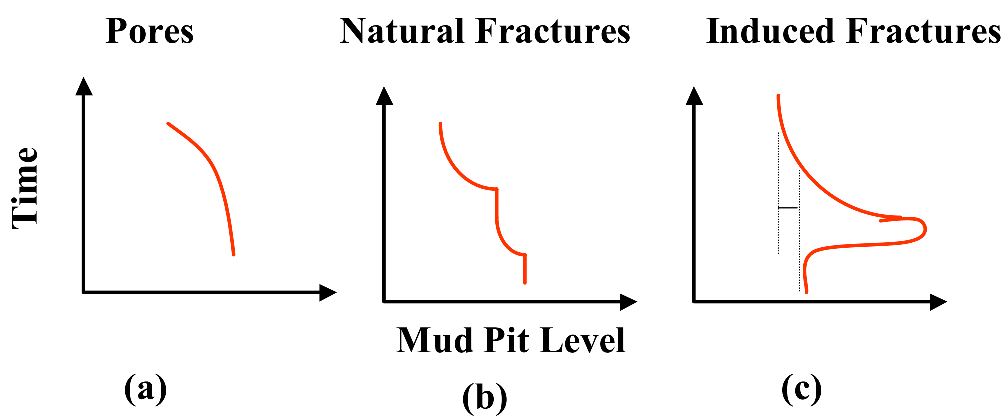

Figure 1.8. Mud loss indication and pit level behavior in pores, natural fracture, and induced fractures.
(a) Gradual buildup in loss ratio with pressure, (b) sudden start and exponential decline, and (c) loss can occur on increase in ECD as pumps are turned off/on (Dyke et al.[14])

1.2.6 Detection from Well Logs

Image tools are the most used well logging devices to identify fractures in the borehole. These tools are electrical, acoustic and density image logs; the most recognizable is the Schlumberger® tool FMI® (Fullbore Formation MicroImager).

The FMI® gives microresistivity formation images in water-base mud. The FMI® log is the preferred approach for determining net pay in laminated sediments of fluvial and turbidite depositional environments, and for visualizing sedimentary features. These features define important reservoir geometries and petrophysical reservoir parameters. The interpretation of image-derived sedimentary dip data lets us understand sedimentary structures and is very useful to detect and measure azimuth, dip angle and density of the fractures around the wellbore.

1.2.7 Detection from Core Analysis

Visual inspection of core samples gives an insight for the presence of fractures. Analyses similar to the FMI® can be done to determine azimuth and dip angle of the fractures at the borehole, see Figure 1.9.a.

Laboratory measurements of cores provide information about elastic rock properties, matrix porosity, matrix permeability and porosity partitioning coefficient (ratio between fracture porosity and total porosity).

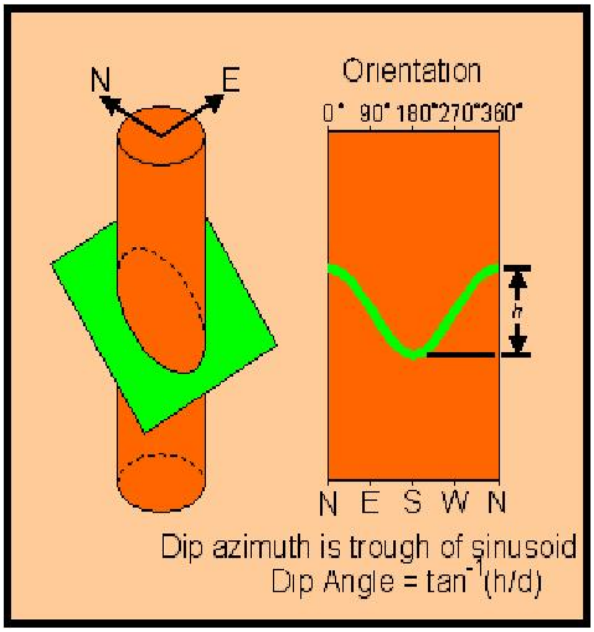

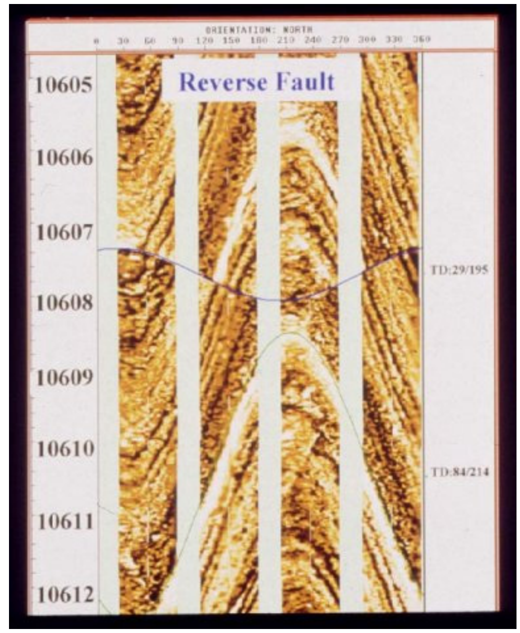

a) Schematic representation of measuring from borehole imaging.

b) Borehole image showing a fault cut through some thin sedimentary beds.

Figure 1.9. Fullbore Formation MicroImager (FMI®). (Slatt, R.[15])

Considerable care must be taken when describing fracture properties from cores; fractures induced by mechanical actions when coring or handling the samples can obscure the description. However, fractures parallel to the bedding plane should be excluded as they are generally caused by core handling. The following parameters are used to describe fractures (Reiss[8]):

a) Distance between fractures.

b) Dip and direction of the fracture plane.

c) Width.

d) Degree of cementation.

e) Length.

Oriented cores (or stereographic projection corrections) should be taken in order to estimate dip and direction of the fracture planes. Usually, width of the fractures is too small to be measured, and seldom obtained from core descriptions. Figure 1.10 presents the definition of the parameters used to describe cores, and Figure 1.11 shows an example of matrix element size determination from core description.

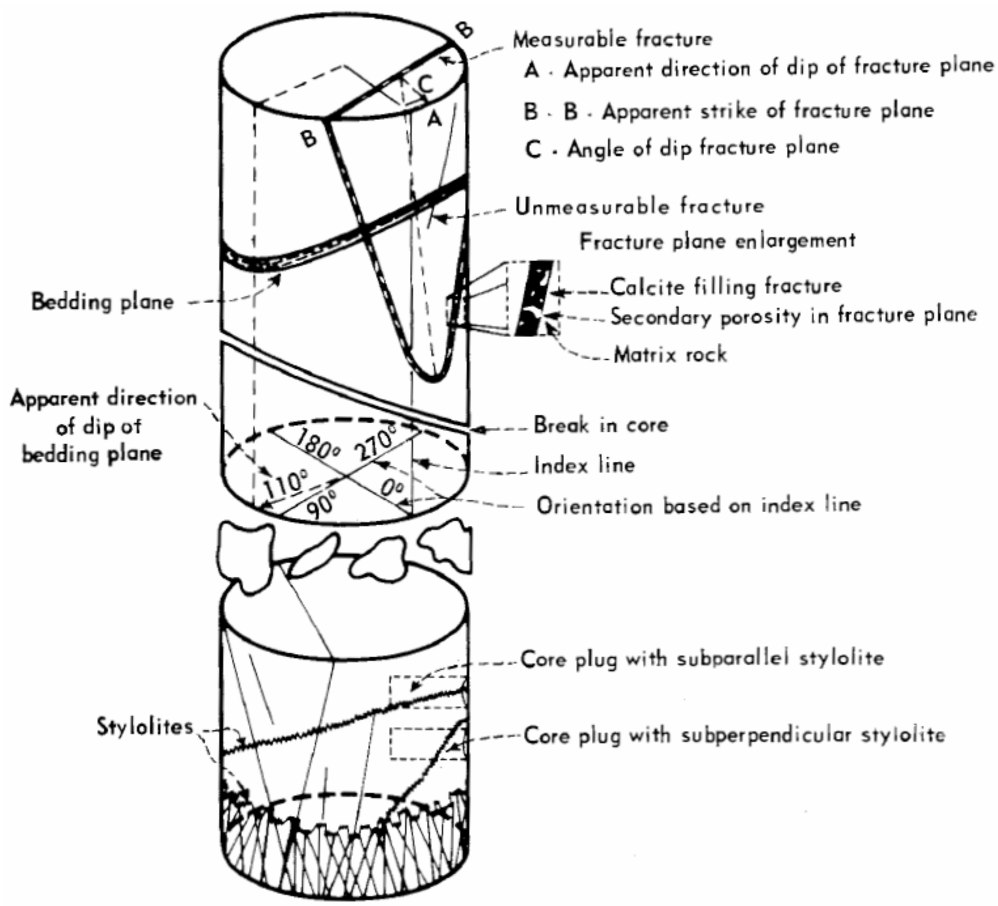

Figure 1.10. Definition of the parameters used to describe cores. (Reis[8])

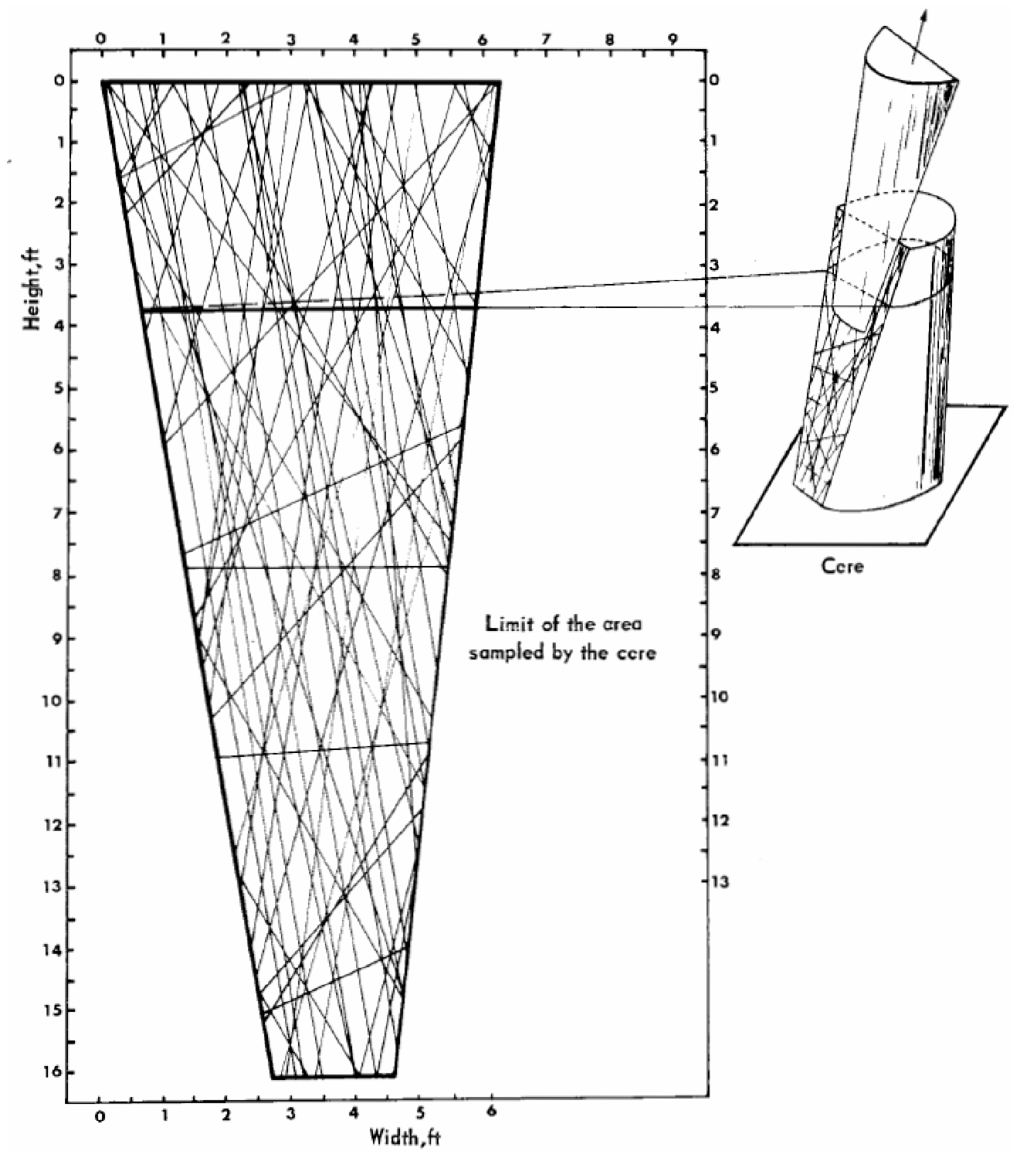

Figure 1.11. Analysis of matrix element size from core description. (Reiss[8])

2 FRACTURE POROSITY

2.1 DEFINITION OF FRACTURE POROSITY

Fracture porosity is defined as the ratio of the fracture volume with respect to the total volume.

From the sugar cube model represented in Figure 1.1, let us take a rectangular matrix block element of sides a_1, a_2, a_3 and fracture width b as shown in Figure 2.1.

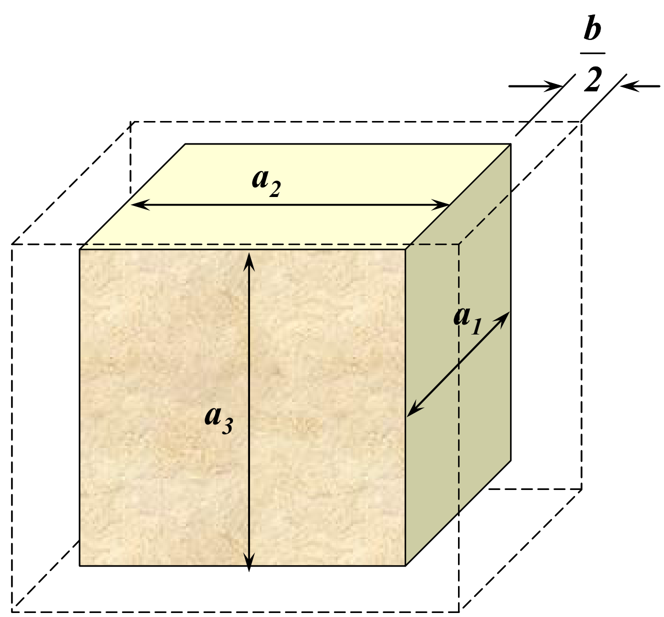

Figure 2.1. Fracture porosity definition.

Then fracture porosity is given by:

$$\phi_f = \frac{(a_1+b)(a_2+b)(a_3+b)-a_1a_2a_3}{(a_1+b)(a_2+b)(a_3+b)} \tag{2.1}$$

Since $b <<< a_1, a_2, a_3,$

$$\phi_f = b\left(\frac{1}{a_1}+\frac{1}{a_2}+\frac{1}{a_3}\right) \tag{2.2}$$

For each one of the dual porosity models presented in Figure 1.1, when $a_1=a_2=a_3$, Equation 2.2 yields:

Table 2.1. Fracture porosity for different models.

Model	**Fracture porosity**	**Matrix geometric constant**, ξ, in^{-1}
Cubes	$\frac{3b}{a}$	$\frac{3}{a}$
Cubes with two effective fracture planes	$\frac{2b}{a}$	$\frac{2}{a}$
Match-sticks	$\frac{2b}{a}$	$\frac{2}{a}$
Sheets	$\frac{b}{a}$	$\frac{1}{a}$

2.2 FRACTURE, MATRIX AND TOTAL POROSITY DETECTION FROM WELL LOGS

As Tiab and Donaldson[1] stated, porosity computed from the neutron log represents the combination of both, matrix and fracture porosity, $\phi_{Neu}=\phi_t$. However, the sonic log only measures the matrix porosity, $\phi_{Son}=\phi_m$. The fracture porosity can be obtained from:

$$\phi_f = \phi_t - \phi_m = \phi_{Neu} - \phi_{Son} \tag{2.3}$$

2.3 POROSITY PARTITION COEFFICIENT

The porosity partition coefficient, υ, represents the apportioning of total porosity, ϕ_t, between the matrix (intergranular) porosity, ϕ_m, and secondary pores (vugs, fractures, and fissures), ϕ_f. Tiab and Donaldson[1] presented Equation 2.4, which allows us to determine the porosity partition coefficient from resistivity and saturation measurements.

$$\nu = \frac{V_f}{V_t} = \frac{V_f}{V_f + \phi_m V_m} = \frac{\phi_f}{\phi_f + \phi_m} = \frac{\phi_f}{\phi_t} = \frac{R_w}{\phi_t (S_w - S_{xo})}\left(\frac{1}{R_t} - \frac{1}{R_{xo}}\right) \tag{2.4}$$

Where:

R_{xo} = borehole corrected invaded zone, short normal, resistivity, ohm-m.

R_{mf} = mud filtrate resistivity, ohm-m.

R_t = borehole corrected true, long normal, resistivity, ohm-m.

R_w = water resistivity, ohm-m.

ϕ_t = total porosity of the formation, fraction.

S_w = water saturation, fraction.

S_{xo} = saturation of mud filtrate in the flushed zone, fraction.

V_f = volume of the fracture space.

V_t = total pore volume.

V_m = bulk volume of the matrix.

The value of υ ranges between zero and unity for dual porosity systems, the absence of fracture porosity is represented by $\upsilon = 0$, and $\upsilon = 1$ indicates that the total porosity is equal to the fracture porosity (type 1 NFR).

If the total porosity is known from logs or core analysis, the matrix porosity can be estimated from:

$$\phi_m = \phi_t (1 - \nu) \tag{2.5}$$

From the Locke and Bliss[16] injectivity method, the fracture and pore volume of a sample can be estimated from the Cartesian plot of injection pressure versus volume of water injected into a core sample as presented in Figure 2.2. In this laboratory experiment, water is injected into a full-sized naturally fractured core sample while recording the injection pressure against the cumulative injected volume. Since the naturally fractured core has a high fracture permeability, water fills first the fracture space, and then a sharp increase in pressure indicates that the matrix porous space is being filled. Applying Equation 2.4 the fracture porosity can be estimated.

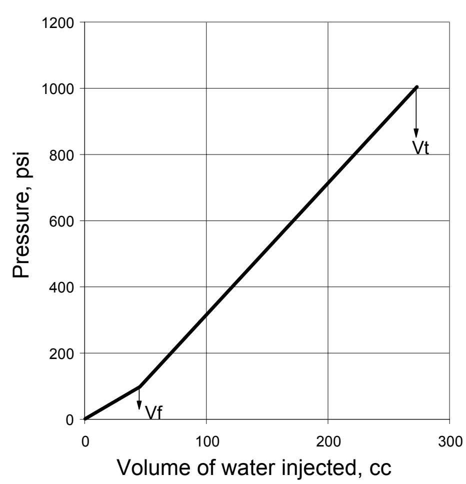

Figure 2.2. Locke and Bliss method for estimating the fracture pore space. (Tiab and Donaldson[1])

2.4 EFFECT OF STRESS ON FRACTURE POROSITY

In naturally fractured reservoirs, changes in effective stress affect primarily the fracture network space, then a reduction in pore pressure due to production, will produce fracture closure.

2.4.1 Effective Stress Concept

Since the pore pressure, p_p, and confining pressure, p_c, have opposite effects on the volumes, it would be convenient to subtract some fraction of the pore pressure from the confining pressure. Terzaghi[17] in 1936 introduced the concept of "effective stress", p_e, presented here in Equation 2.6. This equation allows us to express all the rock properties of a porous rock (fractured or not) as a function of the effective stress.

$$p_e = p_c - \alpha p_p \qquad (2.6)$$

Where α is the "Biot[18] effective stress coefficient", which is defined by:

$$\alpha = 1 - \frac{K_{dry}}{K_g} \qquad (2.7)$$

K_{dry} is the bulk modulus of the dry frame of the rock (pores + grains) and K_g is the bulk modulus of the grains. Usually, α is assumed to be the unity, which is valid only in high porous or weaker rocks (ϕ>5% and/or bad cemented rocks), where the bulk modulus of the grains is much higher than the bulk modulus of the dry frame, which makes negligible the second term on the right side of Equation 2.7. Under these assumptions, Equation 2.6 reduces to:

$$p_e = p_c - p_p \tag{2.8}$$

From density logs, the confining pressure resulting from the overburden can be computed by integration as:

$$p_e = g\int_0^{TVD} \rho dD \tag{2.9}$$

Where:

$g =$ acceleration due to gravity.

$\rho =$ density of the saturated rock as function of depth.

$D =$ depth.

$TVD =$ true vertical depth.

If there are not available density logs, a common practice is to assume a constant saturated rock density of 2.3 gm/cm^3, which corresponds to a lithostatic gradient of 1 psi/ft.

2.4.2 Effect of Effective Stress on Fracture Porosity

As shown in Figure 2.3, in a naturally fractured reservoir which has changing stress conditions, the characteristic matrix block side length is larger than the fracture width ($a >>> b_i$), and $b < b_i$, the matrix block sides can be considered of constant shape and length ($a \sim a_i$ = constant).

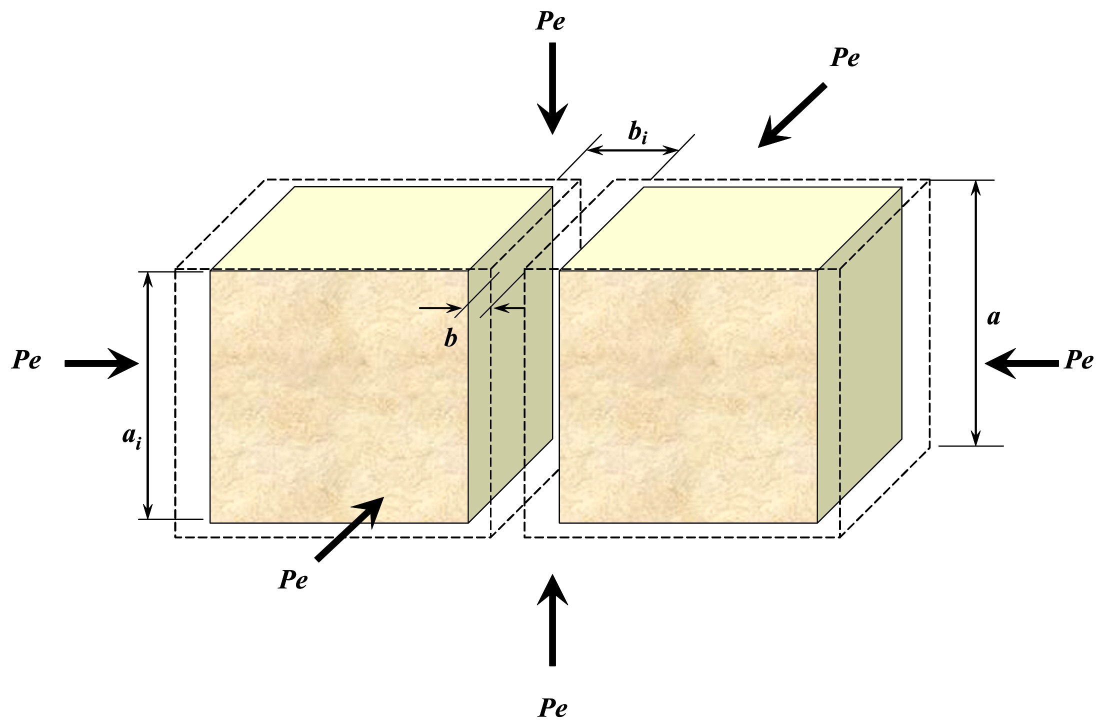

Figure 2.3. Effect of stress on fracture porosity.

Starting from the definition of fracture pore compressibility in terms of fracture porosity:

$$(c_t)_f = \frac{1}{\phi_f}\left(\frac{d\phi_f}{dP_p}\right)_{P_c} \tag{2.10}$$

Where:

$(c_t)_f$ total compressibility of the fracture due to a variation of the pore pressure at constant confining pressure, psi^{-1}.

$P_p =$ pore pressure, psi.

$\phi_f =$ fracture porosity, fracture volume / total volume.

$b =$ current fracture width (after reservoir depletion), in.

$b_i =$ initial fracture width (before reservoir depletion), in.

$a =$ characteristic block side length, in.

As a is constant, for any NFR model, the fracture porosity equation can be generalized as:

$$\phi_f = \xi * b \tag{2.11}$$

Where ξ is a geometric constant depending upon each model (Table 2.1).

Differentiating with respect to b:

$$d\phi_f = \xi * db \tag{2.12}$$

Substituting into Equation 2.10:

$$(c_t)_f = -\frac{1}{\xi * b}\frac{\xi * db}{dP_p} = -\frac{1}{b}\frac{db}{dP_p} \tag{2.13}$$

Separating and integrating:

$$\int_{Pp_i}^{Pp} (c_t)_f dP_p = \int_{b_i}^{b} \frac{db}{b}$$

$$(c_t)_f (P_p - P_{p_i})_e = \ln \frac{b}{b_i}$$

Solving for the current fracture width:

$$b = b_i e^{-(c_t)_f (P_{p_i} - P_p)} \tag{2.14}$$

Substituting the definition of fracture porosity (Equation 2.11) yields:

$$\phi_f = \phi_{f_i} e^{-(c_t)_f (P_{p_i} - P_p)} = \phi_{f_i} e^{-(c_t)_f (P_i - \overline{P})} \tag{2.15}$$

Where:

P_i = P_{pi} = initial pore pressure = initial reservoir pressure.

$\overline{P}$ = P_p = current pore pressure = current average reservoir pressure.

Equation 2.15 provides a method to compute the reduction in fracture porosity due to changes in pore pressure.

2.4.3 Effect of Pore Pressure Changes on Matrix Porosity

The definition of compressibility for changes in pore volume due to changes in pore pressure at constant confining pressure states:

$$(c_t)_m = \frac{1}{\phi_m}\left(\frac{d\phi_m}{dP_p}\right)_{P_c} \tag{2.16}$$

Where:

ϕ_m = matrix porosity, matrix pore volume / total volume.

$(c_t)_m$ = total compressibility of the matrix pore due to a variation of the pore pressure at constant confining pressure, psi^{-1}.

Solving the partial differential Equation 2.16 yields:

$$\Delta\phi_m = 1 - \phi_{m_i} e^{-(c_t)_m (Pi - \overline{P})} \tag{2.17}$$

Sondergeld and Rai[19] presented a similar equation to compute the reduction in porosity for isotropic rocks, $\Delta\phi$, due to increases in the effective stress of the rock.

$$\Delta\phi_m \approx \frac{\Delta p_e}{K_m} = \Delta p_e (c_{bc,m}) \tag{2.18}$$

Where K_m is the bulk modulus of the matrix frame.

The subscript *m* indicates matrix isotropic rock. Sondergeld and Rai[19] demonstrated that a rock with bulk modulus of 2 Mpsi ($c_{bc,m}$=5x10^{-6} psi^{-1}), and a change in the effective stress of 5000 psi has a reduction of porosity of only 0.25% (equations 2.17 and 2.18 give similar results). Therefore, this concludes that there are not significant changes in matrix porosity with changes in the effective stress of a fractured rock.

3 FRACTURE PERMEABILITY

Permeability is a tensor which depends upon the flow direction. In the case of fractured networks, permeability shall be assumed to be parallel to the fracture planes as shown in Figure 3.1 (Reiss[8]).

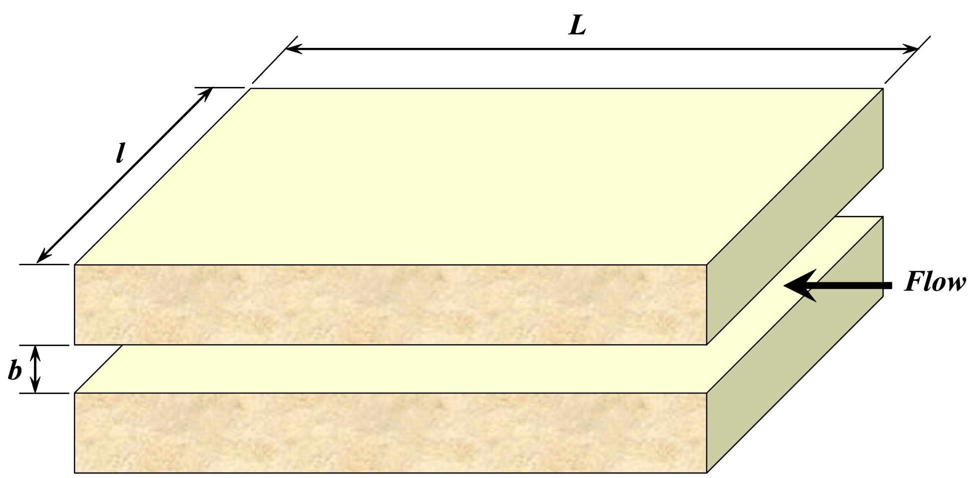

Figure 3.1. Fracture permeability definition.

Darcy's law across a fracture path can be written as:

$$q = \frac{Ak_f}{\mu} \frac{\Delta P}{L} \tag{3.1}$$

For laminar flow along two parallel planes, Poiseuille's Equation becomes:

$$q_1 = \frac{b^3 l}{12\mu} \frac{\Delta P}{L} \tag{3.2}$$

For a system composed by n fractures it becomes:

$$q_n = n \frac{b^3 l}{12\mu} \frac{\Delta P}{L} \tag{3.3}$$

Equating 3.2 and 3.3, for $q = q_n$, and solving for fracture permeability becomes:

$$k_f = \frac{n}{A} \frac{b^3 l}{12} = f_s \frac{b^3}{12} \tag{3.4}$$

Where:

A = net cross section area opens to flow.

B = fracture width.

$f_s = nl/A$ = total fracture length per cross section area (see Table 3.1).

k_f = fracture permeability.

L = section length.

l = section width.

ΔP = pressure drop along the fracture.

q = flow rate.

The geometry models considered in this study are listed in Table 3.1:

Table 3.1. Total fracture length per unit cross section for NFR models.

Model	f_s
Cubes	*2/a*
Match-sticks with flow perpendicular to the axes of the matches	*1/a*
Match-sticks with flow parallel to the axes of the matches	*2/a*
Sheets	*1/a*

Appendix B presents a summary table of the relationships among fracture parameters in terms of fracture geometry and plots relating the variables fracture porosity, fracture permeability, fracture width and characteristic matrix block length.

3.1 EFFECT OF STRESS ON PERMEABILITY

As the naturally fractured reservoir produces, pore pressure decreases, fracture width decreases, and fracture permeability decreases. Equation 3.5 calculates the permeability after depletion in terms of initial fracture width and is found by substituting Equation 2.14 into 3.4:

$$k_f = f_s \frac{b_i^3}{12} e^{-3(c_t)_f (Pi - \overline{P})} \tag{3.5}$$

Taking the ratio between equations 3.5 and 3.4 at initial reservoir conditions yields:

$$k_f = k_{f_i} e^{-3(c_t)_f (Pi - \overline{P})} \tag{3.6}$$

Where:

k_{fi} = fracture permeability at the initial reservoir pressure, P_i.

k_f = fracture permeability at the current average reservoir pressure, $\overline{P}$.

A similar expression was presented by Saidi[20]:

$$c_{ef} = \frac{1 - \left(k_f / k_{fi}\right)^{1/3}}{\Delta p} \tag{3.7}$$

Applying Terzaghi's Law of effective stress, Equation 2.8, and assuming no changes in the confining pressure (overburden does not change), Saidi's equation becomes:

$$k_f = k_{fi}\left(1 + c_{ef}\Delta p\right)^3 \tag{3.8}$$

The effective permeability can be obtained from (Tiab and Donaldson[1]):

$$k = \sqrt{k_{\max} k_{\min}} \tag{3.9}$$

Where:

k_{max} = maximum permeability measured in the direction parallel to the fracture plane (Figure 3.2), thus, $k_{max} \approx k_f$.

k_{min} = minimum permeability measured in the direction perpendicular to the fracture plane (Figure 3.2), thus $k_{min} \approx k_m$.

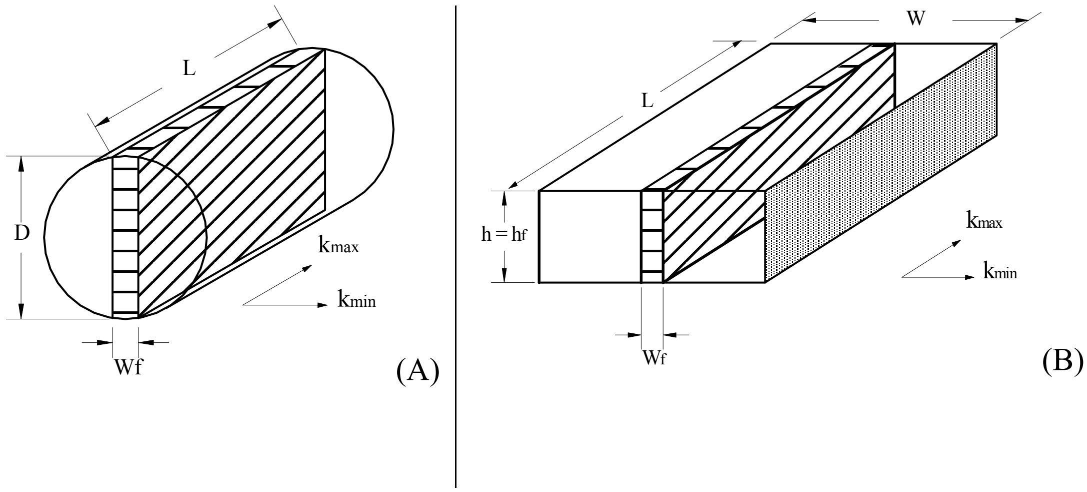

Figure 3.2. Maximum and minimum permeability.
(Tiab and Donaldson[1])

Substituting, Equation 3.9 yields:

$$k_f = \frac{k^2}{k_m} \tag{3.10}$$

Substituting Equation 3.10 into Equation 3.6, a new expression to compute the change in the average effective permeability as a function of fracture compressibility and change in effective stress is found.

$$k = k_i e^{-\frac{3}{2}(c_t)_f (Pi-\overline{P})} \tag{3.11}$$

4 WELL TEST ANALYSIS IN NATURALLY FRACTURED RESERVOIRS

As shown in Chapter Two, naturally fractured reservoirs are characterized by the presence of two distinct types of porous media, matrix and fracture porosity, which is the reason why they often are called dual porosity reservoirs (see Figure 1.1). The general assumptions in well test analysis are: a) pseudosteady state matrix flow, b) production from the matrix goes to the fracture and then into the wellbore, the matrix does not provide fluids directly to the wellbore and, c) the matrix has low permeability but large storage capacity relative to the fracture system, while the fractures have high permeability but low storage capacity.

Warren and Root[6] introduced two dimensionless dual porosity parameters in addition to the single porosity parameters to characterize naturally fractured reservoirs, the interporosity flow coefficient, λ, and the storage capacity ratio, ω.

Interporosity flow coefficient, λ, is the fluid exchange between the matrix and the fractures and is defined by:

$$\lambda = \alpha \frac{k_m r_w^2}{k_f} \tag{4.1}$$

Where k_m = permeability of the matrix, k_f = permeability of the natural fractures and α = parameter characteristic of the system geometry given by:

$$\alpha = \frac{4n}{(n+2)x_m^m} \tag{4.2}$$

Where n is 1, 2, and 3 for sheet, matches, and cube models; x_m represents the side length of the cube or the diameter of the sphere block.

For the sugar cube model, the side length of each matrix block is obtained from:

$$x_m = r_w \sqrt{\frac{60k_m}{\lambda k_f}} \tag{4.3}$$

A value of unity for λ indicates the absence of fractures. Low values of λ indicate low fluid transfer between the matrix and the fractures. λ ranges between 10^{-3} to 10^{-9} indicate high to poor fluid transfer between the matrix and the fractures.

The storage capacity ratio, ω, is a measure of the relative fracture storage capacity of the reservoir and is defined by:

$$\omega = \frac{(\phi c_t)_f}{(\phi c_t)_{f+m}} = \frac{(\phi c_t)_f}{(\phi c_t)_f + (\phi c_t)_m} = \frac{(\phi c_t)_f}{(\phi c_t)_t} \tag{4.4}$$

Where ϕ = ratio of the system pore volume (PV) to the total volume. The subscripts f and $f+m$ refer to the fracture and the total system (fracture plus matrix).

4.1 CONVENTIONAL METHODS

Traditionally, conventional methods for well test analysis in NFRs have been performed using semilog analysis and type curve matching.

4.1.1 Traditional Semilog Analysis Technique

Warren and Root[6] presented this technique, when they predicted that in dual porosity systems two parallel lines will develop on a semilog plot of pressure vs. time as shown in Figure 4.1.

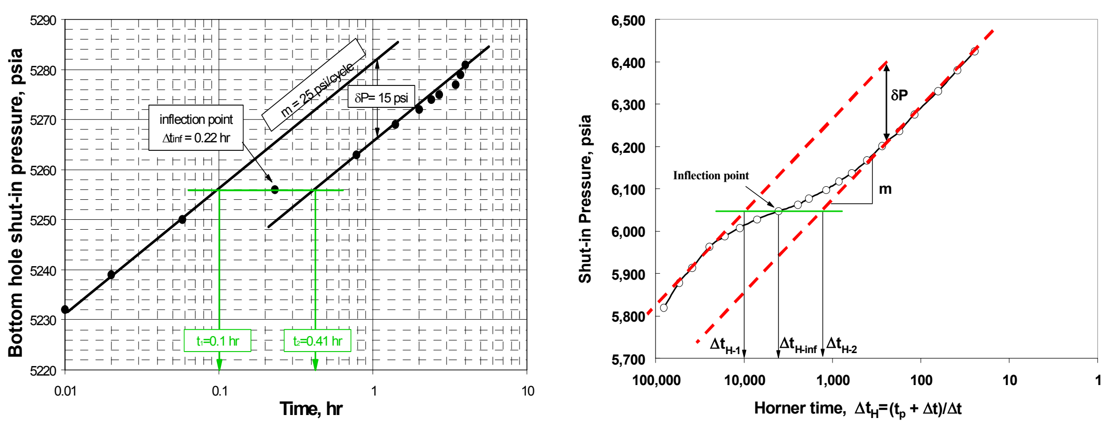

a) Drawdown test. *b) Buildup test.*

Figure 4.1. Typical pressure curves for a semilog analysis in naturally fractured reservoirs.
(Tiab and Donaldson[1])

If the initial and final straight lines can be identified and the pressure difference, δP, established, the storage capacity ratio can be computed from:

$$\omega = \exp\left(-2.303\frac{\partial P}{m}\right) \tag{4.5}$$

Or:

$$\omega = 10^{-\frac{\partial P}{m}} \tag{4.6}$$

Denotating t_1 and t_2 which are the times of intersection of a horizontal line drawn through the inflection point with the first and second line, then the storage capacity ratio for a drawdown test also can be expressed as:

$$\omega = \frac{t_1}{t_2} \tag{4.7}$$

For a buildup test use the Horner[21] time *$(t_p+\Delta t)\Delta t$* instead of t, and it becomes:

$$\omega = \frac{\left[(t_p + \Delta t)/\Delta t\right]_1}{\left[(t_p + \Delta t)/\Delta t\right]_2} \tag{4.8}$$

For a drawdown test, the interporosity flow coefficient, λ, is computed as (Bourdet *et al.*[22]):

$$\lambda = \frac{(\phi c_t)_f \mu r_w^2}{1.781 k t_1} = \frac{(\phi c_t)_{f+m} \mu r_w^2}{1.781 k t_2} \tag{4.9}$$

For a buildup test by:

$$\lambda = \frac{(\phi c_t)_f \mu r_w^2}{1.781 k t_p}\left(\frac{t_p + \Delta t_1}{\Delta t_1}\right) = \frac{(\phi c_t)_{f+m} \mu r_w^2}{1.781 k t_p}\left(\frac{t_p + \Delta t_2}{\Delta t_2}\right) \tag{4.10}$$

The slope is used to estimate the formation permeability, *k*, from:

$$k = \frac{162.6 q \mu B_o}{mh} \tag{4.11}$$

The second semilog straight line must be extrapolated to p_{1hr}, and the skin factor is:

$$s = 1.151\left[\frac{\Delta p_{1hr}}{m} - \log\left(\frac{\bar{k}}{\phi \mu c_t r_w^2}\right) + 3.23\right] \tag{4.12}$$

4.1.1.1 Semilog Analysis Technique Based on the Inflection Point

In 2006 Tiab[23] improved the semilog analysis technique for uniformly distributed matrix blocks, where the inflection point is at an equal distance between the two parallel lines, and presented the following new equations to compute the storage capacity ratio and interporosity flow parameter from the inflection point coordinates on the Horner plot (Figure 4.1.b).

$$t_{\inf} = \frac{t_p}{(H_T)_{\inf} - 1} \tag{4.13}$$

$$\omega = 10^{-\frac{2\Delta P_{1\inf}}{m}} \tag{4.14}$$

Where:

(H_T) is the Horner[21] time $(t_p+\Delta t)/\Delta t$ or the effective Horner time $t_p\Delta t/(t_p+\Delta t)$.

ΔP_{1inf} (= $0.5\delta P$) is the pressure drop between the first semilog straight line and the inflection point along a vertical line parallel to the pressure axis.

$$\lambda = \frac{3792(\phi c_t)_{f+m}\mu r_w^2}{kt_{\inf}}\left[\omega \ln\left(\frac{1}{\omega}\right)\right] \tag{4.15}$$

For a short buildup test:

$$\omega = \frac{10^{(P_i - P_{FF1})/m}}{1 - 10^{(P_i - P_{FF1})/m}} \tag{4.16}$$

Where P_{FF1} corresponds to the pressure read at the extrapolation of the straight line to a Horner time of unity, i.e. $(t_p+\Delta t)/\Delta t = 1$.

For a long build up test, when the first straight line is not observed on the semilog plot,

$$\omega = 10^{-\frac{2\Delta P_{2\inf}}{m}} \tag{4.17}$$

Where:

ΔP_{1inf} (= $0.5\delta P$) is the pressure drop between the second semilog straight line and the inflection point along a vertical line parallel to the pressure axis.

4.1.2 Type Curve Analysis Technique

This technique uses type curves designed specially for naturally fractured reservoirs. See Figure 4.2 and Figure 4.3 for an illustration of this technique.

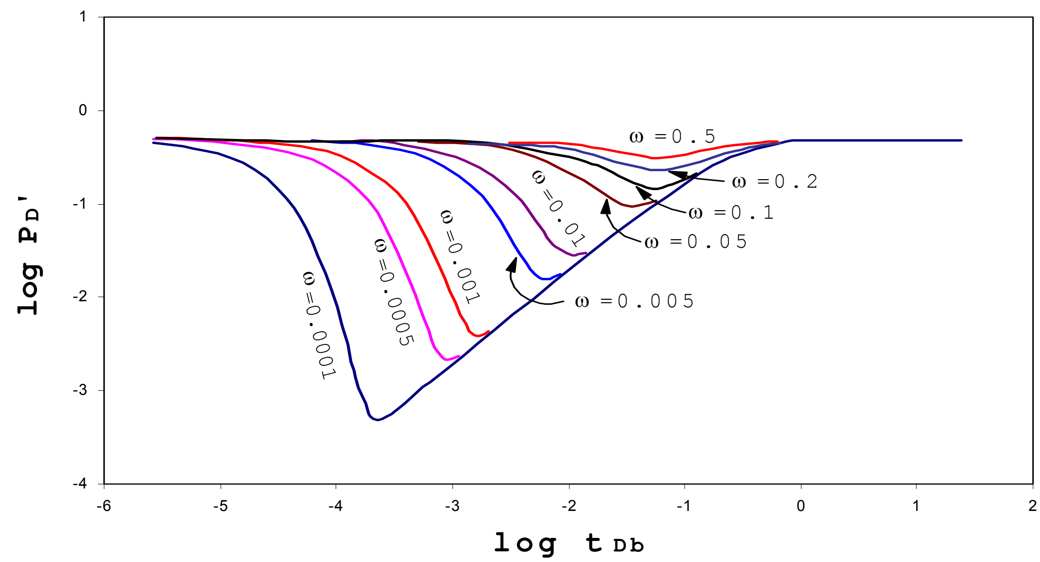

Figure 4.2. Unified derivative type curve.
(Stewart el al.[24])

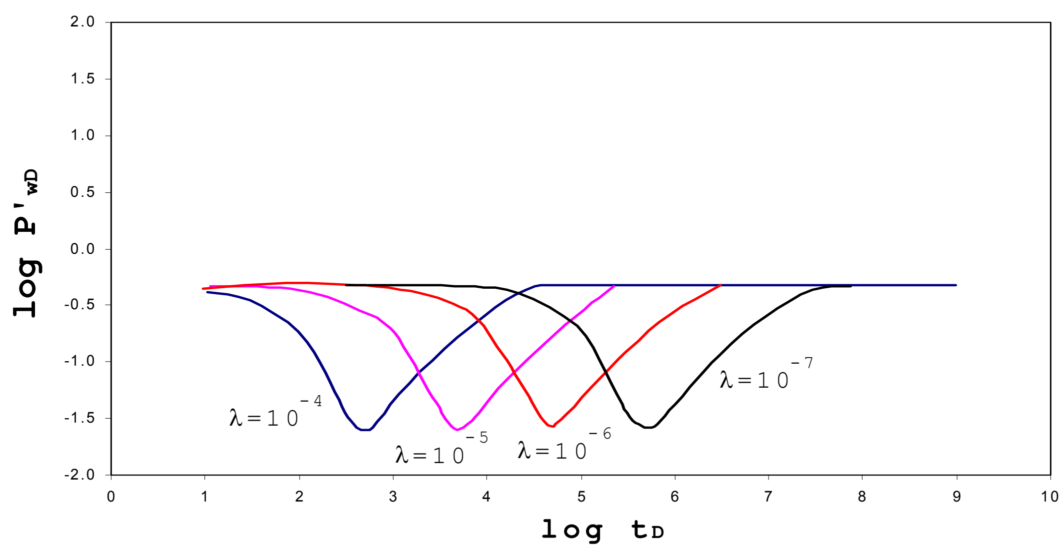

Figure 4.3. Effect of λ on the pressure behavior of dual porosity reservoirs, pseudosteady state model for ω=0.01.
(Stewart el al.[24])

The type curve analysis technique is a trial and error method that requires an estimate of the permeability from a semilog analysis to verify its exactness. Lee *et al.*[25] described the procedure in detail and presented examples of this technique. To summarize:

1. Plot the pressure change and the pressure derivative on log-log tracing paper.

2. From the semilog analysis determine the permeability and calculate the pressure match point with Equation 4.18.

$$(\Delta p)_{MP} = \frac{141.2 qB\mu}{\bar{k}h}(p_D)_{MP} \tag{4.18}$$

Where, the subscript *MP* stands for an arbitrary selected match point.

3. With the type curve in the match position, read the values of $(C_De^{2s})_f$, $(C_De^{2s})_{f+m}$ and λe^{2s}.

4. Determine the storage capacity ratio, dimensionless wellbore storage, skin factor and interporosity flow parameter from:

$$\omega = \frac{(C_De^{2s})_{f+m}}{(C_De^{2s})_f} \tag{4.19}$$

$$C_D = \frac{0.0002637\bar{k}}{\phi\mu c_t r_w^2}\left(\frac{\Delta t}{t_D / C_D}\right)_{MP} \tag{4.20}$$

$$s = 0.5\ln\left[\frac{(C_De^{2s})_{f+m}}{C_D}\right] \tag{4.21}$$

$$\lambda = \frac{(\lambda e^{2s})_{MP}}{e^{2s}} \tag{4.22}$$

4.1.3 *Tiab's Direct Synthesis Technique* (TDS)

In 1993 Tiab[26] introduced a method to interpret pressure transient analysis without the use of type curves. Later on, Engler and Tiab[27] extended the technique to naturally fractured reservoirs.

The log-log plot of the pressure derivative of a well test in a naturally fractured reservoir presents a characteristic trough, which corresponds to the main fingerprint to identify and characterize naturally fractured reservoirs. Figure 4.4 shows the effect of natural fractures on the pressure derivative on a log-log plot of pressure and the pressure derivative against time.

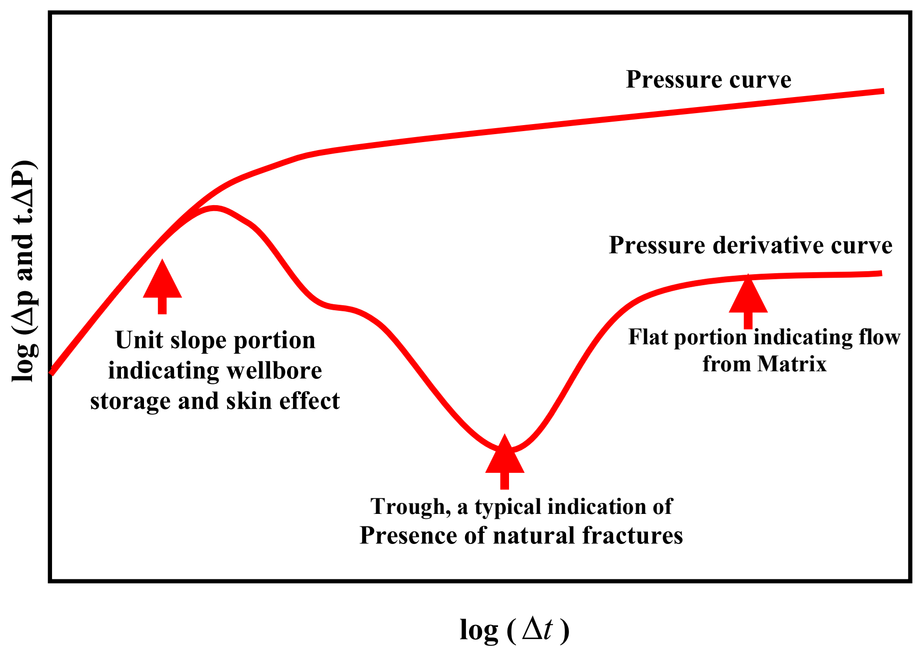

Figure 4.4. Effect of natural fractures on pressure derivative on a log-log plot of pressure and pressure derivative against time.
(Tiab and Donaldson[1])

Figure 4.5 presents the characteristic lines and points required to apply the *Tiab's Direct Synthesis Technique (TDS)*.

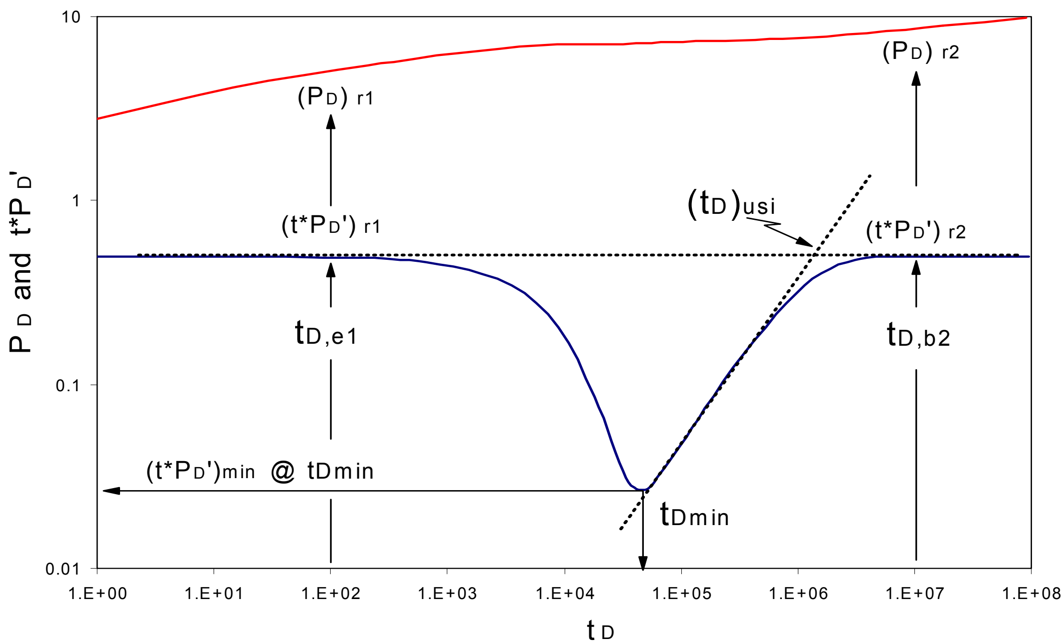

Figure 4.5. Characteristic lines and points of a naturally fractured reservoir with pseudosteady state interporosity flow ω=0.01 and $\lambda=1x10^{-6}$. (Engler and Tiab[27])

In Figure 4.5, Engler and Tiab[27] observed the following characteristics:

1) The early radial flow in the fracture system and the infinite acting radial flow are represented by two horizontal segments in the pressure derivative plot. The first horizontal segment corresponds to fracture depletion and the second segment corresponds to the equivalent homogeneous reservoir response. An expression for the derivative during these times is given by:

$$t_D * p_D' = \frac{1}{2} \tag{4.23}$$

Substituting for the dimensionless variables and rearranging the equation results in a simple and quick technique for determining bulk fracture permeability.

$$k = \frac{70.6 q \mu B_o}{h(t * \Delta p')_r} \tag{4.24}$$

Where $(t^*\Delta P')_r$ is the pressure derivative at some convenient time, t.

2) Notice in Figure 4.5, the characteristic trough on the derivative curve, indicative of the transition period for naturally fractured reservoirs. The depth of this trough is dependent on the dimensionless storage coefficient, but independent of the interporosity flow parameter, see figures 4.2 and 4.3.

3) From the coordinates of the minimum point on the trough of the pressure derivative curve and the radial flow regime (horizontal) line, the storage capacity ratio is obtained as[27]:

$$\omega = 0.15866 \left\{ \frac{(t * \Delta P')_{\min}}{(t * \Delta P')_r} \right\} + 0.54653 \left\{ \frac{(t * \Delta P')_{\min}}{(t * \Delta P')_r} \right\}^2 \tag{4.25}$$

4) The interporosity flow parameter can be obtained from:

$$\lambda = \frac{42.5 h (\phi c_t)_{f+m} r_w^2}{q B_o} \left(\frac{t * \Delta P'}{t} \right)_{\min} \tag{4.26}$$

5) The wellbore storage coefficient can be obtained as follows:

From the log-log plot of *ΔP* vs. *t*, read the coordinates of one point on the early unit slope line, and if it is present, compute the wellbore storage using the following equation:

$$C = \left(\frac{qB}{24}\right)\frac{t}{\Delta P} \tag{4.27}$$

6) The skin factor is computed from:

$$s = \frac{1}{2}\left[\frac{\Delta P_r}{(t*\Delta P')_r} - \ln\left(\frac{k\,t_r}{\mu(\phi c_t)_{f+m} r_w^2}\right) + 7.43\right] \tag{4.28}$$

5 WELL TEST ANALYSIS AND ELASTIC BEHAVIOR OF NATURALLY FRACTURED RESERVOIRS

In order to analyze the effect of stress on the fracture parameters, it is essential to analyze the relationship between the elastic properties of the rock frame (matrix plus fractures) and well test analysis. The main assumption is that the anisotropic double porosity rock is composed of elastically isotropic blocks (matrix) separated by fractures as shown in Figure 5.1.

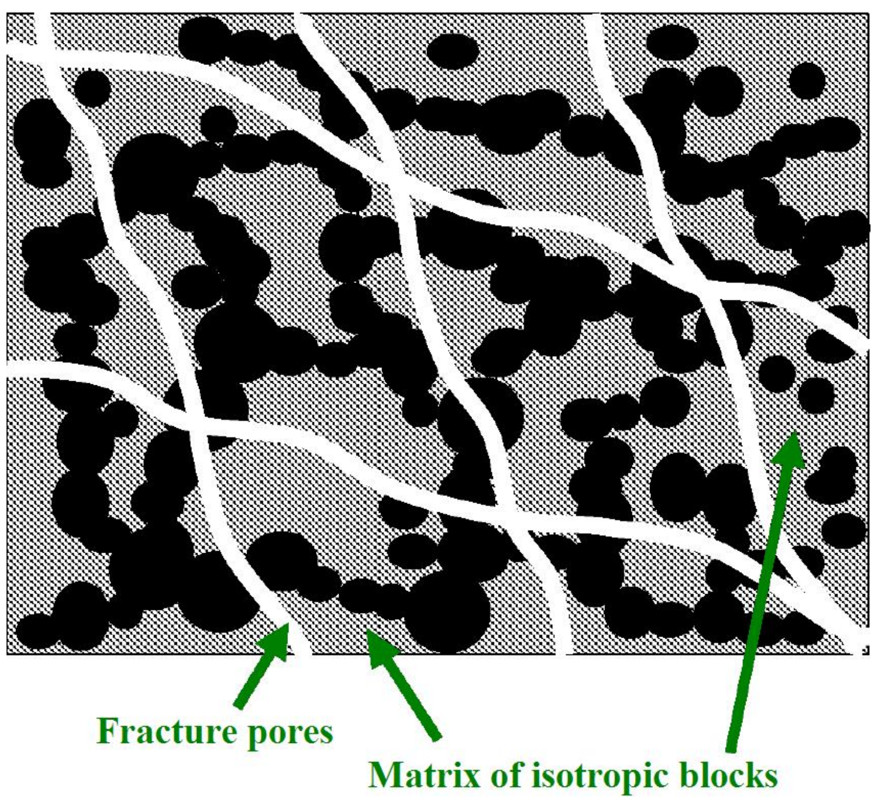

Figure 5.1. Schematic representation of the anisotropic, double porosity rock. (Cardona et al.[28])

Using Equations 4.6 or 4.25, from pressure well test analysis, it is possible to estimate the storage capacity ratio. Then Cardona *et al.*[28] demonstrated that using Zimmerman's[29] rock compressibility relations and Schoenberg's linear slip theory (Schoenber and Douma[30], Schoenberg and Sayers[31]), the storage capacity ratio can be related to the normal compliance of the fracture system. Since in fractured rocks the bulk modulus is a function of the normal fracture compliance, relationships between the storage capacity and the normal fracture compliance can be derived. For the case of two orthogonal fracture sets and a single fracture set, Bakulin *et al.*[32] presented a technique to estimate the normal fracture compliance from multi-component seismic data. Later on, in 2005 Brown[33] presented a discussion in which treats the normal fracture compliance as a function of stress and pore pressure.

As result of Bakulin *et al.*[32] and Cardona *et al.*[28] works, seismic derived normal fracture compliance allows us to estimate the storage capacity ratio without well data. Where well data are available, another independent estimate of storage capacity ratio can be obtained, which leads us to link seismic to pressure transient analysis.

5.1 EFFECT OF STRESS ON STORAGE CAPACITY RATIO, ω

The storage capacity of any porous media can be expressed as:

$$(\phi c_t) = \phi\left(c_F + c_{pp}\right) = \phi\left(\frac{1}{K_F} + c_{pp}\right) \tag{5.1}$$

$$c_F = \frac{1}{K_F} = c_o S_o + c_g S_g + c_w S_w \tag{5.2}$$

Where:

c_{pp} = compressibility of the pore due to a variation of the pore pressure at a constant confining pressure, psi.

ϕ = porosity, fraction.

K_F = fluid bulk modulus, psi, or MPa

c_o, c_w, and c_g = oil, water, and gas compressibilities respectively, fractions.

S_o, S_w, and S_g = oil, water, and gas saturations respectively, fractions.

Figure 5.2 presents the behavior for Bandera sandstone of the pore compressibility with respect to the confining stress and effective stress at different pore pressures. From the figure, one can see that the pore compressibility c_{pc}, reduces when the effective stress increases.

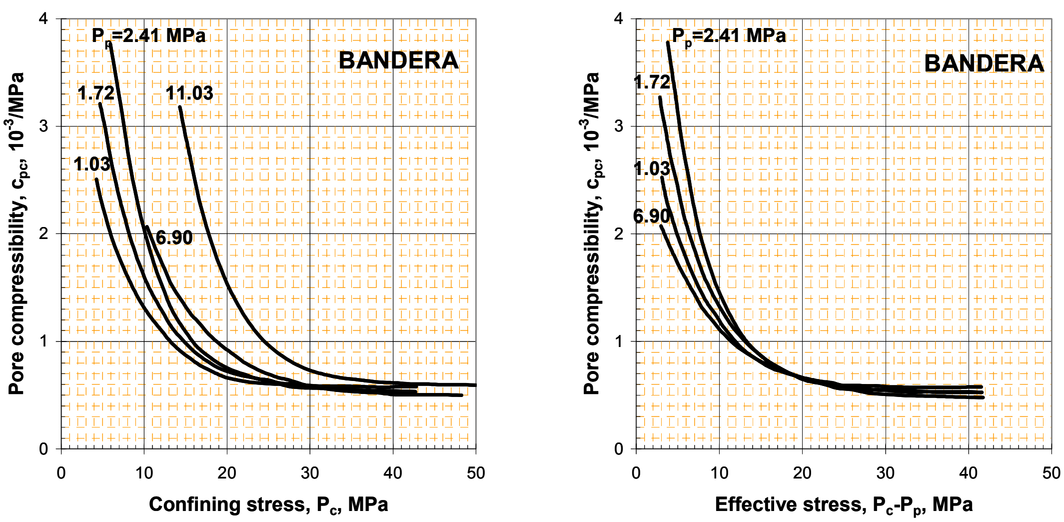

Figure 5.2. Pore compressibility of Bandera sandstone as function of confining pressure and effective stress.
(Zimmerman et al.[29])

The diffusivity equation describes the pressure variation (Δp) with time (t). In order to model dual porosity media with two different types of storage and flow capacities, two differential equations are required.

The first required differential equation, which models the flow through the fracture network into the wellbore in radial coordinates, is described by:

$$\frac{k_f}{\mu}\frac{1}{r}\frac{\partial}{\partial r}\left(r\frac{\partial \Delta p_f}{\partial r}\right) = (\phi c_t)_f\frac{\partial \Delta p_f}{\partial t} + (\phi c_t)_m\frac{\partial \Delta p_m}{\partial t} \tag{5.3}$$

Where k_f is the fracture permeability, μ is the fluid viscosity and ϕc_t is the storage capacity with the subscript f indicating fracture pores and the subscript m indicating matrix isotropic media. Δp_f and Δp_m indicate the pressure variations in the fracture pore space and the matrix pore space respectively.

In the second required differential equation, the volume of fluid flowing from the isotropic matrix into the fractures is described by the second term on the right side of Equation 5.3. However, the pressure differential between matrix and fracture pores (Δp_f - Δp_m), and the permeability of the matrix (k_m) determine the flow rate into the fracture system. Therefore,

$$(\phi c_t)_m\frac{\partial \Delta p_m}{\partial t} = \frac{k_m}{\mu}\frac{(\Delta p_f - \Delta p_m)}{x_m^2} \tag{5.4}$$

Where, x_m is the side length of each matrix block, as previously defined by Equation 4.3.

Solutions to the partial differential equations 5.3 and 5.4 lead to the definition of storage capacity ratio, ω, presented in Equation 4.4, which also can be rewritten as:

$$\omega = \frac{\left(\dfrac{\phi_f}{\phi_T}\right)\left(\dfrac{(c_t)_f}{(c_t)_m}\right)}{\left(\dfrac{\phi_f}{\phi_T}\right)\left(\dfrac{(c_t)_f}{(c_t)_m}-1\right)+1} \tag{5.5}$$

Figure 5.3 represents a graphical plot of Equation 5.5, in which the influence of the compressibility ratio, $c_{t,f}/c_{t,(f+m)}$, and the porosity partitioning coefficient, ϕ_f/ϕ_T, on the storage capacity ratio, ω, can be appreciated.

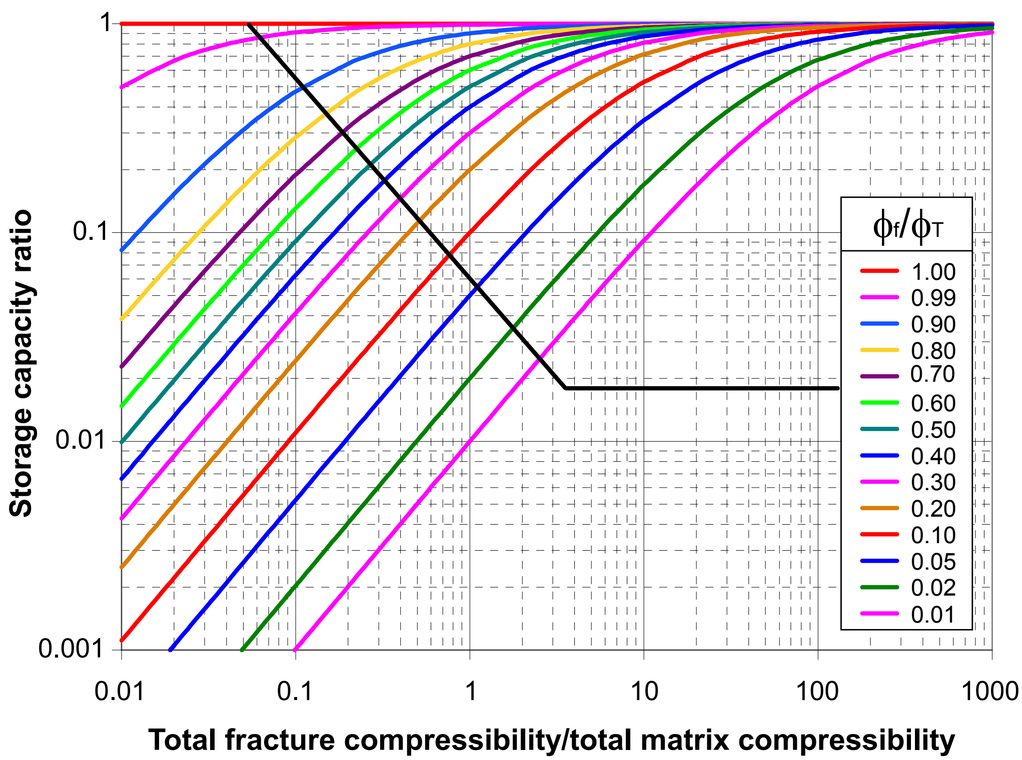

Figure 5.3. Effect of compressibilities on the storage capacity ratio.

5.1.1 Storage Capacity Ratio and Normal Fracture Compliance

The presence of fractures increases the overall compressibility of the isotropic porous rock, because of the excess compliance associated with the fracture system (Schoenberg and Sayers[31]). The compressibility of the dry fractured rock can be expressed as:

$$c_{pp,(f+m)} = \frac{1}{K_{d,(f+m)}} = Z_{Nf} + \frac{1}{K_{d,m}} \tag{5.6}$$

Where Z_{Nf} is the normal compliance of the fracture system, $K_{d,m}$ is the bulk modulus of the isotropic matrix of the rock, and the subscript *(f+m)* takes into account the whole fractured rock.

Sheriff[34] defined: "*Compliance is an elastic property defined as the relationship of strain to stress. Compliance is a tensor of rank 4, but it is also expressible as a 6 x 6 matrix that is the inverse of the stiffness matrix. Compliance is the mechanical or acoustical equivalent of electrical capacitance*."

Using the equations presented by Zimmerman's[29] that relate the pore space compressibility to the bulk compressibility of the rock (see appendix D), Cardona *et al.*[28] demonstrated that the total and fracture storage capacities can be expressed as:

$$(\phi c_t)_f = \left(\frac{1}{K_F} - \frac{1}{K_g}\right)\phi_f + \left(\frac{1}{K_{d,(f+m)}} - \frac{1}{K_{d,m}}\right) \tag{5.7}$$

$$(\phi c_t)_f + (\phi c_t)_m = \left(\frac{1}{K_F} - \frac{1}{K_g}\right)\phi_T + \left(\frac{1}{K_{d,(f+m)}} - \frac{1}{K_g}\right) \tag{5.8}$$

K_g is the bulk modulus of the grains (isotropic mineral material) and ϕ_T is the total porosity of the rock.

By substituting equations 5.7 and 5.8 into Equation 4.4 Cardona *et al.*[28] found another expression for the storage capacity ratio.

$$\omega = \frac{\left(\frac{1}{K_F} - \frac{1}{K_g}\right)\phi_f + \left(\frac{1}{K_{d,(f+m)}} - \frac{1}{K_{d,m}}\right)}{\left(\frac{1}{K_F} - \frac{1}{K_g}\right)\phi_T + \left(\frac{1}{K_{d,(f+m)}} - \frac{1}{K_g}\right)} \tag{5.9}$$

Inserting Equation 5.6 into 5.9, an expression for ω as a function of the normal compliance of the fracture system, Z_{Nf}, is obtained:

$$\omega = \frac{\left(1 - \frac{K_F}{K_g}\right)\phi_f + K_F Z_{Nf}}{\left(1 - \frac{K_F}{K_g}\right)\phi_T + K_F Z_{Nf} + K_F c_{pc,m}\phi_m} \tag{5.10}$$

$c_{pc,m}$ is the compaction compressibility of the isotropic matrix pore.

From inspection of equations 4.4 and 5.10, the storage capacity ratio, ω, provides the link between pressure transient analysis and the normal fracture compliance estimated from seismic data (Cardona *et al.*[28]).

In order to simplify Equation 5.10, Cardona *et al.*[28] proposed the following approximations:

1) Limiting the case for very compressible fluids ($K_F \rightarrow 0$GPa). When the fluid stored inside the rock is a gas at low effective stress, the bulk modulus of the fluid is negligible ($K_F \approx 0$), which simplifies Equation 5.10 to:

$$\omega \approx \frac{\phi_f}{\phi_T} = \frac{\phi_f}{\phi_f + \phi_m} \tag{5.11}$$

2) Limiting the case for very incompressible fluids ($K_F \rightarrow 3$GPa), a good approximation to ω is:

$$\omega = \frac{K_F Z_{Nf}}{\phi_T + K_F Z_{Nf}} \tag{5.12}$$

Equation 5.12 allows us to estimate the storage capacity ratio from core analysis or seismic derived values of normal compliance of the fracture Z_{Nf}. When K_F and ϕ_T are known, equations 5.11 and 5.12 can be used to compute fracture porosity, ϕ_f, or normal compliance of the fracture, Z_{Nf}.

The bulk modulus in terms of s- and p-wave velocities is defined by:

$$K = \rho\left(V_p^2 - \frac{4}{3}V_s^2\right) \tag{5.13}$$

V_p and V_s are the compressional and shear wave velocities respectively.

Appendix A presents a table with the equivalents of the different elastic constants, expressed in terms of each other and p-wave and shear wave velocities (V_p, V_s).

5.1.2 Fracture Density Computed from the Normal Compliance of the Fracture

In 2000 Bakulin *et al.*[32] proposed a method to compute the normal compliance of the fracture from seismic derived information assuming a specific micro structural description of the fractures, and that the fracture pores behave elastically as a single set of aligned penny-shaped cracks.

$$Z_{Nf} = \frac{A_N D_f}{M_m (1 - A_N D_f)} \tag{5.14}$$

Where:

$$A_N = \frac{4}{3 \frac{V_{p_m}}{V_{s_m}} \left(1 - \frac{V_{p_m}}{V_{s_m}}\right)} \tag{5.15}$$

$M_m =$ p-wave modulus of the matrix (isotropic background rock).

V_{p_m} and $V_{s_m} =$ p- and s-wave velocities of the isotropic matrix rock respectively.

The fracture density, D_f, is a function of the fracture aspect ratio, α_f, and is defined as:

$$D_f = \frac{3\phi_f}{4\pi\alpha_f} \tag{5.16}$$

Using Equation 5.11 we can estimate the fracture porosity from ω, and applying Equation 5.16 compute the fracture density; but it requires the geometrical assumption that the fractures behave as ellipsoidal cracks.

In order to prove that Equation 5.12 is a good approximation to Equation 4.4, Cardona *et al.*[28] computed ω for different fluid bulk modules, K_F, and $\phi_T = 0.05$, using the exact and approximated equations; figures 5.4, 5.5 and 5.6 present their results. From the figures below, it is observed that the approximations give reliable values.

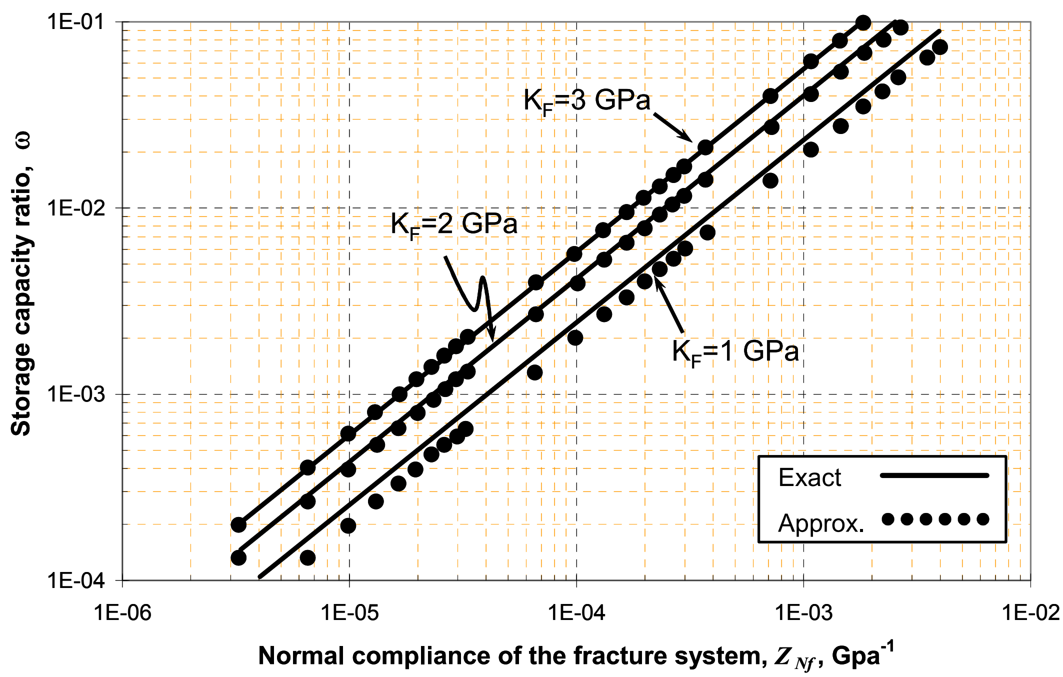

Figure 5.4. Storage capacity ratio vs. normal compliance of the fracture system. (Cardona et al.[28])

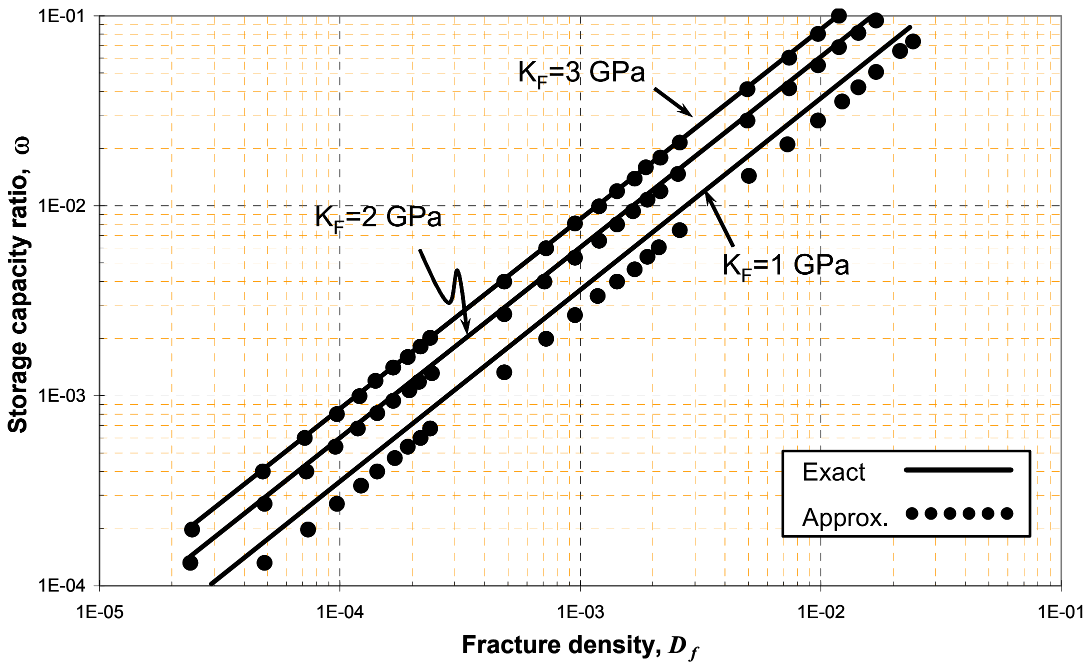

Figure 5.5. Storage capacity ratio vs. fracture density. (Cardona et al.[28])

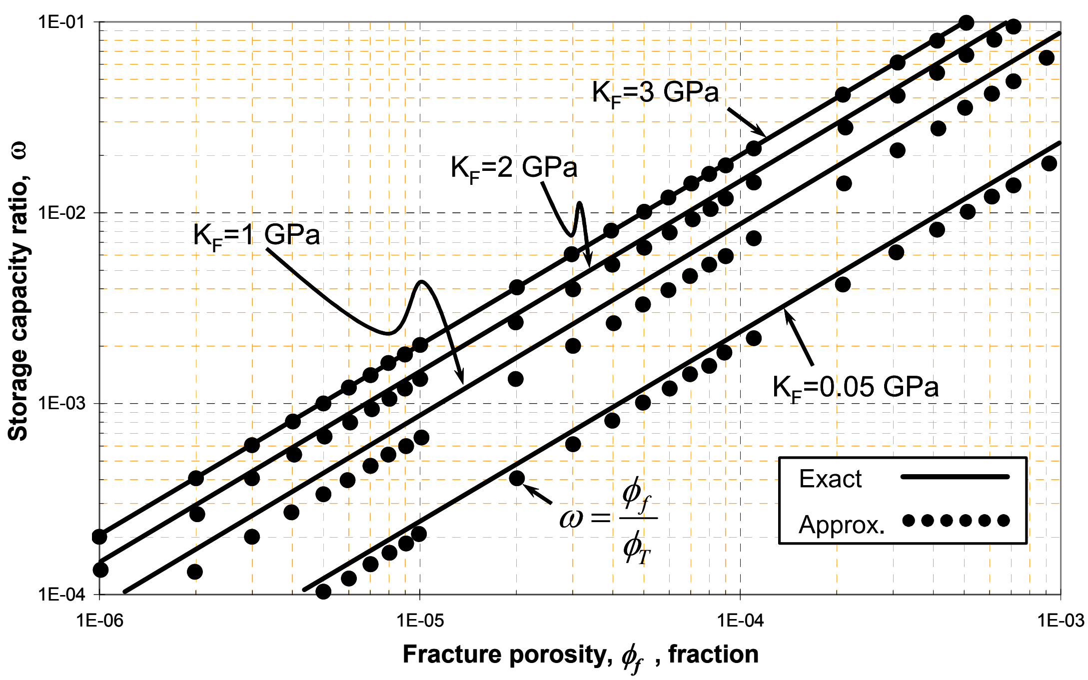

Figure 5.6. Storage capacity ratio vs. fracture porosity. (Cardona et al.[28])

As shown in Figure 5.6, the bulk modulus of the fluid inside the porous rock affects the fracture porosity, since most of the fluids in the reservoir are in the range of 0.05GPa$<K_F<$3Gpa. In addition, fracture porosity can be estimated from seismic derived information using Equation 5.11 for compressible fluids and from Equation 5.12 for slightly compressible fluids.

6 PROPOSED WELL TEST TECHNIQUE

As shown in previous chapters, only having pressure data does not provide enough information about the reservoir. Therefore, it is necessary to have accurate values of reservoir properties to perform the analysis. Thus, in order to predict the effect of stress on rock properties in fractured saturated rocks it requires integration of information from different sources, such as well logging, core analysis, petrophysics and seismic derived information.

The conventional and Tiab's direct synthesis techniques have been extended to compute the fractured rock properties: fracture and matrix porosity, fracture and matrix and total compressibilities, average permeability and the normal compliance of the fractures at in-situ stress conditions.

Since the overburden remains constant, the only way to change the in-situ effective stresses of the reservoir is by producing or injecting fluids, which modifies the pore pressure and changes the effective stress of the rock. Therefore, it is necessary to gather additional reservoir information such as average total permeability, and/or average reservoir pressure at two different stages of the production of the reservoir (data from the same well are preferable). Generally, initial condition and current conditions are taking into account. In this chapter, a step by step procedure and a worked example explain the proposed well test analysis technique.

6.1 STEP BY STEP PROCEDURE

Step One: Compute the Pore Pressure

Perform a pressure build up analysis and determine the current average reservoir pressure. The pore pressure corresponds to the current average reservoir pressure.

Step Two: Compute the Confining Pressure and Effective Stress

The confining pressure is caused by the overburden of the rocks. If density logs are available in the region, compute the confining pressure by integration of the density response with respect to the depth (Equation 2.9). If density logs are not available, a good approximation is to assume a constant density of the rock of 2.3 gm/cm^3, which corresponds to a lithostatic gradient of 1 psi/ft. Compute effective stress using Terzagui's law (Equation 2.6).

$$p_e = g\int_0^{TVD} \rho dD \tag{2.9}$$

$$p_e = p_c - \alpha p_p \tag{2.6}$$

Step Three: Compute the Wellbore Storage Coefficient

On the log-log plot of the pressure derivative versus test time, read the Δt and ΔP coordinates for a point on the early unit-slope straight line and use Equation 4.27 to compute the wellbore storage coefficient.

$$C = \left(\frac{qB}{24}\right)\frac{t}{\Delta P} \tag{4.27}$$

Step Four: Compute the Storage Capacity Ratio

On the log-log plot of the pressure derivative curve, read the coordinates for the minimum point of the trough (t_{min} and $(t^*\Delta p')_{min}$) and the pressure derivative coordinate for the late time radial flow regime($(t^*\Delta p')_{min}$). Use Equation 4.25 to compute the storage capacity ratio.

$$\omega = 0.15866\left\{\frac{(t*\Delta P')_{\min}}{(t*\Delta P')_r}\right\} + 0.54653\left\{\frac{(t*\Delta P')_{\min}}{(t*\Delta P')_r}\right\}^2 \tag{4.25}$$

If the late radial flow regime cannot be identified on the log-log plot of the pressure derivative since it is a short test or the presence of boundary masks the radial flow period, the storage capacity ratio can be estimated using commercial pressure analysis software (i.e. Saphir®, Pie®) only if you do a historical match over the whole production and pressure history for an analytical or numerical reservoir model.

Step Five: Compute the Compressibility of the Reservoir Fluid

From PVT correlations or lab measurements estimate the fluid compressibility. Another method is from the physical properties of the fluids to determine the velocity of the sound across them. For mixtures of different fluids use mixing laws to compute the compressional wave velocity, harmonic average, equivalent to Reuss isostress average is used for modulii of fluids, and compute fluid compressibility as the inverse of the fluid bulk modulus (since fluids do not have shear, equation presented in Appendix A reduces to: $c_F = \frac{1}{K_F} = \frac{1}{\rho\left(V_p^2 - \frac{4}{3}V_s^2\right)} = \frac{1}{\rho V_p^2}$).

Step Six: Compute the Normal Compliance of the Fracture

Compute the normal compliance of the fracture using Equation 5.12.

$$c_{pp,f} = Z_{Nf} = \left(\frac{\omega}{1-\omega}\right)\frac{\phi_T}{K_F} \tag{5.12}$$

Step Seven: Compute the Fracture Porosity

Use Equation 5.16 to compute the fracture porosity. If there is not a fracture density datum, D_f, available, the fracture porosity can be estimated from well logging by using as the fracture porosity the difference between neutron and sonic porosities, Equation 2.3.

$$\phi_f = \frac{D_f 4\pi\alpha_f}{3} \tag{5.16}$$

$$\phi_f = \phi_t - \phi_m = \phi_{Neu} - \phi_{Son} \tag{2.3}$$

Step Eight: Compute the Matrix Porosity

Solve Equation 2.3 for matrix porosity and substitute.

$$\phi_m = \phi_t - \phi_f \tag{2.3}$$

Step Nine: Compute the Total Fracture Compressibility

Compute the total fracture compressibility as the dry fracture compressibility plus the compressibility of the fluid.

$$(c_t)_f = \frac{1}{K_F} + Z_{Nf}$$

Step Ten: Compute the Total Matrix Compressibility

Solve Equation 4.4 for the total matrix compressibility and substitute.

$$(c_t)_m = \frac{(\phi c_t)_f}{\phi_m}\left(\frac{1}{\omega} - 1\right)^{-1} \tag{4.4}$$

Step Eleven: Compute the Total Storage Capacity of the Rock

Solve Equation 4.4 for the total storage capacity ratio and substitute.

$$(\phi c_t)_{f+m} = \frac{(\phi c_t)_f}{\omega} \tag{4.4}$$

Step Twelve: Compute the Interporosity Flow Parameter

Use Equation 4.26.

$$\lambda = \frac{42.5h(\phi c_t)_{f+m}\, r_w^2}{qB}\left(\frac{t * \Delta P'}{t}\right)_{\min} \tag{4.26}$$

Step Thirteen: Compute the Average Reservoir Permeability

Use Equation 4.24.

$$k = \frac{70.6 q \mu B_o}{h(t^* \Delta p')_r} \tag{4.24}$$

Step Fourteen: Compute the Skin Factor

Use Equation 4.28.

$$s = \frac{1}{2}\left[\frac{\Delta P_r}{(t^* \Delta P')_r} - \ln\left(\frac{k\, t_r}{\mu (\phi c_t)_{f+m} r_w^2}\right) + 7.43\right] \tag{4.28}$$

Step Fifteen: Compute the Reduction in Fracture Porosity Due to Depletion

From Equation 2.15, the ratio between current and initial fracture porosity is estimated.

$$\frac{\phi_f}{\phi_{f\,i}} = e^{-(c_t)_f (P_i - \overline{P})} \tag{2.15}$$

Computations at Initial in-Situ Stress Conditions

Step Sixteen: Compute the Effective in-Situ Stress

The change in effective stress due to depletion is computed as:

$$\Delta p_e = \overline{p} - p_i$$

Step Seventeen: Compute the Initial Average Reservoir Permeability

The average permeability at initial reservoir conditions can be computed using Equation 3.11.

$$k_i = \frac{k}{e^{-\frac{3}{2}(c_t)_f (Pi-\overline{P})}} \tag{3.11}$$

Step Eighteen: Compute the Matrix Porosity

The porosity reduction of the matrix due to changes in the effective stress is computed using Equation 2.17.

$$\Delta\phi_m = 1 - \phi_{m_i} e^{-(c_t)_m (Pi-\overline{P})} \tag{2.17}$$

6.2 APPLICATION EXAMPLE

Cardona *et al.*[28] presented pressure data for the Wyebourn field, a carbonate reservoir consisting of a 30m (98.4ft) interval of dolomite and limestone. From production, core and borehole data, there is enough evidence that the reservoir is fractured. Appendix C presents the pressure data table acquired at one of the wells during a pressure buildup test. The well is primarily a water producer (oil/water ratio=0.02). Prior to shutting-in for the test, this well had produced 600,000 STB of water during one year and eight months. From core analysis measurements, the total porosity is 20% and the aspect ratio of the cracks, α_f = 3x10^{-4}. An azimuthal AVO analysis determined that fracture density, D_f, is 0.03. Production records indicate that the initial reservoir pressure was 5500 psi. Additional well, reservoir and fluid data are:

True vertical depth (TVD) = 1634 m (5360 ft)

μ = 1.0 cp

B =1.01 RB/STB

ρ = 8.65 lbm/gal (1.04 gm/cm^3)

r_w = 0.333 ft

a) At current in-situ stress conditions compute:

1) Average pore pressure.

2) Effective stress.

3) Wellbore storage coefficient.

4) Storage capacity ratio.

5) Compressibility of the reservoir fluid.

6) Normal compliance of the fracture.

7) Fracture porosity.

8) Matrix porosity.

9) Total fracture compressibility.

10) Total matrix compressibility.

11) Total storage capacity of the rock.

12) Interporosity flow parameter.

13) Average reservoir permeability.

14) Skin factor.

15) Reduction in fracture porosity due to depletion.

b) At initial in-situ stress conditions compute:

16) Effective in-situ stress.

17) Initial average reservoir permeability.

18) Matrix porosity reduction.

SOLUTION:

6.2.1 Computations at Current in-Situ Stress Conditions

Step One: Compute the Pore Pressure

From the pressure buildup test, perform a Horner analysis and determine the current average reservoir pressure.

$$t_p = (365 + 8(30))day = 605days = 14520hr$$

$$q = \frac{600{,}000STB}{605days} = 992STB/day$$

Figure 6.1 presents the linear plot of the flow rates and shut-in pressure vs. production time, and Figure 6.2 the corresponding Horner plot.

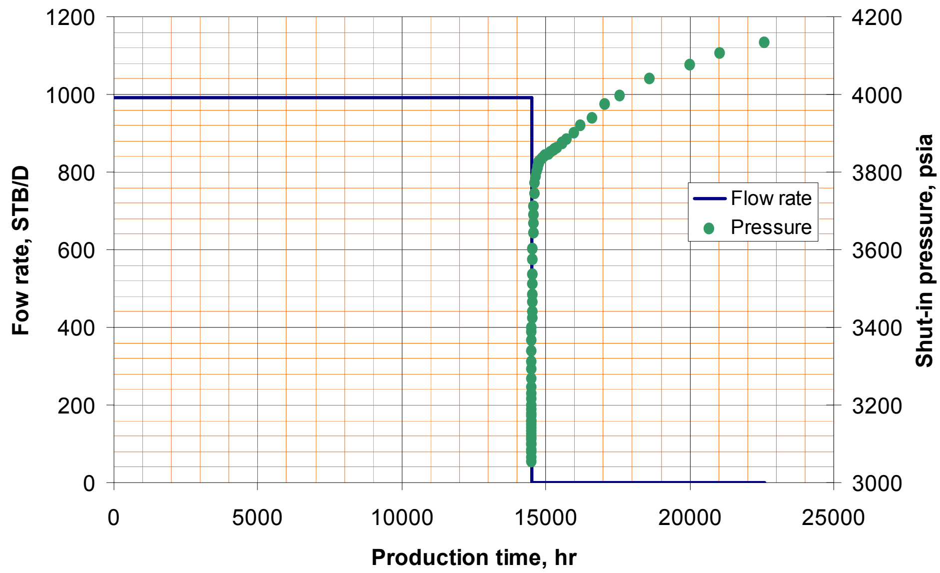

Figure 6.1. Cartesian plot of flow rate and shut-in pressure vs. production time.

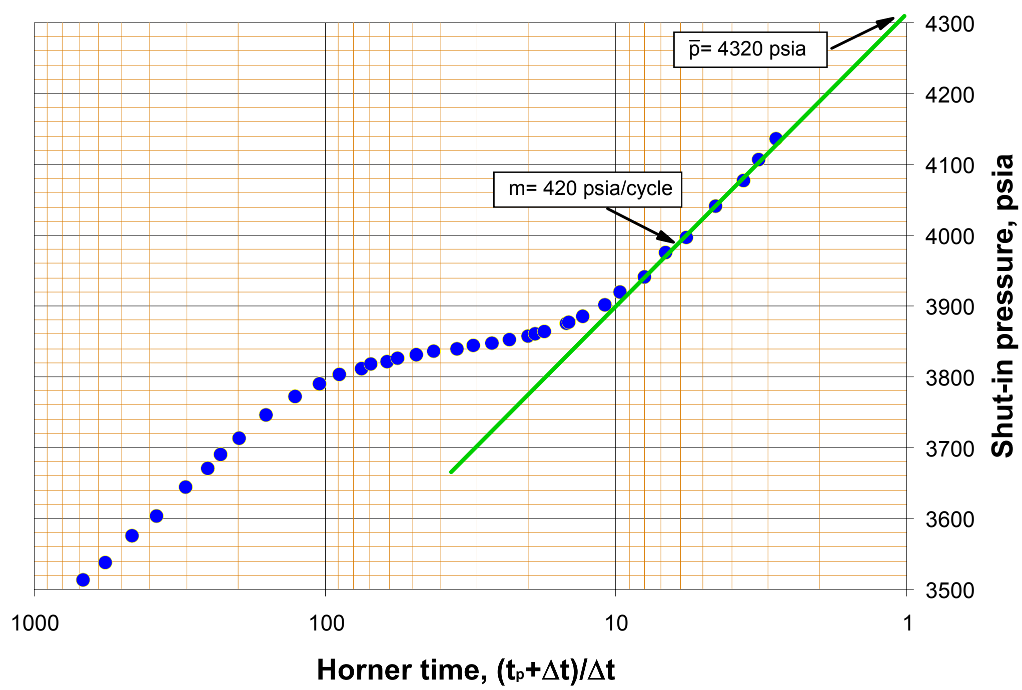

Figure 6.2. Horner plot.

The current average reservoir pressure corresponds to the current pore pressure. As shown on the Horner plot, the current average reservoir pressure is 4320 psia.

Step Two: Compute the Confining Pressure

There is not a density log available. Thus, a constant density of the rock of 2.3 gm/cm^3 is assumed, which corresponds to a lithostatic gradient of 1 psi/ft.

$$p_c = (0.052)(5260)(1) = 5260\,psi$$

Using Terzaghi's[17] law (Equation 2.8), the effective stress is computed as:

$$p_e = p_c - p_p = 5260 - 4320 = 940\,psi$$

Step Three: Compute the Wellbore Storage Coefficient

Use the *Tiab's direct synthesis technique*[27]; on the derivative plot, identify the characteristic values, see Figure 6.3.

From the log-log plot of ΔP vs. t, presented in Figure 6.3, one of the points on the early unit slope line is identified at the coordinates:

t_i = 0.69 hr

ΔP_i = 144.8 psi

The wellbore storage is computed using Equation 4.27.

$$C = \left(\frac{qB}{24}\right)\frac{t}{\Delta P} = \left(\frac{(992)(1.01)}{24}\right)\frac{0.69}{144.8} = 0.199\,STB/psi$$

The unit slope straight line in the pressure derivative plot at the beginning of the test confirms the presence of wellbore storage.

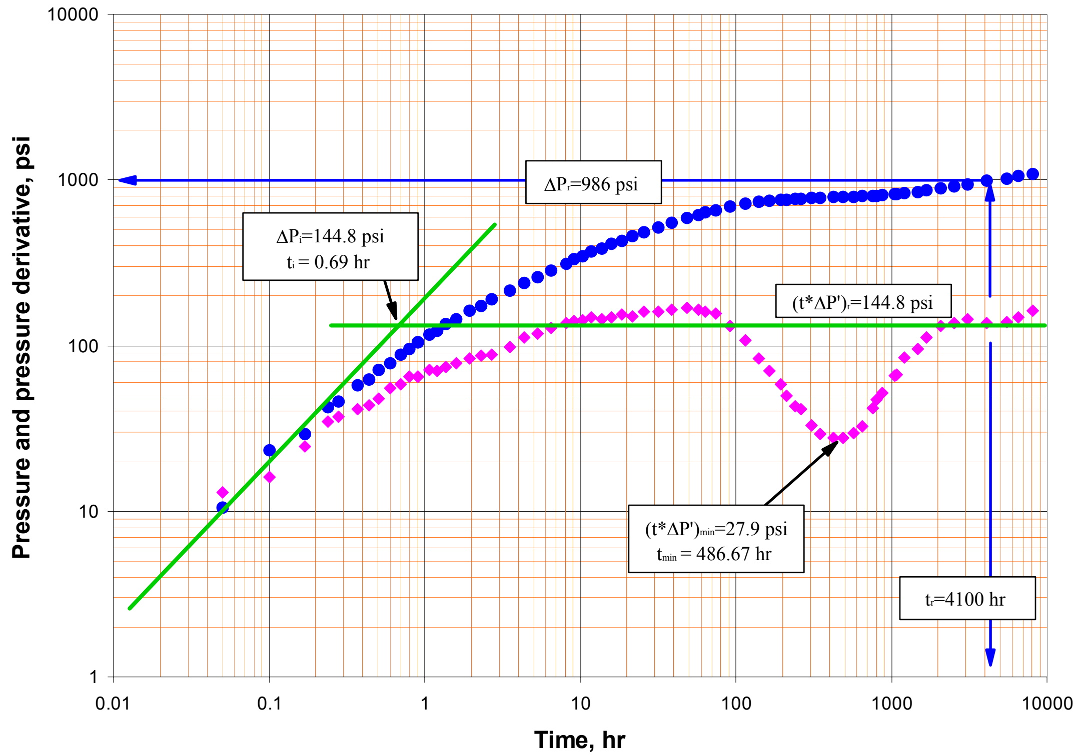

Figure 6.3. Pressure derivative plot.

Step Four: Compute the Storage Capacity Ratio

On the pressure derivative plot (Figure 6.3), the following characteristic values are read:

$(t^*\Delta p')_{min} = 27.9$ psi

$t_{min} = 486.67$ hr

$(t^*\Delta p')_r = 144.8$ psi

Compute the storage capacity ratio using Equation 4.25,

$$\omega = 0.15866\left\{\frac{(t*\Delta P')_{\min}}{(t*\Delta P')_r}\right\} + 0.54653\left\{\frac{(t*\Delta P')_{\min}}{(t*\Delta P')_r}\right\}^2$$

$$\omega = 0.1586\left(\frac{27.9}{144.8}\right) + 0.54653\left(\frac{27.9}{144.8}\right)^2 = 0.05$$

In this case, is very risky to perform the computation of the storage capacity ratio using semilog analyses, because the apparent first and the second straight lines in the Horner and MDH plots are not parallel.

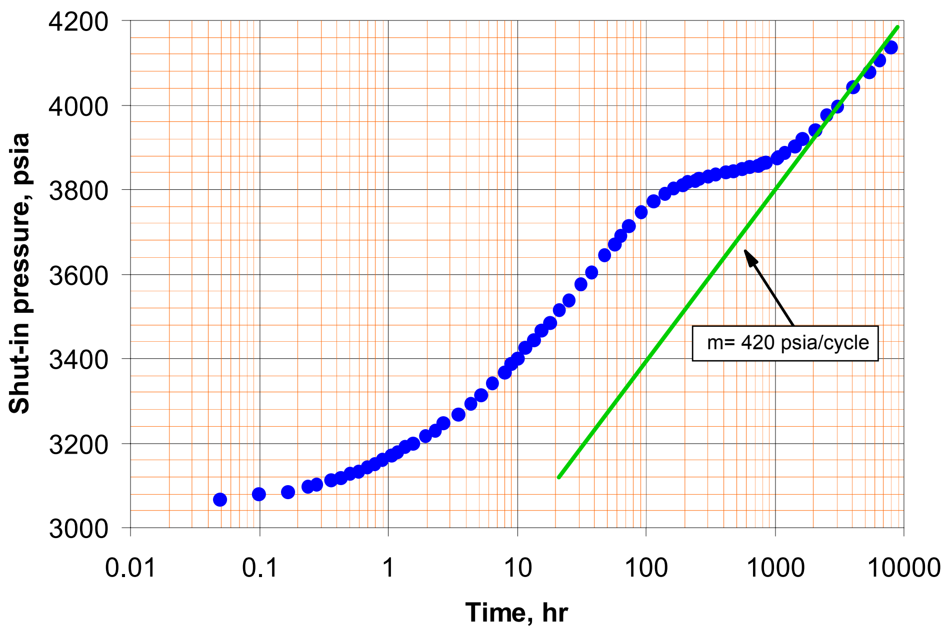

Figure 6.4. MDH plot.

Step Five: Compute the Compressibility of The Reservoir Fluid

From the physical properties of the fluids determine the velocity of the sound across them. For mixtures of different fluids use mixing laws to compute the sound velocity. Harmonic average, equivalent to Reuss isostress average, is used for modulii of fluids.

In this instance, the reservoir fluid is salty water, which has compressional wave velocity, V_p = 1.62 km/sec, and shear-wave velocity, V_s = 0 (fluids do not have shear), substituting into Equation 5.13 the bulk modulus of the fluid is found.

$$K = \rho\left(V_p^2 - \frac{4}{3}V_s^2\right)$$

$$K_{water} = 1.04\left(1.62^2\right) = 2.73GPa\frac{10^6\,psi}{68.95GPa} = 3.96x10^4\,psi$$

Then, the compressibility of the reservoir fluid is:

$$c_w = \frac{1}{K_{water}} = 2.53x10^{-5}\,psi^{-1}$$

Step Six: Compute the Normal Compliance of the Fracture

Solving Equation 5.12 for the normal compliance of the fracture yields:

$$c_{pp,f} = Z_{Nf} = \left(\frac{\omega}{1-\omega}\right)\frac{\phi_T}{K_F} = \left(\frac{0.05}{1-0.05}\right)\frac{0.2}{2.73GPa} = 0.0038GPa^{-1}$$

Step Seven: Compute the Fracture Porosity

Solving Equation 5.16 for fracture porosity results to:

$$\phi_f = \frac{D_f 4\pi\alpha_f}{3} = \frac{(0.03)(4\pi)(3x10^{-4})}{3} = 3.77x10^{-5} = 0.0037\% \approx 0$$

Step Eight: Compute the Matrix Porosity

Solving Equation 2.3 for matrix porosity and substituting becomes:

$$\phi_m = \phi_t - \phi_f = 0.2 - 3.7x10^{-5} \approx 0.2 \therefore \phi_t \approx \phi_m$$

Equation 2.3 indicates that the matrix provides almost all the pore space of the rock.

Step Nine: Compute the Total Fracture Compressibility

As shown in Equation 5.6, the normal fracture compliance corresponds to the dry fracture compressibility of the rock. Thus, the total fracture compressibility is the dry fracture compressibility plus the compressibility of the fluid.

$$(c_t)_f = \frac{1}{K_F} + Z_{Nf} = \left(\frac{1}{2.73} + 0.0038\right) GPa^{-1} x \frac{68.95 GPa}{10^6 \, psi} = 2.55x10^{-5} \, psi^{-1}$$

Step Ten: Compute the Total Matrix Compressibility

Solve Equation 4.4 for the total matrix compressibility and substitute.

$$(c_t)_m = \frac{(\phi c_t)_f}{\phi_m}\left(\frac{1}{\omega} - 1\right) = \frac{(3.77x10^{-5})(2.55x10^{-5})}{0.2}\left(\frac{1}{0.05} - 1\right) = 9.13x10^{-8} \, psi^{-1}$$

$$\frac{(c_t)_f}{(c_t)_m} = \frac{2.56x10^{-5}}{9.13x10^{-8}} = 280.4$$

In this reservoir the total fracture compressibility is 280 folds higher than the total matrix compressibility.

Step Eleven: Compute the Total Storage Capacity of the Rock

From Equation 4.4:

$$(\phi c_t)_{f+m} = \frac{(\phi c_t)_f}{\omega} = \frac{(3.77x10^{-5})(2.55x10^{-5})}{0.05} = 1.92x10^{-8}\, psi^{-1}$$

Step Twelve: Compute the Interporosity Flow Parameter

It can be computed from TDS using Equation 4.26:

$$\lambda = \frac{42.5h(\phi c_t)_{f+m}\, r_w^2}{qB}\left(\frac{t*\Delta P'}{t}\right)_{\min} = \frac{(42.5)(98.4)(1.93x10^{-8})(0.333)^2}{(992)(1.01)}\left(\frac{27.9}{486.67}\right)$$

$$\lambda = 5.12x10^{-10}$$

Step Thirteen: Compute the Average Reservoir Permeability

From TDS using Equation 4.24:

$$k = \frac{70.6q\mu B_o}{h(t*\Delta p')_r} = \frac{(70.6)(992)(1.0)(1.01)}{(98.4)(144.8)} = 4.96md$$

From semilog analysis, using the slope of the Horner plot (Figure 6.2) and Equation 4.11:

$$k = \frac{162.6q\mu B}{mh} = \frac{(166.6)(992)(1.0)(1.01)}{(420)(98.4)} = 3.95md$$

Both analyses provide similar values; however, since the pressure derivative provides more exact solutions than semilog analyses, the value of 4.96 md is used in further computations.

Step Fourteen: Compute the Skin Factor

The mechanical skin factor is determined from the *Tiab's Direct Synthesis Technique*[27].

On the pressure derivative plot of Figure 6.3, the following values are read:

$\Delta p_r = 986$ psi

$t_r = 4100$ hr

The skin factor is computed substituting into Equation 4.28:

$$s = \frac{1}{2}\left[\frac{\Delta P_r}{(t^*\Delta P')_r} - \ln\left(\frac{k\,t_r}{\mu(\phi c_t)_{f+m} r_w^2}\right) + 7.43\right]$$

$$s = \frac{1}{2}\left[\frac{986}{144.8} - \ln\left(\frac{(4.96)(4100)}{(1)(1.92x10^{-8})(0.333^2)}\right) + 7.43\right] = -7.82$$

The negative skin factor indicates that well has been stimulated.

Step Fifteen: Compute the Reduction in Fracture Porosity Due to Depletion

From Equation 2.15, the ratio between current and initial fracture porosity is estimated.

$$\frac{\phi_f}{\phi_{f_i}} = e^{-(c_t)_f (P_i - \overline{P})} = e^{-(2.55x10^{-5})(800)} = 0.98$$

It means that fracture porosity has reduced 2% due to depletion.

6.2.2 Computations at Initial in-Situ Stress Conditions

Step Sixteen: Compute the Effective Stress

The change in effective stress due to depletion can be estimated as:

$$\Delta p_e = \overline{p} - p_i = 4320 - 5200 = -880\, psi$$

The computation of effective stress shows that at initial in-situ stress condition the effective stress was 880 psi lower than at current conditions, then the initial effective stress was:

$$(p_e)_i = p_e + \Delta p_e = 940 - 880 = 60\, psi$$

Step Seventeen: Compute the Initial Average Reservoir Permeability

From Equation 3.11, the average permeability at initial reservoir conditions can be computed.

$$k_i = \frac{k}{e^{-\frac{3}{2}(c_t)_f (Pi - \overline{P})}} = \frac{4.96}{e^{-\frac{3}{2}(2.35x10^{-5})(880)}} = 5.13 md$$

As a consequence of depletion of 880 psi, and under the condition that matrix permeability remains unchanged and is very low compared to fracture permeability, the reservoir has reduced its fracture permeability by 4%.

Step Eighteen: Compute the Matrix Porosity

From Equation 2.17, the porosity reduction of the matrix due to changes in the effective stress is estimated.

$$\Delta\phi_m = 1 - \phi_{m_i} e^{-(c_i)_m (Pi - \overline{P})} = 1 - e^{-(9.13x10^{-8} psi^{-1})(880 psi)} = 8x10^{-5} \approx 0$$

Thus, this is not a significant reduction in matrix porosity due to depletion, which validates the assumption that changes in matrix porosity and matrix compressibility are negligible.

7 EFFECTS OF PRESSURE DEPLETION ON RECOVERY IN NATURALLY FRACTURED RESERVOIRS

Previous chapters concentrated with methods to compute the fracture and matrix parameters under changes in effective stress due to reservoir depletion. In this chapter, their repercussions on hydrocarbon recovery are analyzed for gas, undersaturated and saturated naturally fractured reservoirs.

The link between the elastic behavior of the rock and the recovery predictions in the material balance modeling resides in the effective compressibility term and the storage capacity ratio. Therefore, to model the effect of changes in stress due to changes in pore pressure in the fracture system, the general volumetric material balance equation must be modified using the correct effective compressibilities of the fracture rock as follows:

The general material balance equation, initially presented for homogeneous reservoirs by Schilthuis[35], is improved to take into account the volumes contained inside the fracture and matrix systems in a naturally fracture reservoir.

$$\left[N_f(B_t - B_{ti}) + \frac{N_f m B_{ti}}{B_{gi}}(B_g - B_{gi}) + (1+m)N_f B_{ti} c_{e,f}\Delta\bar{p} + W_{e,f}\right]$$
$$+\left[N_m(B_t - B_{ti}) + \frac{N_m m B_{ti}}{B_{gi}}(B_g - B_{gi}) + (1+m)N_m B_{ti} c_{e,m}\Delta\bar{p} + W_{e,m}\right] = \quad (7.1)$$
$$N_p[B_t + (R_p - R_{soi})B_g] + B_w W_p$$

Where:

$$c_{e,f} = \frac{c_w S_{wi} + c_{pp,f}}{1 - S_{wi}} \quad (7.2)$$

$$c_{e,m} = \frac{c_w S_{wi} + c_{pp,m}}{1 - S_{wi}} \quad (7.3)$$

$$c_{pp,(f+m)} = c_{pp,f} + c_{pp,m} \quad (7.4)$$

$$N = N_f + N_m \quad (7.5)$$

And:

$N =$ initial reservoir oil, STB.

$N_f =$ initial reservoir oil in the fractures, STB.

$N_m =$ initial reservoir oil in the matrix, STB.

$B_{oi} =$ initial oil formation volume factor, rb/STB.

$N_p =$ cumulative produced oil, STB.

$B_o =$ oil formation volume factor, rb/STB.

$B_{gi} =$ initial gas formation volume factor, rb/SCF.

$R_{soi} =$ initial solution gas-oil ratio, SCF/STB.

$R_p =$ cumulative produced gas-oil ratio, SCF/STB.

R_{so} = solution gas-oil ratio, SCF/STB.

B_g = gas formation volume factor, rb/SCF.

W = initial reservoir water, rb.

W_p = cumulative produced water, STB.

B_w = water formation volume factor, rb/STB.

W_e = water influx into reservoir, rb.

c_w = water isothermal compressibility, psi^{-1}.

$c_{e,f}$ = effective compressibility of the fracture system, also known as the rock expansion term due to changes in rock and water compressibility of the fracture rock system, psi^{-1}.

$c_{e,m}$= effective compressibility of the matrix system, also known as the rock expansion term due to changes in rock and water compressibility of the matrix, psi^{-1}.

$c_{e,(m+f)}$ = effective compressibility of the fractured rock system, also known as the rock expansion term due to changes in rock and water compressibility (matrix + fracture), psi^{-1}.

$c_{pp,(f+m)}$ = fracture rock system (matrix + fracture) isothermal pore compressibility, psi^{-1}.

$c_{pp,f}$ = fracture isothermal pore compressibility, psi^{-1}.

$c_{pp,m}$ = matrix isothermal pore compressibility, psi^{-1}.

$\Delta\overline{p}$ = change in average reservoir pressure ≈ change in effective stress.

S_{wi} = initial water saturation.

m = ratio of the initial gas cap volume to the initial oil volume.

The first term inside the square parentheses on the left side of Equation 7.1 accounts for the change in the fracture system (oil volume, gas expansion, rock volume changes due to changes in effective stress (changes in pore pressure), and water influx drive mechanisms in the fracture). The second term inside the square parenthesis accounts for the drive mechanisms inside the matrix system. The right-hand side of Equation 7.1 accounts for the cumulative amount of oil, gas and water produced or injected.

Equation 7.1 can be rearranged and applied to any kind of reservoir. This study concentrates in the single phase gas, undersaturated, and saturated naturally fractured reservoirs.

7.1 SINGLE PHASE GAS RESERVOIRS

The general material balance equation (Equation 7.1) can be modified and rearranged for gas reservoirs recognizing that $NmB_{ti} = GB_{gi}$ and that $N_p R_p = G_p$; therefore, when there is no initial oil amount, $N = N_p = 0$, which leads to the following general material balance equation for a naturally fractured gas reservoir:

$$\begin{aligned}
&\left[G_f (B_g - B_{gi}) + GB_{gi} \left(\frac{c_w S_{wi,f} + c_{pp,f}}{1 - S_{wi,f}} \right) \Delta\overline{p} + W_{e,f} \right] \\
&+ \left[G_m (B_g - B_{gi}) + GB_{gi} \left(\frac{c_w S_{wi,m} + c_{pp,m}}{1 - S_{wi,m}} \right) \Delta\overline{p} + W_{e,m} \right] \\
&= G_p B_g + B_w W_p
\end{aligned} \tag{7.6}$$

Assuming a volumetric reservoir (no water encroachment), Equation 7.6 reduces to:

$$G_f\left\lfloor B_g + B_{gi}(c_{e,f}\Delta\overline{p} - 1)\right\rfloor + G_m\left\lfloor B_g + B_{gi}(c_{e,m}\Delta\overline{p} - 1)\right\rfloor = G_p B_g \tag{7.7}$$

Where:

$G =$ initial reservoir gas, SCF.

$G_p =$ cumulative gas production, SCF.

$G_f =$ initial reservoir gas in the fractures, SCF.

$G_m =$ initial reservoir gas in the fractures, SCF.

Substituting the gas volume factor definition into Equation 7.7, implying isothermal conditions, and dividing by G on both sides of the equation yields:

$$\frac{G_f}{G}\left\{\frac{z}{p} + \frac{z_i}{p_i}\left(c_{e,f}\Delta\overline{p} - 1\right)\right\} + \frac{G_m}{G}\left\{\frac{z}{p} + \frac{z_i}{p_i}\left(c_{e,m}\Delta\overline{p} - 1\right)\right\} = \frac{G_p}{G}\frac{z}{p} \tag{7.8}$$

Recalling the general definition of the storage capacity ratio (Equation 4.4), at initial reservoir conditions as proposed by Aguilera[36]:

$$\omega_i = \frac{(\phi c_t)_f}{(\phi c_t)_f + (\phi c_t)_m} = \frac{(\phi c_t)_f}{(\phi c_t)_{f+m}} \approx \frac{G_f}{G} \tag{7.9}$$

Substituting into Equation 7.8:

$$\omega_i\left\{\frac{z}{p} + \frac{z_i}{p_i}\left(c_{e,f}\Delta\overline{p} - 1\right)\right\} + (1-\omega_i)\left\{\frac{z}{p} + \frac{z_i}{p_i}\left(c_{e,m}\Delta\overline{p} - 1\right)\right\} = \frac{G_p}{G}\frac{z}{p} \tag{7.10}$$

Since Equation 7.10 is written in terms of the initial storage capacity ratio, it allows us to link the material balance formulation with pressure transient analyses performed on data collected during the early stages of reservoir production, when the first wells are intensively tested, and generally, good well test data are available.

Simplifying:

$$\frac{p}{z}\left[\omega_i(1-c_{e,f}\Delta\overline{p})+(1-\omega_i)(1-c_{e,m}\Delta\overline{p})\right]=-\frac{p_i}{z_iG}G_p+\frac{p_i}{z_i} \tag{7.11}$$

Notice, since p_i, z_i and G are constants, plotting p/z versus G_p on a Cartesian plot yields to a straight line when gas expansion is the only drive mechanism acting on the reservoir; conversely, when compressibility effects and/or water influx are not negligible its behavior in this plot deviates from a straight line.

A plot of $\frac{p}{z}\left[\omega_i(1-c_{e,f}\Delta\overline{p})+(1-\omega_i)(1-c_{e,m}\Delta\overline{p})\right]$ versus G_p takes into account the effect of the matrix and fracture compressibilities, which yields a straight line with slope $\frac{p_i}{z_iG}$, from where the initial gas in place can be estimated.

A plot of $\frac{p}{z}\left[\omega_i(1-c_{e,f}\Delta\overline{p})+(1-\omega_i)(1-c_{e,m}\Delta\overline{p})\right]$ versus $\frac{G_p}{G}$ also yields a straight line with a slope $\frac{p_i}{z_i}$, from where the recovery factor can be obtained by reading the datum corresponding at the abandonment pressure, $\left(\frac{p_a}{z_a}\right)$, as shown in Figure 7.1.

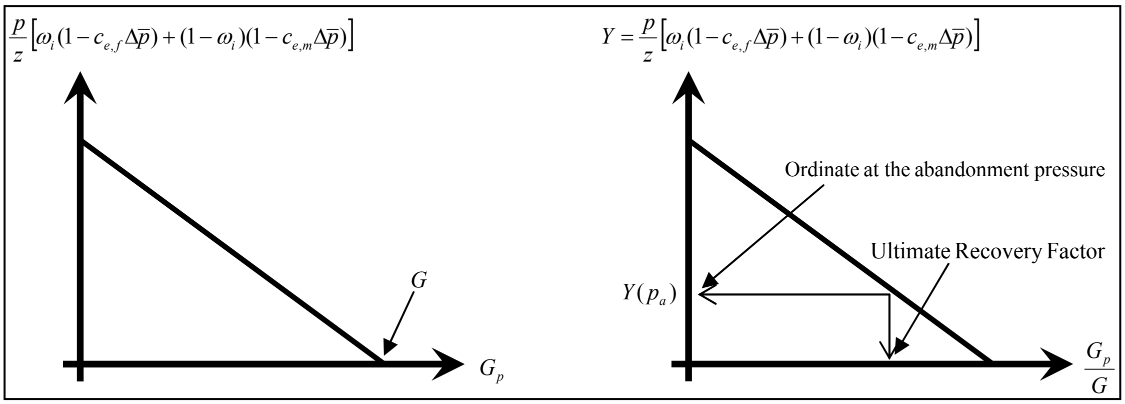

Figure 7.1. Material balance plotting schemes for gas reservoirs.

7.1.1 Field Example, Gas Reservoir

The XYZ reservoir is a stratigraphic bounded gas accumulation. The sand is generally fine-grained sublitharenite to feldspathic litharenite with minor amounts (<1%) of authigenic clay and pyrite. The reservoir fluid in the productive zone is a very lean, biogenic gas with a condensate-gas ratio of about 0.3 bbl/mmscf.

Compute the original gas in place and the recovery factors for an abandonment pressure of 2000 psi under the following conditions:

1) Negligible compressibility.
2) Effective fracture compressibility equals to effective fracture compressibility.
3) Effective fracture compressibility of 10, 20, 50, 75, and 100 folder higher than the effective matrix compressibility.

Core and borehole images have proven that this lean gas field is producing from a naturally fractured reservoir.

Core analyses show that the matrix frame of the rock has pressure dependent effective compressibility as shown in Table 7.1, and comparative fracture compliance analysis from seismic shows that the fracture rock compressibility could be 50 times higher than the matrix rock compressibility.

Table 7.1. Matrix rock dependent compressibility.

Reservoir pressure, psia	**$c_{pp,m}$, on original volume, psi^{-1}**
1000	5.00E-05
6000	5.00E-05
7000	3.50E-05
8000	1.80E-05
9000	1.50E-05
9472	1.00E-06

Table 7.2. Gas composition and properties.

Name	Mole percent	Critical temp., ºF	Critical pressure, psig	Critical volume	Acentric factor	Molecular weight
CO2	0.09999	87.93	1056.91	1.498	0.2250	44.01
C1	99.5995	-117.70	651.50	1.583	0.0129	16.04
C2	0.20005	90.12	693.11	2.784	0.0986	30.07
C3	0.04005	206.01	601.61	3.296	0.1924	44.10
C4	0.03007	297.46	530.24	4.454	0.2101	58.12
C5-C6	0.01029	441.41	465.89	5.743	0.2389	78.36
C7-C10	0.01202	566.18	386.76	7.588	0.3173	113.54
C11-C14	0.00410	770.56	328.31	8.241	0.4850	165.03
C15-C20	0.00241	935.64	254.14	11.491	0.6475	234.24
C21-C29	0.00069	1127.58	215.63	16.700	0.8881	329.95
C30+	0.00087	1151.80	92.20	41.792	0.9009	457.58

7.1.1.1 Pressure Transient Analysis (PTA)

Early production tests determined that the reservoir can be produced with only one well. The producer well was completed with permanent temperature and pressure downhole gauges, and data are available since the first day of production. The well was ramped up following the production and pressure profiles presented in Figure 7.2.

7.1.1.1.1 Pressure Buildup (PBU) Interpretations

Appendix E presents a detailed pressure transient analysis interpretation for the four available pressure buildups. As you can observe in appendix E (Figure E.0.3), the derivative curves for the four available buildups overlay each other, which indicate that there is no noticeable change in permeability during the early production history. Also, a non-Darcy skin effect is noticed, and is computed in the analysis.

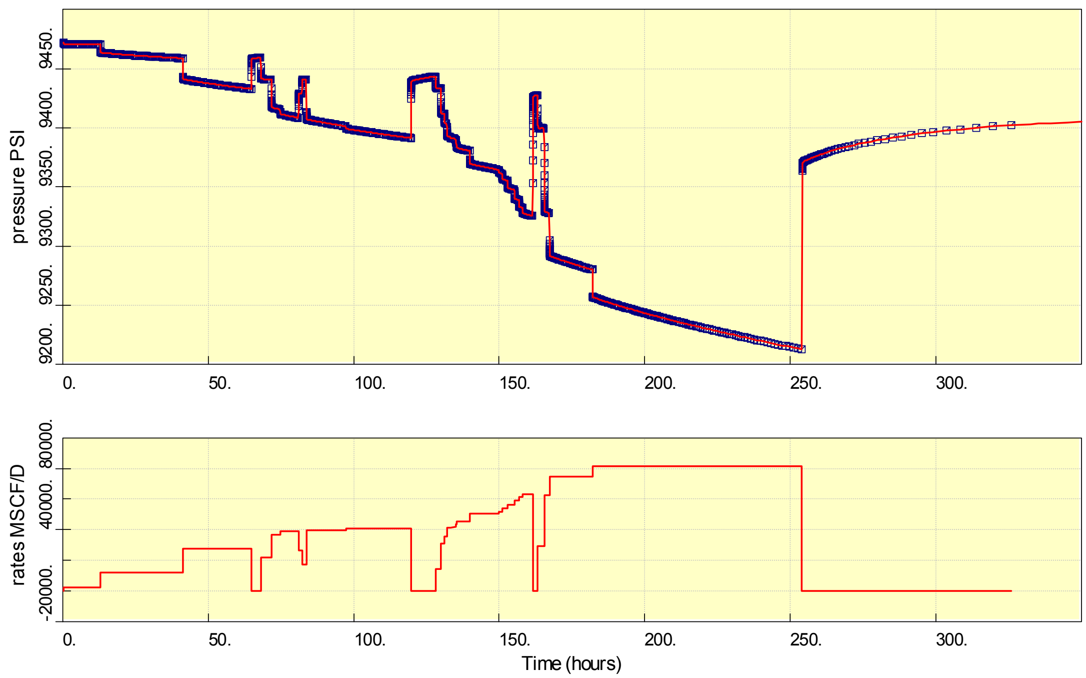

Figure 7.2. Ramping up profile.

Figure 7.3 presents the pseudopressure derivative plot for the fourth build up starting at an elapsed time of 254 hours, see Figure 7.2. The presence of a trough in the pseudopressure derivative characterizes it as a dual porosity reservoir. Furthermore, the boundary effects are masking the radial flow regime for the fractured system (matrix + fractures), so the reservoir properties were determined by mean of an analytical history match over the whole pressure history using commercial PTA software (the best analytical match is shown in figures 7.2 and 7.3).

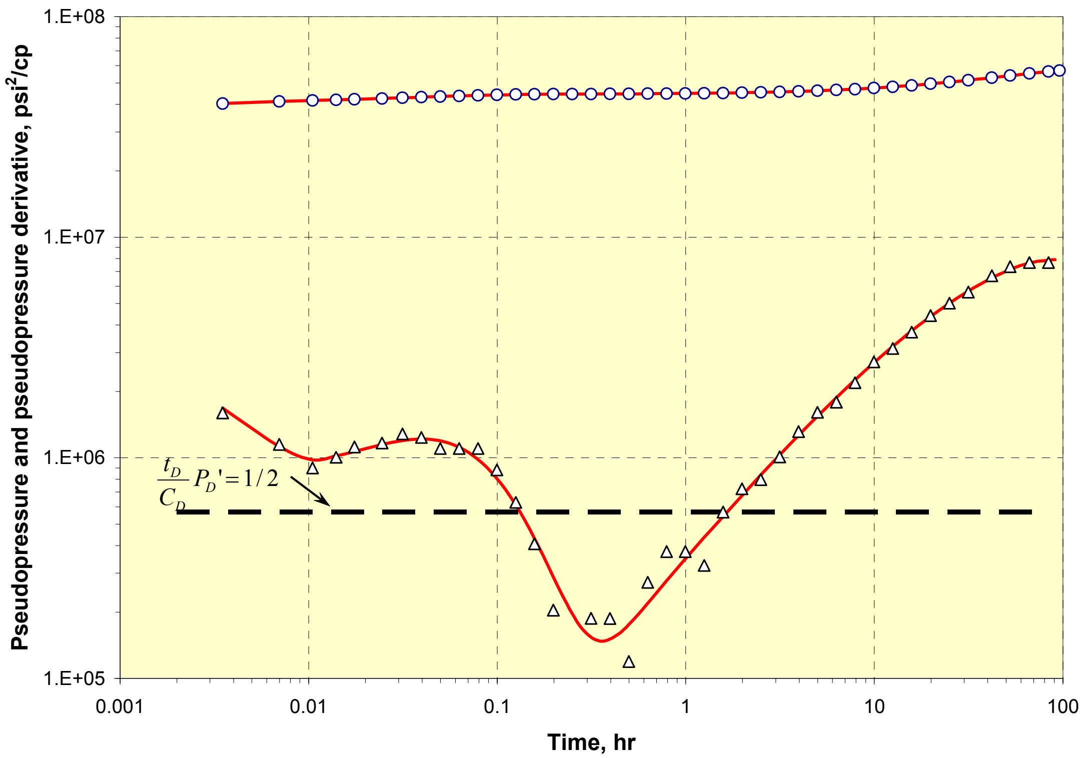

Figure 7.3. Pressure buildup number four.

Figure 7.4 depicts the boundary interpretation on the structural map, and

Table 7.3 presents a brief summary of the results obtained for the selected model in the PTA.

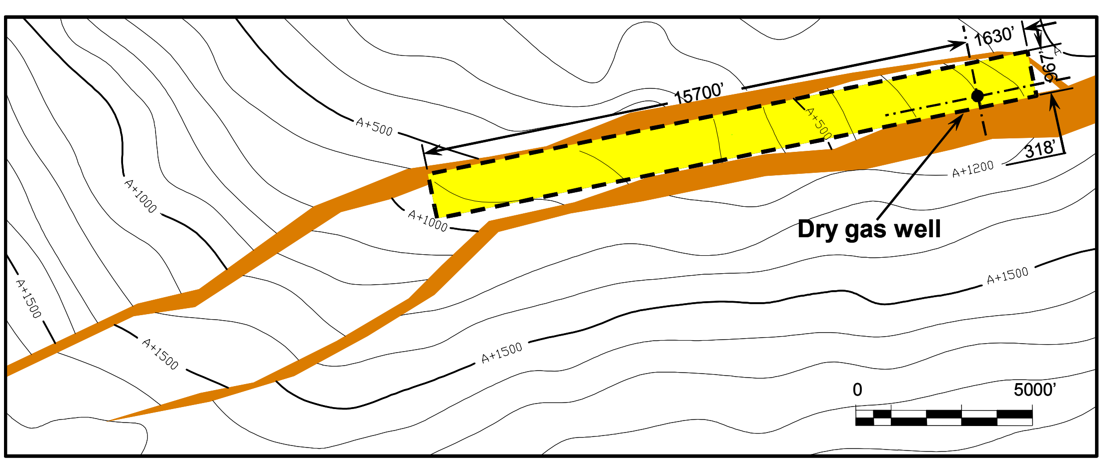

Figure 7.4. PTA interpretation on the structural map.

Table 7.3. Analytical pressure transient analysis results.

Property	**Value**
Well model	Vertical, variable skin
Reservoir model	Two porosity PSS
Boundary model	Rectangle, no flow
Main model parameters:	
Total skin	31.5
k.h, total	66900 md.ft
k, average	942 md
P_i	9472 psia
Well & wellbore parameters (tested well):	
C	0.00969 bbl/psi
Skin0 (mechanical)	3.02
Rate dependent skin gradient, d*s*/d*q*	3.5E-4 $[\text{Mscf/D}]^{-1}$
Reservoir & boundary parameters	
Storage capacity ratio, ω	0.01
Interporosity flow parameter, λ	1.03E-7
S - no flow boundary distance	318 ft
E - no flow boundary distance	1630 ft
N - no flow boundary distance	967 ft
W - no flow boundary distance	15700 ft
Derived & secondary parameters:	
Delta P (total skin)	89.08 psi
Average reservoir pressure at the end of test period	9421.01 psia

7.1.1.2 Average Reservoir Pressure and Cumulative Production History

The following cumulative production history is also available:

Table 7.4. Average reservoir pressure and cumulative production history.

Average reservoir pressure, psig	Cumulative produced gas, MMscf		Average reservoir pressure, psig	Cumulative produced gas, MMscf
9472	0		7506	31421
9461	167		7455	34039
9437	503		6777	48938
9174	4259		6531	54672
8730	10862		5584	81454
8632	12468		6180	60949
8217	20904		6109	62376
8082	22295		6084	64978
7705	27863		5084	89759

7.1.1.3 Solution

7.1.1.3.1 Assuming Negligible Compressibility

For this case, the general material balance equation becomes $\frac{p}{z} = -\frac{p_i}{z_i G} G_p + \frac{p_i}{z_i}$.

Then, a plot of $\frac{p}{z}$ versus G_p should yield a straight line where the extrapolation to $\frac{p}{z} = 0$ gives the original gas in place. Table 7.5 presents the computations, and Figure 7.5 represents the graphical model.

Extrapolating the early linear behavior to the x-axis, 330.4 bcf is estimated as the original gas in place. At an abandonment pressure of 2000 psi, the estimated ultimate recovery is 224.7 bcf, which leads to a recovery factor of 68% assuming negligible compressibility effects.

Table 7.5. P/Z computations.

Reservoir pressure, psi	**G_p, MMscf**	***P/Z*, psi**	***Z* factor**
9472	0	6946.79	1.363507
9461	167	6943.43	1.362583
9437	503	6936.08	1.360567
9174	4259	6853.97	1.338494
8730	10862	6708.27	1.301379
8632	12468	6674.83	1.293216
8217	20904	6527.65	1.258799
8082	22295	6477.71	1.247663
7705	27863	6332.46	1.216747
7506	31421	6252.11	1.200555
7455	34039	6231.09	1.196420
6777	48938	5933.30	1.142197
6531	54672	5816.03	1.122931
5584	81454	5309.77	1.051646
6180	60949	5639.12	1.095916
6109	62376	5601.87	1.090529
6084	64978	5588.64	1.088637
5084	89759	5001.22	1.016552
2000		2223.93	0.899309

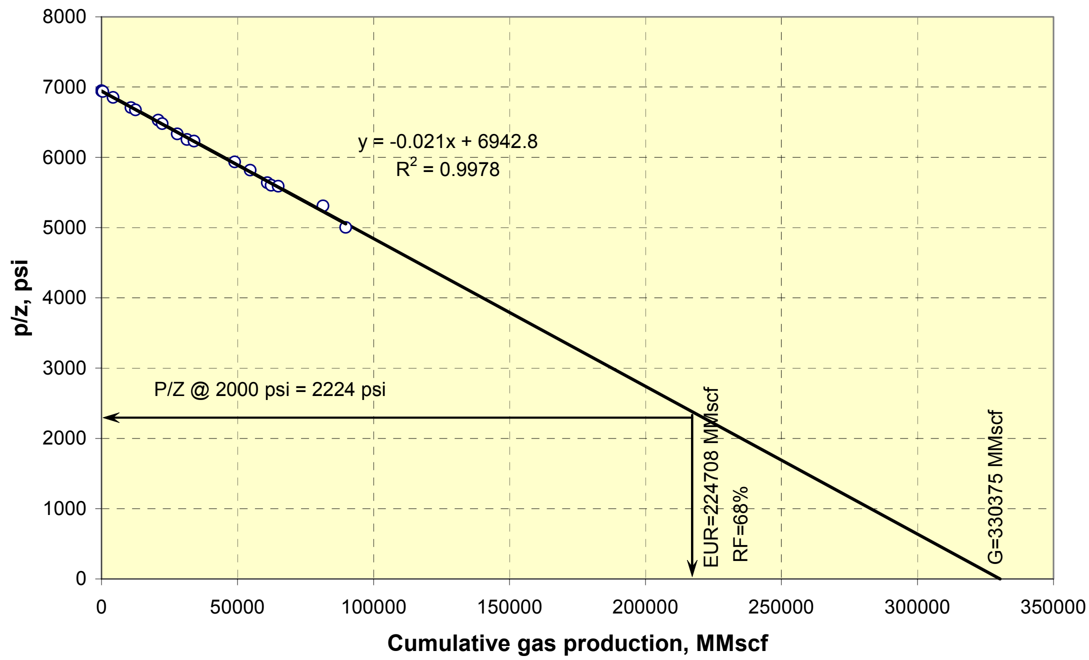

Figure 7.5. Assuming negligible compressibility case.

7.1.1.3.2 For Different Fracture / Matrix Compressibility Ratios

As an illustrative example, Table 7.6 presents the computations for the ratio $c_{pp,f}/c_{pp,m}$ = 10. Table 7.7 summarizes the results for different compressibility ratios, and Figure 7.6 displays the material balance plot for all the cases under study.

Common reservoir values for all the cases are:

S_{wi} = 0.1

Storage capacity ratio, ω = 0.01 (from PTA)

Table 7.6. Computations for $c_{pp,f}/c_{pp,m}$ = 10.

Reservoir pressure, psi	G_p, MMscf	P/Z, psi	Z	c_w, 1/psi	$c_{pp,m}$, 1/psi	$c_{e,m}$, 1/psi	$c_{pp,f}$, 1/psi	$c_{e,f}$, 1/psi	Y-AXIS, psi
9472	0	6947	1.36	3.08E-06	1.00E-06	1.5E-06	1.00E-05	1.1E-05	6947
9461	167	6943	1.36	3.08E-06	1.33E-06	1.8E-06	1.33E-05	1.5E-05	6943
9437	503	6936	1.36	3.08E-06	2.04E-06	2.6E-06	2.04E-05	2.3E-05	6935
9174	4259	6854	1.34	3.08E-06	9.84E-06	1.1E-05	9.84E-05	1.1E-04	6829
8730	10862	6708	1.30	3.07E-06	1.58E-05	1.8E-05	1.58E-04	1.8E-04	6611
8632	12468	6675	1.29	3.07E-06	1.61E-05	1.8E-05	1.61E-04	1.8E-04	6564
8217	20904	6528	1.26	3.07E-06	1.73E-05	2.0E-05	1.73E-04	1.9E-04	6353
8082	22295	6478	1.25	3.07E-06	1.78E-05	2.0E-05	1.78E-04	2.0E-04	6281
7705	27863	6332	1.22	3.06E-06	2.30E-05	2.6E-05	2.30E-04	2.6E-04	6017
7506	31421	6252	1.20	3.06E-06	2.64E-05	3.0E-05	2.64E-04	2.9E-04	5855
7455	34039	6231	1.20	3.06E-06	2.73E-05	3.1E-05	2.73E-04	3.0E-04	5812
6777	48938	5933	1.14	3.06E-06	3.83E-05	4.3E-05	3.83E-04	4.3E-04	5185
6531	54672	5816	1.12	3.05E-06	4.20E-05	4.7E-05	4.20E-04	4.7E-04	4939
5584	81454	5310	1.05	3.04E-06	5.00E-05	5.6E-05	5.00E-04	5.6E-04	4053
6180	60949	5639	1.10	3.05E-06	4.73E-05	5.3E-05	4.73E-04	5.3E-04	4569
6109	62376	5602	1.09	3.05E-06	4.84E-05	5.4E-05	4.84E-04	5.4E-04	4492
6084	64978	5589	1.09	3.05E-06	4.87E-05	5.4E-05	4.87E-04	5.4E-04	4465
5084	89759	5001	1.02	3.04E-06	5.00E-05	5.6E-05	5.00E-04	5.6E-04	3665
2000**	152756	2224	0.90	3.01E-06	5.00E-05	5.6E-05	5.00E-04	5.6E-04	1212
0	184625								0

*Y-AXIS= $\frac{p}{z}\left[\omega_i(1-c_{e,f}\Delta\bar{p})+(1-\omega_i)(1-c_{e,m}\Delta\bar{p})\right]$

** Abandonment pressure.

Table 7.7. Computation summary for several $c_{pp,f}/c_{pp,m}$ ratios.

Reservoir pressure, psi	Case a) $c_w = c_{pp,f} = c_{pp,m} = 0$ (negligible compressibility)		Case b) $c_{pp,f}/c_{pp,m}=1$		Case c) $c_{pp,f}/c_{pp,m}=10$		Case d) $c_{pp,f}/c_{pp,m}=20$	
	G_p, MMscf	Y-AXIS*	G_p, MMscf	Y-AXIS*	G_p, MMscf	Y-AXIS*	G_p, MMscf	Y-AXIS*
9472	0	6946.79	0	6947	0	6947	0	6947
9461	167	6943.43	167	6943	167	6943	167	6943
9437	503	6936.08	503	6935	503	6935	503	6935
9174	4259	6853.97	4259	6831	4259	6829	4259	6827
8730	10862	6708.27	10862	6619	10862	6611	10862	6603
8632	12468	6674.83	12468	6573	12468	6564	12468	6554
8217	20904	6527.65	20904	6367	20904	6353	20904	6337
8082	22295	6477.71	22295	6297	22295	6281	22295	6263
7705	27863	6332.46	27863	6043	27863	6017	27863	5988
7506	31421	6252.11	31421	5887	31421	5855	31421	5819
7455	34039	6231.09	34039	5846	34039	5812	34039	5774
6777	48938	5933.30	48938	5247	48938	5185	48938	5117
6531	54672	5816.03	54672	5011	54672	4939	54672	4860
5584	81454	5309.77	81454	4156	81454	4053	81454	3938
6180	60949	5639.12	60949	4657	60949	4569	60949	4472
6109	62376	5601.87	62376	4583	62376	4492	62376	4391
6084	64978	5588.64	64978	4557	64978	4465	64978	4362
5084	89759	5001.22	89759	3775	89759	3665	89759	3543
2000**	224708	2223.93	156157	1295	152756	1212	149258	1120
0	330375	0	191515	0	184625	0	177539	0

Cont.

Reservoir pressure, psi	Case e) $c_{pp,f}/c_{pp,m}$=50		Case f) $c_{pp,f}/c_{pp,m}$=75		Case g) $c_{pp,f}/c_{pp,m}$=100	
	G_p, MMscf	Y-AXIS*	G_p, MMscf	Y-AXIS*	G_p, MMscf	Y-AXIS*
9472	0	6947	0	6947	0	6947
9461	167	6943	167	6943	167	6943
9437	503	6935	503	6935	503	6935
9174	4259	6820	4259	6814	4259	6809
8730	10862	6576	10862	6554	10862	6533
8632	12468	6523	12468	6498	12468	6473
8217	20904	6290	20904	6250	20904	6211
8082	22295	6210	22295	6166	22295	6121
7705	27863	5902	27863	5831	27863	5759
7506	31421	5711	31421	5621	31421	5530
7455	34039	5660	34039	5564	34039	5469
6777	48938	4913	48938	4742	48938	4572
6531	54672	4620	54672	4420	54672	4220
5584	81454	3594	81454	3307	81454	3020
6180	60949	4179	60949	3935	60949	3691
6109	62376	4087	62376	3834	62376	3581
6084	64978	4054	64978	3798	64978	3542
5084	89759	3177	89759	2872	89759	2568
2000**	140229	843	134036	612	128766	381
0	159262	0	146735	0	136082	0

*Y-AXIS= $\frac{p}{z}\left[\omega_i(1-c_{e,f}\Delta\overline{p})+(1-\omega_i)(1-c_{e,m}\Delta\overline{p})\right]$

** Abandonment pressure.

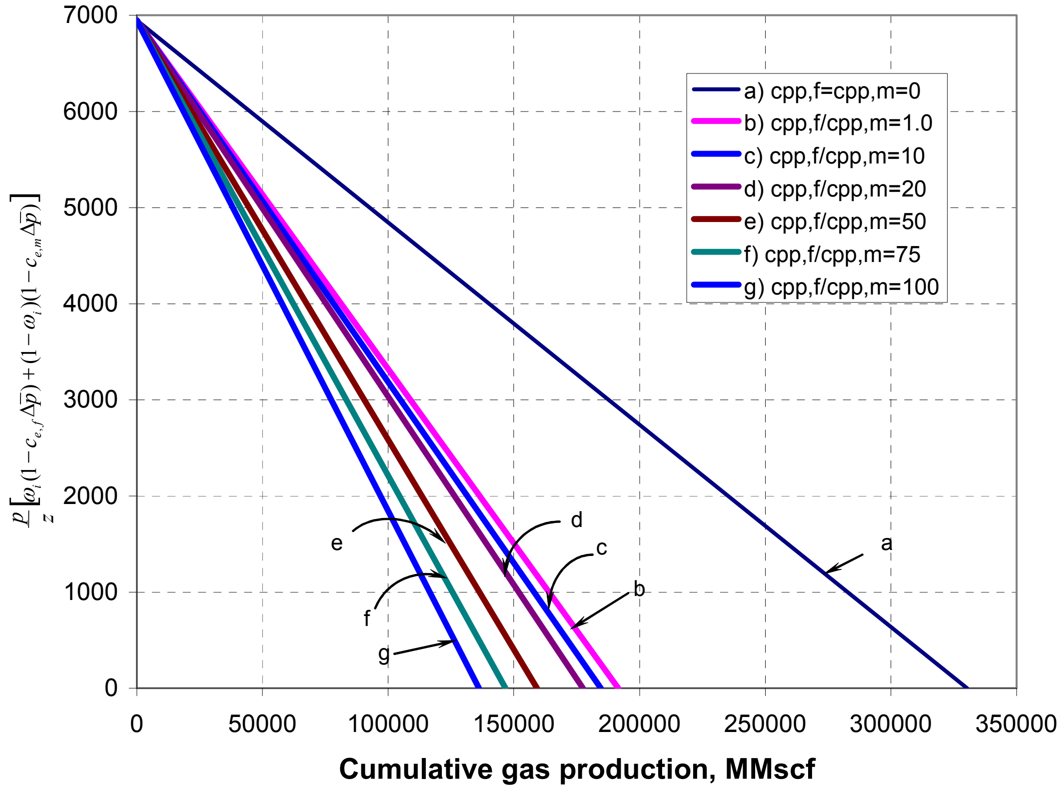

Figure 7.6. Graphical material balance representation for several fracture and matrix compressibility ratios.

Table 7.8. Comparative analysis for several $c_{pp,f}/c_{pp,m}$ ratios.

Case	$c_{ppf}/c_{pp,m}$	Original gas in place, MMscf	EUR, MMscf	Recovery factor, fraction	Error in OGIP,%	Error in EUR, %
a)	Negligible compressibility	330375	224708	0.68	107%	60%
b)	1	191515	156157	0.82	20%	11%
c)	10	184625	152756	0.83	16%	9%
d)	20	177539	149258	0.84	11%	6%
e) Base case	50	159262	140229	0.88	0%	0%
f)	75	146735	134036	0.91	8%	4%
g)	100	136082	128766	0.95	15%	8%

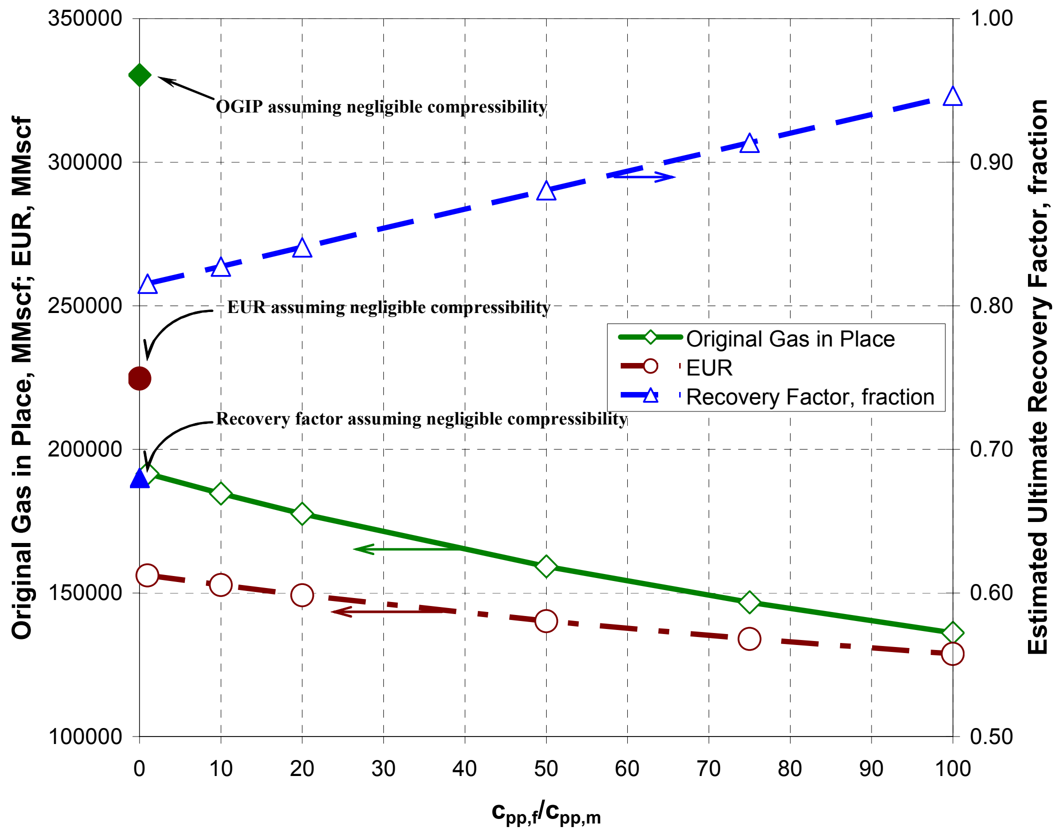

Figure 7.7. Reserves sensitivity to fracture and matrix compressibilities.

From the comparative analysis presented in Table 7.8, and the sensitivity analysis of Figure 7.7, considering the fracture to matrix compressibility ratio of 50 as the correct estimate of reserves, it can be concluded that fracture and matrix compressibilities play an important roll in the estimation of original gas in place. If no compressibility at all is taken into the material balance computation, reserves will be overestimated (for this case EUR will be 60% overestimated). Conversely, the assumption of having a fracture compressibility equal to fracture compressibility leads to significant errors (higher than 5% for this example) in the estimation of reserves for fracture to matrix pore volume compressibility ratios greater than 20.

7.2 UNDERSATURATED RESERVOIRS

When the reservoir is above the bubble pressure, there is no original free gas, m=0, and for volumetric undersaturated naturally fractured reservoirs (no water encroachment), Equation 7.1 reduces to:

$$N_f\left[(B_t - B_{ti}) + B_{ti}c_{e,f}\Delta\overline{p}\right] + N_m\left[(B_t - B_{ti}) + B_{ti}c_{e,m}\Delta\overline{p}\right] = N_p[B_t + (R_p - R_{soi})B_g] \tag{7.12}$$

Where:

$$B_t = B_o + B_g(R_{soi} - R_{so}) \tag{7.13}$$

For pressures above the bubble point, the solution gas-oil ratio R_s, remains constant, leading to B_t=B_o. Therefore, Equation 7.12 reduces to:

$$N_pB_0 = N_f\left[(B_o - B_{oi}) + B_{oi}c_{e,f}\Delta\overline{p}\right] + N_m\left[(B_o - B_{oi}) + B_{oi}c_{e,m}\Delta\overline{p}\right] \tag{7.14}$$

Equation 7.12 can also be applied to oil reservoirs below the bubble point when they have not reached critical gas saturation, and no free gas is being produced.

Defining:

$$F = N_p\left[B_t + (R_p - R_{soi})B_g\right] \tag{7.15}$$

$$E_{o,f} = (B_t - B_{ti}) + B_{ti}c_{e,f}\Delta\overline{p} \tag{7.16}$$

$$E_{o,m} = (B_t - B_{ti}) + B_{ti} c_{e,m} \Delta \bar{p} \tag{7.17}$$

Where:

$F =$ Amount of oil produced, rb.

$E_{o,f} =$ Expansion of the initial amount of oil contained inside the fractures, rb/STB.

$E_{o,m} =$ Expansion of the initial amount of oil contained inside the matrix, rb/STB.

Then, the compact expression of the material balance equation results:

$$F = N_f E_{o,f} + N_m E_{o,m} \tag{7.18}$$

Equation 7.18 says that in volumetric undersaturated naturally fractured reservoirs, the total amount of oil produced is due to the expansion of the original fluid and pore volume contained in the fracture and matrix spaces.

Penuela *et al.*[37] proposed to write the compact material balance equation in NFRs as:

$$\frac{F}{E_{o,m}} = N_f \frac{E_{o,f}}{E_{o,m}} + N_m \tag{7.19}$$

A plot of $\frac{F}{E_{o,m}}$ versus $\frac{E_{o,f}}{E_{o,m}}$ leads to a straight line with y-intercept N_m and slope N_f as represented in Figure 7.8.

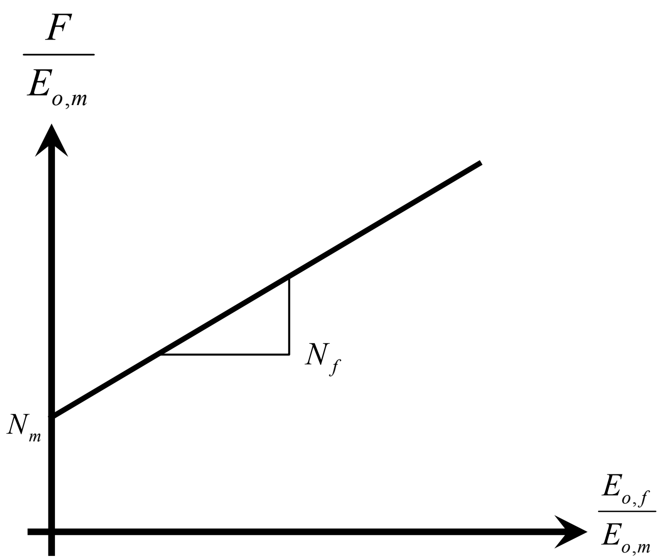

Figure 7.8. Material balance plotting scheme proposed by Penuela et al. (Reference 37)

7.2.1 The Material Balance Equation for Undersaturated Reservoirs as Function of the Storage Capacity Ratio

Dividing into the original oil in place, *N*, on both sides of Equation 7.18 yields:

$$\frac{F}{N} = \frac{N_f}{N} E_{o,f} + \frac{N_m}{N} E_{o,m} \tag{7.20}$$

Recalling once again the general definition of the storage capacity ratio (Equation 4.4), at initial reservoir conditions for an undersaturated reservoir:

$$\omega_i = \frac{(\phi c_t)_f}{(\phi c_t)_f + (\phi c_t)_m} = \frac{(\phi c_t)_f}{(\phi c_t)_{f+m}} \approx \frac{N_f}{N} \tag{7.21}$$

Substituting into Equation 7.18, and rearranging becomes:

$$F = N\left\lfloor \omega_i E_{o,f} + (1-\omega_i) E_{o,m} \right\rfloor \tag{7.22}$$

Therefore, a plot of F as the y-coordinate and $\omega_i E_{o,f} + (1-\omega_i) E_{o,m}$ as the x-coordinate would yield a straight line passing through the origin with slope N, as represented in Figure 7.9.

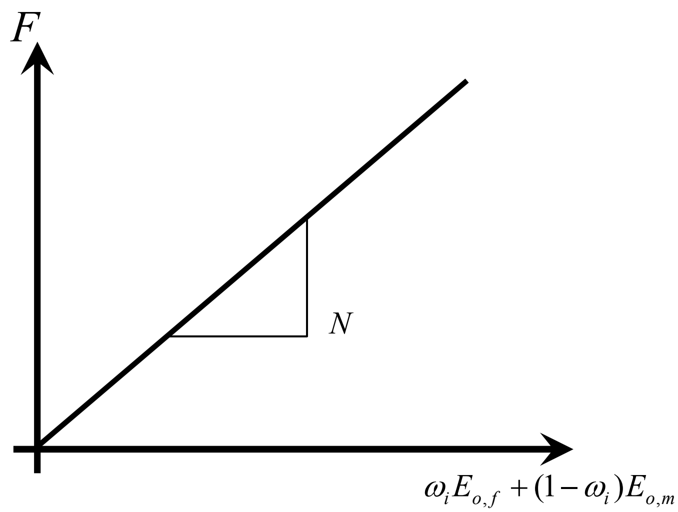

Figure 7.9. Material balance as function of storage capacity ratio for a volumetric undersaturated NFR.

When the initial storage capacity ratio can be estimated from pressure transient analysis, the new plotting method proposed in Equation 7.22 has an advantage because it requires less production data to get good estimates of the total original hydrocarbon in place than the proposed by Penuela *et al.*[37] (Equation 7.19), since only one regression parameter is needed to get the solution.

The initial oil in place in the fractures is obtained by solving Equation 7.21 for N_f, where:

$$N_f = \omega_i N \tag{7.23}$$

Taking into account that:

$$N = N_f + N_m \tag{7.24}$$

The original oil contained in the matrix pore volume is obtained from:

$$N_m = (1-\omega_i)N \tag{7.25}$$

The fractional recovery can be estimated by combining equations 7.22 and 7.15 as:

$$\frac{N_p}{N} = \frac{\omega_i E_{o,f} + (1-\omega_i)E_{o,m}}{B_t + (R_p - R_{soi})B_g} \tag{7.26}$$

Notice, when the matrix pore volume compressibility is equal to the fracture pore volume compressibility ($c_{pp,f} = c_{pp,m}$), Equation 7.26 reduces to the classical material balance equation to compute fractional recovery in homogeneous reservoirs.

$$\frac{N_p}{N} = \frac{(B_t - B_{ti}) + B_{ti}c_e\Delta\overline{p}}{B_t + (R_p - R_{soi})B_g} \tag{7.28}$$

Below the bubble point, the cumulative gas-oil ratio at any pressure is:

$$R_p = \frac{\sum \Delta N_p R}{N_p} = \frac{N_{pb}R_{so} + (N_{p1} - N_{pb})R_{avg1} + (N_{p2} - N_{p1})R_{avg2} + etc.}{N_{pb} + (N_{p1} - N_{pb}) + (N_{p2} - N_{p1}) + etc.} \tag{7.29}$$

7.2.2 Application Example, Undersaturated Reservoir

Craft and Hawkins[38] presented an example for a homogeneous undersaturated reservoir in which the effects of considering or not considering the compressibilities in the computation of recovery were analyzed. This study uses the example of a homogeneous undersaturated reservoir in a naturally fractured reservoir.

Given the following reservoir and fluid properties:

$P_i = 4000$ psia

$P_b = 2500$ psia

$S_w = 30\%$

$c_w = 3\text{x}10^{-6}$ psi^{-1}

$c_{pp,m} = 5\text{x}10^{-6}$ psi^{-1}

$\phi = 10\%$

$\omega = 0.01$

Table 7.9. PVT data.

Pressure, psia	R_{so}, SCF/STB	B_g, rb/SCF	B_t, rb/STB
4000	1000	0.00083	1.3000
2500	1000	0.00133	1.3200
2300	920	0.00144	1.3952
2250	900	0.00148	1.4180
2200	880	0.00151	1.4410

Compute the fractional recovery (N_p/N) for an undersaturated naturally fractured reservoir with no water production and negligible water influx for the following cases:

a) Negligible compressibilities.

b) Pore volume fracture compressibility equals to pore volume matrix compressibility.

c), d), e), and f) Pore volume fracture compressibility 25, 50, 75, and 100 times higher than the pore volume matrix compressibility respectively.

Assume that the critical gas saturation is not reached until the reservoir pressure drops below 2200 psia.

7.2.2.1 Solution

From the definition of effective compressibility for the matrix system:

$$c_{e,m} = \frac{c_w S_{wi} + c_{pp,m}}{1 - S_{wi}} = \frac{(3x10^{-6})(0.3) + 5x10^{-6}}{1 - 0.3} = 8.43x10^{-6}\ psi^{-1}$$

Cases a) and b)

When pore volume fracture compressibility is equal to the pore volume matrix compressibility, the solution becomes identical to the one for homogeneous reservoirs with constant pore volume compressibility. Therefore, the detailed computations presented by Craft and Hawkins[38] in their Example 5.4 (page 174 of reference 38) apply for cases a) and b) of this example. Results are reproduced in Table 7.11.

Case c) $c_{pp,f}/c_{pp,m}$=25:

$$c_{e,f} = (25)c_{pp,m} = (25)(5x10^{-6}) = 110^{-4}\ psi^{-1}$$

$$c_{e,f} = \frac{c_w S_{wi} + c_{pp,f}}{1 - S_{wi}} = \frac{(3x10^{-6})(0.3) + 1.25x10^{-4}}{1 - 0.3} = 1.80x10^{-4}\ psi^{-1}$$

The fracture and matrix expansion terms are computed using equations 7.16 and 7.17 respectively.

$$E_{o,f} = (B_t - B_{ti}) + B_{ti}c_{e,f}\Delta\overline{p} = (1.32 - 1.30) + (1.30)(1.80x10^{-4})(1500) = 0.371 rb/STB$$

$$E_{o,m} = (B_t - B_{ti}) + B_{ti}c_{e,m}\Delta\overline{p} = (1.32 - 1.30) + (1.30)(8.43x10^{-6})(1500) = 0.036 rb/STB$$

The total expansion of the fracture rock (fracture + matrix) is:

$$\omega_i E_{o,f} + (1-\omega_i)E_{o,m} = (0.01)(0.371) + (1-0.01)(0.036) = 0.040 rb/STB$$

Equation 7.28 is used to compute the fractional recovery at the bubble point:

$$\frac{N_p}{N} = \frac{\omega_i E_{o,f} + (1-\omega_i)E_{o,m}}{B_t + (R_p - R_{soi})B_g} = \frac{0.040}{1.32 + (1000-1000)0.00133} = 0.030$$

Below the bubble point, Equations 7.26 and 7.29 are used to compute the recovery.

$$\frac{N_p}{N} = \frac{\omega_i E_{o,f} + (1-\omega_i)E_{o,m}}{B_t + (R_p - R_{soi})B_g}$$

And:

$$R_p = \frac{\sum \Delta N_p R}{N_p} = \frac{\sum (\Delta N_p / N) R}{N_p / N}$$

During the depletion period from 2500 to 2300 psia, the calculations are:

$$E_{o,f} = (B_t - B_{ti}) + B_{ti}c_{e,f}\Delta\overline{p} = (1.3952 - 1.30) + (1.30)(1.80x10^{-4})(1700) = 0.493 rb/STB$$

$$E_{o,m} = (B_t - B_{ti}) + B_{ti} c_{e,m} \Delta\overline{p} = (1.3952 - 1.30) + (1.30)(8.43x10^{-6})(1700) = 0.114 rb/STB$$

The total expansion of the fracture rock (fracture + matrix) is:

$$\omega_i E_{o,f} + (1-\omega_i) E_{o,m} = (0.01)(0.493) + (1-0.01)(0.114) = 0.118 rb/STB$$

$$\frac{N_p}{N} = \frac{0.118}{0.3952 + (R_p - 1000)0.00144} \tag{7.30}$$

$$R_p = \frac{0.030(1000) + (N_p/N - 0.030)R_{ave1}}{N_p/N} \tag{7.31}$$

Where R_{ave1} is the average solution gas-oil ratio during the pressure depletion period analyzed.

$$R_{ave1} = \frac{1000 + 920}{2} = 960 \text{ SCF/STB} \tag{7.32}$$

Solving equations 7.30, 7.31 and 7.32 for the fractional recovery yields:

$$\frac{N_p}{N} = 0.087$$

Following the same procedure, the fractional recovery factors are computed for the subsequent depletion periods. Table 7.10 summarizes their computations and results.

Table 7.10. Computations summary for case c) $c_{pp,f}/c_{pp,m}$=25.

Pressure, psia	**Pressure depletion, psi**	$E_{o,f}$, ***Rb/STB***	$E_{o,m}$, ***Rb/STB***	$\omega_i E_{o,f} + (1-\omega_i)E_{o,m}$, ***Rb/STB***	R_{ave}, ***SCF/STB***	N_p/N
4000	0	0.000	0.000	0.000		0.000
2500	1500	0.371	0.036	0.040	1000	0.029
2300	1700	0.493	0.114	0.118	960	0.085
2250	1750	0.527	0.137	0.141	910	0.104
2200	1800	0.562	0.161	0.165	890	0.121

Cases d), e), and f) $c_{pp,f}/c_{pp,m}$=50, 75, and 100 Respectively:

In order to get the results for these cases, the above procedure was followed. A summary of the results for all cases is presented in Table 7.11 and plotted in Figure 7.10.

Table 7.11. Summary of results for all cases.

	Fractional Recovery					
Pressure, psia	**Case a) c_w=$c_{e,f}$=$c_{e,m}$=0 (Negligible compressibility)**	**Case b) $c_{pp,f}/c_{pp,m}$=1**	**Case c) $c_{pp,f}/c_{pp,m}$ =25**	**Case d) $c_{pp,f}/c_{pp,m}$ =50**	**Case e) $c_{pp,f}/c_{pp,m}$ =75**	**Case f) $c_{pp,f}/c_{pp,m}$ =100**
4000	0.000	0.000	0.000	0.000	0.000	0.000
2500	0.015	0.028	0.030	0.033	0.035	0.038
2300	0.071	0.084	0.087	0.089	0.092	0.095
2250	0.087	0.118	0.106	0.109	0.112	0.115
2200	0.104	0.120	0.123	0.126	0.129	0.132

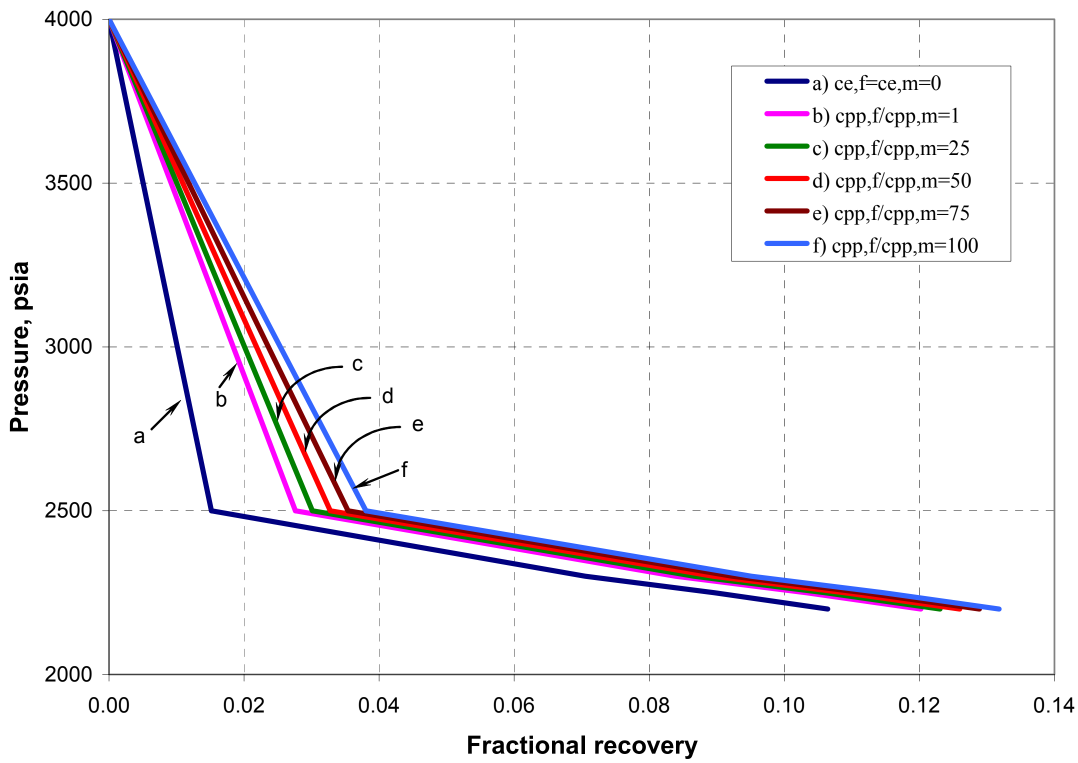

Figure 7.10. Sensitivity analysis on recovery versus pore pressure in an undersaturated NFR.

Notice from Figure 7.10 that for pressures above the bubble point, the effect of having greater fracture pore volume compressibility than the matrix pore volume compressibility in NFRs improves the fractional recovery.

7.3 SATURATED RESERVOIRS

When the reservoir pressure is below the bubble point, a free gas cap is present; as the reservoir depletes, the expansion of the gas provides extra energy to the reservoir, displacing the oil downward toward the open intervals in the wells.

Let us recall the general material balance equation (Equation 7.1), and define the following terms to express it in a compact form.

$$E_o = B_t - B_{ti} \tag{7.33}$$

$$E_g = B_g - B_{gi} \tag{7.34}$$

$$E_f = E_o + \frac{mB_{ti}}{B_{gi}} E_g + (1+m) B_{ti} c_{e,f} \Delta\overline{p} \tag{7.35}$$

$$E_m = E_o + \frac{mB_{ti}}{B_{gi}} E_g + (1+m) B_{ti} c_{e,m} \Delta\overline{p} \tag{7.36}$$

$$F = N_p [B_t + (R_p - R_{soi}) B_g] + B_w W_p \tag{7.37}$$

Where:

$E_o =$ Expansion of the oil, rb/STB.

$E_g =$ Expansion of the gas, rb/STB.

$E_f =$ Expansion of oil, gas and pore volume inside the fractures, rb/STB.

$E_m =$ Expansion of oil, gas and pore volume inside the matrix, rb/STB.

Substituting into Equation 7.1, the general material balance equation for saturated reservoirs can be rewritten in compact form as:

$$F = N_f E_f + N_m E_m + W_e \tag{7.38}$$

Following a similar approach than the one proposed by Penuela *et al.*[37] for undersaturated reservoirs, when water influx is negligible, this equation can be rewritten as:

$$\frac{F_e}{E_m} = E_f \frac{E_f}{E_m} + N_m \tag{7.39}$$

Equation 7.39 is similar to Equation 7.19, with the main difference that the matrix and fracture expansion factors now have taken into account the effects of the gas cap expansion.

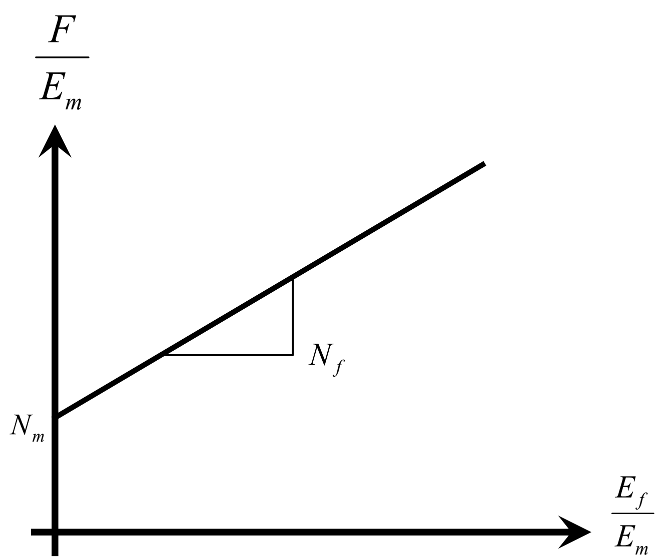

Figure 7.3. Material balance plotting scheme for saturated reservoirs. (After Penuela et al.[37])

7.3.1 The Material Balance Equation for Saturated Reservoirs as Function of the Storage Capacity Ratio

Following a similar approach that was presented previously for undersaturated reservoirs; when there is no water influx and introducing the definition of storage capacity ratio (Equation 7.21) into Equation 7.38, it becomes:

$$F = N\lfloor \omega_i E_f + (1-\omega_i)E_m \rfloor \tag{7.40}$$

The difference between equations 7.39 and 7.40 resides in the definition of the fracture and matrix expansion factors. Therefore, a plot of F as the y-coordinate and $\omega_i E_f + (1-\omega_i)E_m$ as the x-coordinate would also yield in a straight line passing through the origin with slope N, as represented in Figure 7.11.

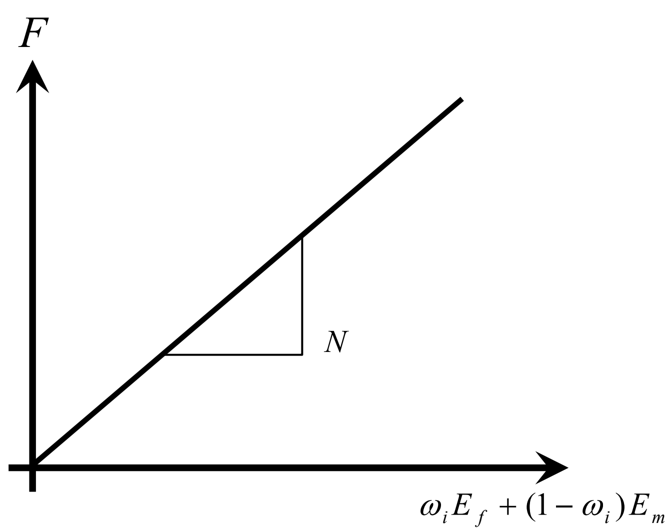

Figure 7.11. Material balance as function of storage capacity ratio for a volumetric saturated NFR.

7.3.2 Application Example, Saturated Reservoir

Craft and Hawkins[38] presented an example for a homogeneous saturated reservoir in which the compressibilities were neglected in the computation of hydrocarbons in place (Example 6.1 of reference 38). This study extends Craft and Hawkins example to a naturally fractured reservoir, and analyzes the effect of compressibilities in the estimation of hydrocarbons originally in place. In order to analyze the compressibility effects, the following were assumed: no water drive and water production.

Given:

Volume of bulk oil zone = 112000 ac-ft

Volume of bulk gas zone = 19600 ac-ft

Initial reservoir pressure = 2710 psia

Initial FVF, B_{ti} = 1.34 rb/STB

Pore volume matrix compressibility, $c_{pp,m} = 3.5 \text{x} 10^{-6}$ psi^{-1}

Connate water saturation, S_{wi} = 0.2

Initial gas volume factor, B_{gi} = 0.001116 rb/SCF

Initial dissolved GOR, R_{soi} = 562 SCF/STB

Oil produced during the interval, N_p = 20 MM STB

Reservoir pressure at the end of the interval = 2000 psia

Average produced GOR, R_p = 700 SCF/STB

Two phase FVF, B_t = 1.4954 rb/STB

FVF of the water, B_w = 1.028 rb/STB

Gas volume factor at 2000 psia, B_g = 0.001510 rb/SCF

Storage capacity ratio of the NFR, ω = 0.01

Compute the initial oil in place for the following cases:

a) Negligible compressibilities.

b) Fracture pore volume compressibility 25 times greater than the matrix pore volume compressibility.

c) Fracture pore volume compressibility 50 times greater than the matrix pore volume compressibility.

d) Fracture pore volume compressibility 75 times greater than the matrix pore volume compressibility.

e) Fracture pore volume compressibility 100 times greater than the matrix pore volume compressibility.

7.3.2.1 Solution

The volume of fluid extracted at reservoir conditions is computed using Equation 7.37:

$$F = N_p[B_t + (R_p - R_{soi})B_g] + B_w W_p$$

$$F = 20x10^6[1.4954 + (700 - 562)0.001510] + 0 = 34.07x10^6 rb = 34.07MMrb$$

The oil expansion is computed from Equation 7.33:

$$E_o = B_t - B_{ti} = 1.4954 - 1.34 = 0.1554 rb / STB$$

The gas expansion is computed from Equation 7.34:

$$E_g = B_g - B_{gi} = 0.00151 - 0.001116 = 0.000394 \text{rb/SCF}$$

Assuming the same porosity and connate water for the oil and gas zones, the ratio of the initial gas cap volume to the initial oil volume is estimated as:

$$m = \frac{\text{Volume of bulk gas zone}}{\text{Volume of bulk oil zone}} = \frac{19600}{112000} = 0.175$$

Case a) Assuming Negligible Compressibilities:

For this case, Equation 7.40 reduces to the classical MBE for saturated reservoirs:

$$F = N\left[E_o + \frac{mB_{ti}}{B_{gi}} E_g\right]$$

Solving for *N*, the original gas in place can be computed:

$$N = \frac{F}{E_o + \frac{mB_{ti}}{B_{gi}} E_g} = \frac{34075600}{0.1554 + \frac{(0.175)(1.34)}{0.001116}(0.000394)} = 143060926 = 143.06 MMSTB$$

Case b) Assuming Fracture Pore Volume Compressibility Equals to Matrix Pore Volume Compressibility:

For this case, $c_{pp,m} = c_{pp,f}$; $c_e = c_{e,m} = c_{e,f,}$ substituting into Equation 7.3 leads to:

$$c_{e,m} = \frac{c_w S_{wi} + c_{pp,m}}{1 - S_{wi}} = \frac{3x10^{-6} * 0.2 + 3.5x10^{-6}}{1 - 0.2} = 5.125x10^{-6}\, psi^{-1}$$

Furthermore, Equation 7.40 reduces to the classical MBE for saturated reservoirs with compressibility effects:

$$F = N(E_o + \frac{mB_{ti}}{B_{gi}} E_g + (1+m) B_{ti} c_e \Delta\overline{p})$$

Solving for N and substituting yields:

$$N = \frac{F}{E_o + \frac{mB_{ti}}{B_{gi}} E_g + (1+m) B_{ti} c_e \Delta\overline{p})}$$

$$= \frac{34075600}{0.1554 + \frac{(0.175)(1.34)}{0.001116}(0.000394) + (1 + 0.175)(1.34)(5.12x10^{-6})(710)}$$

$$= 139700681 = 139.70 MMSTB$$

Case c) Assuming Fracture Pore Volume Compressibility 25 Times Greater Than the Matrix Pore Volume Compressibility:

The new developed equation is used without any additional restrictions (Equation 7.40).

$$F = N\lfloor \omega_i E_f + (1 - \omega_i) E_m \rfloor$$

Where:

$$c_{pp,f} = (25)(3x10^{-6}) = 8.75x10^{-5}\ psi^{-1}$$

$$c_{e,f} = \frac{c_w S_{wi} + c_{pp,f}}{1 - S_{wi}} = \frac{3x10^{-6} * 0.2 + (8.75x10^{-5})}{1 - 0.2} = 1.10x10^{-4}\ psi^{-1}$$

$$E_f = E_o + \frac{mB_{ti}}{B_{gi}} E_g + (1+m) B_{ti} c_{e,f} \Delta\overline{p}$$

$$= 0.1554 + \frac{(0.175)(1.34)}{0.001116}(0.000394) + (1+0.175)(1.34)(1.10x10^{-4})(710) = 0.361298 rb/STB$$

$$E_m = E_o + \frac{mB_{ti}}{B_{gi}} E_g + (1+m) B_{ti} c_{e,m} \Delta\overline{p}$$

$$= 0.1554 + \frac{(0.175)(1.34)}{0.001116}(0.000394) + (1+0.175)(1.34)(5.12x10^{-6})(710) = 0.243919 rb/STB$$

Solving Equation 7.40 for N and substituting:

$$N = \frac{F}{\omega_i E_f + (1-\omega_i) E_m}$$

$$N = \frac{34075600}{(0.01)(0.361298) + (1 - 0.01)(0.243919)} = 139031631 = 139.03 MMSTB$$

Cases d), e), and f) Assuming Fracture Pore Volume Compressibility 50, 75, and 100 Times Greater Than the Matrix Pore Volume Compressibility:

Results are listed in Table 7.12, which were obtained using the procedure presented in case c.

7.3.2.2 Analysis of Results

Table 7.12 summarizes the results for all the cases.

Table 7.12. Summary of results.

Case	$c_{pp,f}$ psi^{-1}	$c_{e,f}$ psi^{-1}	$E_{o,f}$ *rb/STB*	$E_{o,m}$ *rb/STB*	**X-AXIS,** ***Rb/STB***	***N*, MMSTB**	**Fractional recovery**
a) Negligible compressibilities ($c_w = c_{pp,m} = c_{pp,f} = 0$)	0	0	0.2382	0.2382	0.2382	143.06	0.140
b) $c_{pp,f}/c_{pp,m}=1$	3.50E-06	5.13E-06	0.2439	0.2439	0.2439	139.70	0.143
c) $c_{pp,f}/c_{pp,m}=25$	8.75E-05	1.10E-04	0.3613	0.2439	0.2451	139.03	0.144
d) $c_{pp,f}/c_{pp,m}=50$	1.75E-04	2.20E-04	0.4836	0.2439	0.2463	138.34	0.145
e) $c_{pp,f}/c_{pp,m}=75$	2.63E-04	3.29E-04	0.6058	0.2439	0.2475	137.66	0.145
f) $c_{pp,f}/c_{pp,m}=100$	3.50E-04	4.38E-04	0.7281	0.2439	0.2488	136.98	0.146

*X-AXIS=$\omega_i E_f + (1-\omega_i) E_m$

Figure 7.12 displays an overlay of the plotting scheme for the material balance computations for all the cases, and Figure 7.13 presents the summary of results for original oil in place and fractional recovery.

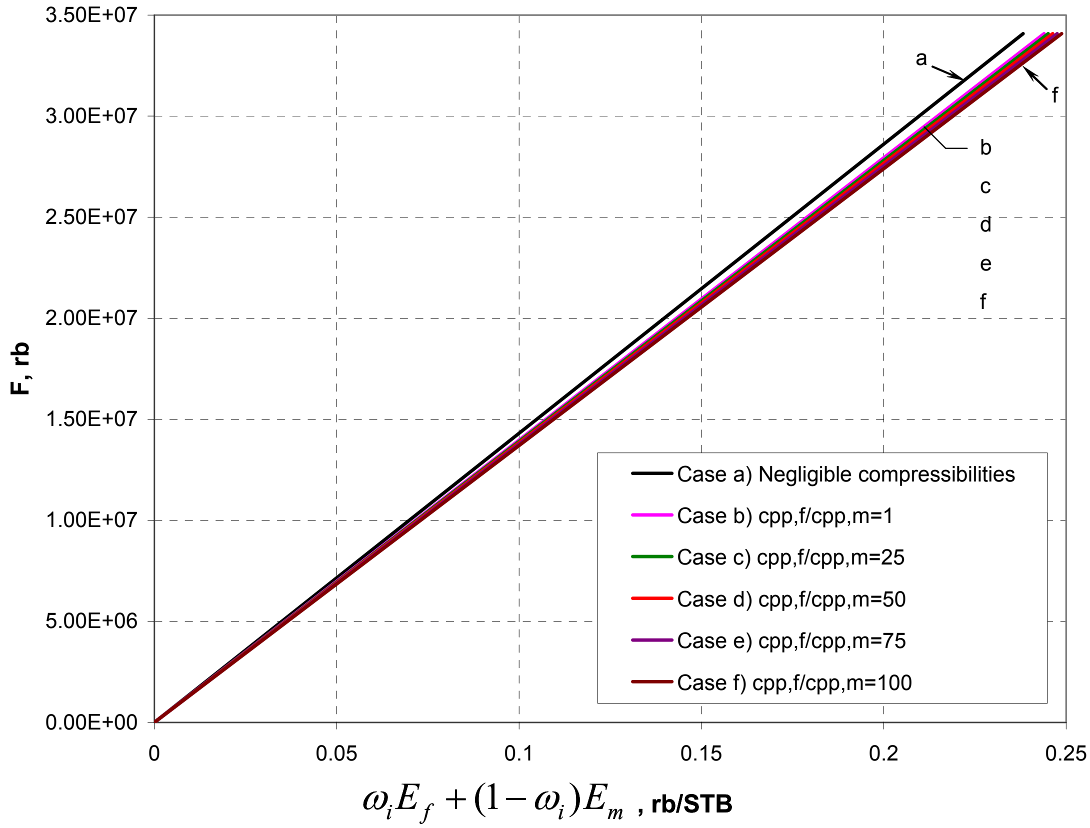

Figure 7.12. Material balance as function of storage capacity ratio for the volumetric saturated NFR example.

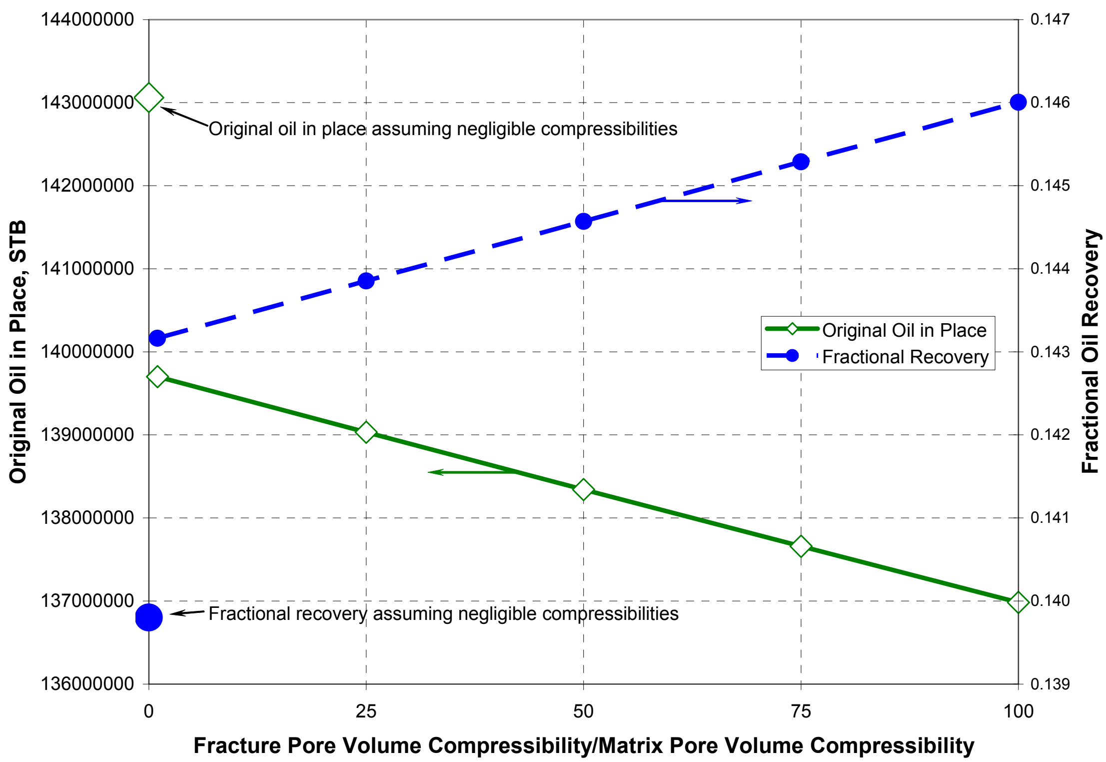

Figure 7.13. Summary of results.

From this example, the cases that were analyzed highlighted that differences between considering the effects of compressibilities and ignoring them could lead to errors in the estimation of oil in place between 2.4% and 4.2%, and errors in the estimation of fractional recovery between 2.4 and 4.4% as shown in Table 7.13.

Table 7.13. Differences in OOIP and F.R. estimations.

Case	*N*, MMSTB	Fractional recovery (F.R.)	Difference in original oil in Place, %	Difference in fractional recovery, %
a) Negligible compressibilities ($c_w = c_{pp,m} = c_{pp,f} = 0$)	143.06	0.140	0	0
b) $c_{pp,f}/c_{pp,m}=1$	139.70	0.143	2.3	2.4
c) $c_{pp,f}/c_{pp,m}=25$	139.03	0.144	2.8	2.9
d) $c_{pp,f}/c_{pp,m}=50$	138.34	0.145	3.3	3.4
e) $c_{pp,f}/c_{pp,m}=75$	137.66	0.145	3.8	3.9
f) $c_{pp,f}/c_{pp,m}=100$	136.98	0.146	4.2	4.4

In saturated naturally fractured reservoirs, the effect of fracture pore volume compressibility is inversely proportional to the original hydrocarbon in place, and directly proportional to the fractional recovery.

8 SUMMARY

8.1 CONTRIBUTIONS

Equations that model the effect of changes in stress due to pressure depletion on fracture porosity and permeability in naturally fractured reservoirs have been developed.

Tiab's Direct Synthesis Technique (*TDS*) has been complemented with more equations for quantifying the effect of stress on the fracture and matrix properties porosity, total compressibility and permeability based upon the integration between well test analysis and seismic derived normal compliance of the fracture system.

The material balance equations for gas, undersaturated, and saturated naturally fractured reservoirs have been improved to consider the effects of compressibility differences between fractured and matrix systems.

This study analyzes in detail the effect of stress on the quantification of fluid volumes stored inside the fractured rock and hydrocarbon recovery for gas, undersaturated and saturated naturally fractured reservoirs for different compressibility scenarios.

Pressure transient analysis is incorporated into the material balance equation for naturally fractured reservoirs, which allows us to determine in a more reliable way the amount of hydrocarbons in place with less production data than the classical material balance formulation.

8.2 MAIN ASSUMPTIONS

- The anisoptropic double porosity rock is composed of elastically isotropic matrix blocks separated by fractures.
- Matrix rock provides fluids to the fractures, and fractures to the wells.
- Pseudosteady state interporosity matrix flow.
- Negligible changes in matrix porosity and matrix pore volume compressibility due to changes in stress.
- Uniform tangential shear stiffness on the fracture planes (tangential compliance is the same in all directions), which implies no relative lateral displacement of the matrix blocks.
- No coupling effects.
- Biot effective stress coefficient equals to the unity.
- Volumetric reservoir (no water encroachment, no water production).

8.3 LIMITATIONS

For the proposed well test analysis technique, seismic or core derived fracture density and fracture aspect ratio data are required, which are not always available. In such cases, data from outcrops or analogue fields could be used as an approximation.

Wellbore storage effects can mask the double porosity signature in the pressure derivative plot, which could lead us to wrong computation of the storage capacity ratio and errors in the estimation of hydrocarbons initially in place in the fracture and matrix systems.

Based upon Nelson's[3] classification (see Table 1.1), this study is best suitable for naturally fractured reservoirs type 2, and 3, where there are well defined dual porosity systems. In the case of type 1 NFRs, where fractures provide all the reservoir storage and permeability, the system reduces to a single porosity system and solutions are the same than for homogeneous reservoirs. This study does not apply for reservoirs type 4, where the fractures do not contribute to porosity or permeability.

9 CONCLUSIONS

1. New equations for computing the change in fracture porosity and fracture permeability due to changes in stress have been presented.

2. Current well test analysis techniques have been improved and extended to consider the elastic behavior of the naturally fractured rock by integrating the normal compliance of the fracture into the pressure transient analysis formulation.

3. Material balance equations that consider the compressibility difference between fractured and matrix systems have been derived for gas, undersaturated, and saturated naturally fractured reservoirs.

4. Well tests analysis has been integrated into the material balance equation to compute original hydrocarbons in place and recovery for gas, undersaturated, and saturated naturally fractured reservoirs.

5. Accurate estimation of the storage capacity ratio at early stages of production is required to obtain good estimation of initial hydrocarbons in place.

6. For naturally fractured gas reservoirs, the assumption of considering matrix compressibility equals to fracture compressibility leads to huge errors (up to 50%) in the estimation of reserves when the fracture pore volume compressibility is 20 times higher than the matrix pore volume compressibility.

7. If the effect of compressibilities is not considered in gas reservoirs, this will lead to overestimates of the original gas in place (in the example it is as large as 60%).

8. In undersaturated naturally fractured reservoirs, huge differences in the estimation of recovery factors are introduced if differences between the fracture pore volume, and matrix pore volume compressibility are not taken into account in the computations.

9. In saturated reservoirs the difference between considering or not considering compressibility effects leads to small errors (less than 5%) in the estimation of original hydrocarbons in place and recovery factors, due to the additional drive contribution of the expansion of the gas cap.

10 RECOMMENDATIONS

This research study can be improved by:

1. Considering transient interporosity fracture flow models.

2. Using fully coupled fracture-matrix models with 3-D stresses.

3. Extending it to naturally fractured reservoirs with water drive (non-volumetric reservoir cases).

11 NOMENCLATURE

The following are the definitions of the nomenclature used in this report.

A = AVO intercept.

B = volumetric factor, rb/STB; AVO gradient.

B_g = gas formation volume factor, rb/SCF.

B_{gi} = initial gas formation volume factor, rb/SCF.

B_{oi} = initial oil formation volume factor, rb/STB.

B_o = oil formation volume factor, rb/STB.

c = compressibility, 1/psi.

C = wellbore storage, bbl/psi.

$(c_t)_f$ = total fracture compressibility, 1/psi.

$(c_t)_m$ = total matrix compressibility, 1/psi.

c_e = effective compressibility, 1/psi.

c_{pp} = isothermal pore volume compressibility due to changes in pore pressure, 1/psi.

c_r = dry bulk rock compressibility, 1/psi.

D = depth, psi.

D_f = fracture density.

$E_{o,f}$ = expansion of the initial amount of oil contained inside the fractures, bbl/STB.

$E_{o,m}$ = expansion of the initial amount of oil contained inside the matrix, bbl/STB.

F = amount of oil produced, RB.

g = acceleration due to gravity, 9.8 m/sec$^{2.}$

G = shear modulus, psi or GPa.

G = initial reservoir gas, SCF.

G_p = cumulative gas production, SCF.

G_f = initial reservoir gas in the fractures, SCF.

G_m = initial reservoir gas in the fractures, SCF.

h = formation thickness, ft.

i = incident polar angle, degrees.

k = average formation permeability, md.

k_f = fracture permeability, md.

k_m = matrix permeability, md.

K = bulk modulus, psi or Gpa.

K_F = bulk modulus of the fluid, psi or GPa.

K_g = bulk modulus of the grains (mineral), psi or Gpa.

K_m = bulk modulus of the matrix (mineral), psi or Gpa.

m = slope from the semilog plot, psia/cycle.

m = ratio of the initial gas cap volume to the initial oil volume.

N = initial reservoir oil, STB.

N_f = initial reservoir oil in the fractures, STB.

N_m = initial reservoir oil in the matrix, STB.

N_p = cumulative produced oil, STB.

n = number of fractures.

p = pressure, psi.

$\overline{p}$ = average reservoir pressure, psi.

p_c = confining pressure, psi.

p_e = effective stress, psi.

p_D = dimensionless pressure.

p_i = initial pressure, psi.

p_{wf} = wellbore flowing pressure, psi.

q = flow rate, BPD.

R = Resistivity, ohm-m.

R_p = acoustic reflection coefficient.

R_{soi} = initial solution gas-oil ratio, SCF/STB.

R_p = cumulative produced gas-oil ratio, SCF/STB.

R_{so} = solution gas-oil ratio, SCF/STB.

r_w = wellbore radius, ft.

r = radius, ft.

r_D = dimensionless radius.

s = skin factor.

S = saturation, fraction.

t = test time, hr.

t_p = producing time before shut-in in a buildup test, hr.

t_i = time intercept, hr.

t_{min} = time at minimum point, hr.

t_D = dimensionless time.

$t*p'$ = pressure derivative.

t_D*p_D' = dimensionless pressure derivative.

V_f = fissures pore volume, bbl.

V_m = volume of matrix fine pores, bbl.

V_p = compressional wave velocity, km/sec; or pore volume, cm^3.

V_s = shear wave velocity, km/sec.

V_t = total fluid volume, bbl.

W = initial reservoir water, bbl.

W_p = cumulative produced water, STB.

B_w = water formation volume factor, bbl/STB.

W_e = water influx into reservoir, bbl.

x_m = characteristic side length, ft.

Z = acoustic impedance, $g/(cm^2 sec)$; or gas deviation factor, dimensionless.

Z_{Nf} = normal compliance of the fracture, Gpa^{-1} or psi^{-1}.

Greek Symbols

α = angle, degrees; or compressional wave velocity, km/sec; or aspect ratio, dimensionless; or Biot effective stress coefficient, dimensionless.

β = shear wave velocity, km/sec.

Δ = change, drop.

$\varepsilon =$ Thomsen anisotropy coefficient.

$\gamma =$ shear wave splitting parameter.

$\lambda =$ interporosity flow parameter, dimensionless.

$\mu =$ viscosity, cp.

$\nu =$ porosity partitioning coefficient, dimensionless; or Poisson ratio, dimensionless.

$\omega =$ storage capacity ratio, dimensionless.

$\phi =$ porosity, dimensionless.

$\rho =$ density, gm/cm^3 or lbm/gal.

$\theta =$ angle, degrees.

Subscripts

$Ani =$ anisotropic.

$c =$ confining.

$D =$ dimensionless.

$d =$ dry.

$F =$ fluid.

$f =$ fracture.

$f+m =$ total NFR system (fracture + matrix).

$g =$ gas.

$H =$ horizontal.

$Iso =$ isotropic.

i = intercept, initial, isotropy.

m = matrix.

mf = mud filtrate.

MP = match point.

Neu = neutron.

Nf = normal to the fracture plane.

o = oil.

p = pore space.

pss = pseudosteady state.

r = radial or infinite acting line zone.

Son = sonic.

T, t = total.

V = vertical.

w = wellbore, well, water.

x = peak.

xo = invaded zone.

12 REFERENCES

1. Tiab, D. and Donaldson, E.C.: "*Petrophysics"*, second edition, Gulf Professional Publishing, Burlington, MA (2004) 488.

2. Stearns, D.W. and Friedman, M.: *"Reservoirs in Fractured Rock"*, Am. Assoc. Petrol. Geol. (AAPG) Memoir 16 and Soc. Expl. Geophysics, Special Publ. No. 10 (1972) 82.

3. Nelson, R.A.: "*Fractured Reservoirs: Turning Knowledge into Practice*", *Soc. Petrol Eng. J.* (Apr. 1987) 407.

4. Belharche, M.: "*Identification, Characterization and Stochastic Modeling of Naturally Fractured Reservoir Validated by Simulation Model – Case Study: Zone 14 of Hassi Messaoud Field",* Master Thesis, the University of Oklahoma, Norman, OK (2005).

5. Argawal, B., Hermansen, H. Sylte, J.E., and Thomas, L.K.: "*Reservoir Characterization of Ekofisk Field: A Giant, Fractured Chalk Reservoir in the Norwegian North Sea – History Match", SPEREE* (Dec. 2000) 534.

6. Warren, J.E. and Root, P.J.: *"The Behavior of Naturally Fractured Reservoirs", SPEJ* (Sep. 1963) 245.

7. Kazemi, H.: *"Pressure Transient Analysis of Naturally Fractured Reservoirs with Uniform Fracture Distribution", SPEJ* (Dec. 1969) 451; *Trans.,* AIME, **246**.

8. Reiss, L.H.: "*The Reservoir Engineering Aspects of Fractured Formations"*, Editions Technip, Paris (1980).

9. Abdassh, D. and Ershaghi, I.: *"Triple Porosity Systems for Representing Naturally Fractured Reservoirs", SPEFE* (April 1986) 113.

10. Sondergeld, C.H. and Rai, C.S.: *"Laboratory Observations of Shear-Wave Propagation in Anisotropic Media", The Leading Edge* (Feb. 1992) 38.

11. Lynn, H.B., Simon, K.M., Layman, M., Schneider, R., Bates, C.R. and Jones, M.: *"Use of Anisotropy in P-wave and S-wave data for Fracture Characterization in a Naturally Fractured Gas Reservoir", The Leading Edge* (Aug. 1995) 887.

12. Thomsen, L.: *"Reflection Seismology over Azimuthally Anisotropic Media", Geophysics* (March 1988) **53**, 304.

13. Rüger, A. and Tsvankin, I.: *"Using AVO for Fracture Detection: Analytic Basis and Practical Solutions", The Leading Edge* (Oct. 1997) 1429.

14. Dyke, C.G., Wu, B. and Tayler, M.D.: "*Advances in Characterizing Natural Fracture Permeability from Mud Log Data*", paper SPE 25022 presented at the 1992 European Petroleum Conference, Cannes, France, Nov.16-18.

15. Slatt, R.: "*GEOL 6970: Introduction to Reservoir Characterization - Class Notes*", graduate course taught at the University of Oklahoma, Norman, OK (Fall 2003).

16. Locke, L.C. and Bliss, J.E.: *"Core Analysis Technique for Limestone and Dolomite", World Oil* (Sept. 1950).

17. Terzaghi, K.: *"The Shearing Resistance of Saturated Soils and the Angle Between the Planes of Shear", Proceedings of the International Conference on Soil Mechanics and Foundation Engineering*, Harvard University Press, Cambridge, MA (1936) **1**, 54.

18. Biot, M.A.: *"General Theory of Three-Dimensional Consolidation", Journal of Applied Physics* (1941) **12**, 155-164.

19. Sondergeld, C.H. and Rai, C.S.: "*Concepts of Elasticity*", class lecture handout of the graduate course "*PE 5990-960: Seismic Rock Properties",* the University of Oklahoma, Norman, OK (Sept. 2003).

20. Saidi, A. M.: "*Reservoir Engineering of Fractured Reservoirs"*, Total Edition Press, Paris (1987).

21. Horner, D.R.: *"Pressure Buildup in Wells", Proceedings*, Third World Petroleum Congress, The Hague (1951)**2**, 203-523. Also, *Reprint Series, No. 9 – Pressure Analysis Methods*, Society of Petroleum Engineers of AIME, Dallas, TX (1967) 25-43.

22. Bourdet, D., Ayoub, J.A., Whittle, T.M., Pirard, Y.M. and Kniazeff, V.: *"Interpreting Well Tests in Fractured Reservoirs", World Oil* (Oct. 1983) 77.

23. Tiab, D., Restrepo, D. P. and Igbokoyi, A.: "*Fracture Porosity of Naturally Fractured Reservoirs",* paper SPE 104056 presented at the 2006 First International Oil Conference and Exhibition in Mexico, Cancun, Mexico, August 31 – September 2.

24. Stewart, G., Asharsobbi, F. and Heriot-Watt U..: *"Well Test Interpretation for Naturally Fractured Reservoirs*", paper SPE 18173 presented at the 1988 SPE Annual Technical Conference and Exhibition, Houston, TX, October 2-5.

25. Lee, J., Rollins, J.B. and Spivey, J.P.: "*Pressure Transient Testing: SPE Textbook Series"*, SPE, Richardson, TX (2003) **9**,137.

26. Tiab, D.: *"Analysis of Pressure and Pressure Derivative without Type Curve Matching – Skin and Wellbore Storage", Journal of Petroleum Science and Engineering* (1995) **12**, 171.

27. Engler, T. and Tiab, D.: *"Analysis of Pressure and Pressure Derivative without Type Curve Matching, 4. Naturally Fractured Reservoirs", Journal of Petroleum Science and Engineering* (1996) **15**, 127.

28. Cardona, R., Ozkan, E. and Batzle, M.: *"Pressure Transient Experiments and the Elastic Characterization of Fractures",* paper presented at the 2002 SEG International Exposition and 72nd Annual Meeting, Salt Lake City, UT, October 6-11.

29. Zimmerman, R.W.: "*Compressibility of Sandstones"*, Elsevier, Amsterdam, The Netherlands (1991).

30. Schoenberg, M. and Douma, J.: *"Elastic Wave Propagation in Media with Parallel Fractures and Aligned Cracks", Geophys. Prosp.* (1989) **36**, 571.

31. Schoenberg, M. and Sayers, C.: *"Seismic Anisotropy of Fractured Rock", Geophysics* (Jan. 1995) **60**, 204.

32. Bakulin, A., Grechka, V. and Tsvankin, I.: *"Estimation of Fracture Parameters from Reflection Seismic Data – Part I and II", Geophysics* (Nov. 2000) **65**, 1788.

33. Brown, R.L.: *"Stress-Dependent Fracture Compliance"*, paper SEG ANI 2.4 presented at the 2005 SEG International Exposition and Seventy-Fifth Annual Meeting, Houston, TX, November 6-11.

34. Sheriff, R.E.: "*Encyclopedic Dictionary of Applied Geophysics"*, Society of Exploration Geophysicist, (2002) **13**, 115.

35. Schilthuis, R.J.: *"Active Oil and Reservoir Energy", Trans. AIME* (1936) **118**, 33.

36. Aguilera, R.: *"Effect of Fracture Compressibility on Gas-in-Place Calculations of Stress-Sensitivity Naturally Fractured Reservoirs"*, paper SPE 100451 presented at the 2006 Gas Technology Symposium, Calgary, May 15-17.

37. Penuela, G., Idrobo, E.A., Ordonez, A, Medina, C.E. and Meza, N.: *"A New Material Balance Equation for Naturally Fractured Reservoirs Using a Dual System Approach"*, paper SPE 68831 presented at the 2001 Western Regional Meeting, Bakersfield, CA, March 26-30.

38. Craft, B.C. and Hawkins, M.: "*Applied Petroleum Reservoir Engineering"*, second Edition, Prentice-Hall Inc., Englewood Cliffs, NJ (1991) 172.

APPENDIX A: RELATIONSHIPS AMONG ELASTIC PROPERTIES

Table A.0.1. Elastic constants for isotropic media expressed in terms of each other and P-and S-wave velocities ($\alpha=V_p$ and $\beta=V_s$) and density ρ. (Sheriff, R.E.[34])

	Young's modulus, E	Poisson's ratio, σ	Bulk modulus, k	Shear modulus, μ	Lamé constant, λ	P-wave velocity, α	S-wave velocity, β	Velocity ratio, β/α
(E, σ)			$\frac{E}{3(1-2\sigma)}$	$\frac{E}{2(1+\sigma)}$	$\frac{E\sigma}{(1+\sigma)(1-2\sigma)}$	$\left[\frac{E(1-\sigma)}{(1+\sigma)(1-2\sigma)\rho}\right]^{1/2}$	$\left[\frac{E}{2(1+\sigma)\rho}\right]^{1/2}$	$\left[\frac{(1-2\sigma}{2(1-\sigma)}\right]^{1/2}$
(E, k)		$\frac{3k-E}{6k}$		$\frac{3kE}{9k-E}$	$3k\left(\frac{3k-E}{9k-E}\right)$	$\left[\frac{3k(3k+E)}{\rho(9k-E)}\right]^{1/2}$	$\left[\frac{3kE}{(9k-E)\rho}\right]^{1/2}$	$\left(\frac{E}{3k+E}\right)^{1/2}$
(E, μ)		$\frac{E-2\mu}{2\mu}$	$\frac{\mu E}{3(3\mu-E)}$		$\mu\left(\frac{E-2\mu}{3\mu-E}\right)$	$\left[\frac{\mu(4\mu-E)}{(3\mu-E)\rho}\right]^{1/2}$	$\left(\frac{\mu}{\rho}\right)^{1/2}$	$\left(\frac{3\mu-E}{4\mu-E}\right)^{1/2}$
(σ, k)	$3k(1-2\sigma)$			$\frac{3k}{2}\left(\frac{1-2\sigma}{1+\sigma}\right)$	$3k\left(\frac{\sigma}{1+\sigma}\right)$	$\left[\frac{3k(1-\sigma)}{\rho(1+\sigma)}\right]^{1/2}$	$\left[\frac{3k}{2\rho}\left(\frac{1-2\sigma}{1+\sigma}\right)\right]^{1/2}$	$\left[\frac{1-2\sigma}{2(1-\sigma)}\right]^{1/2}$
(σ, μ)	$2\mu(1+\sigma)$		$\frac{2\mu(1+\sigma)}{3(1-2\sigma)}$		$\mu\left(\frac{2\sigma}{1-2\sigma}\right)$	$\left[\left(\frac{2\mu}{\rho}\right)\left(\frac{1-\sigma}{1-2\sigma}\right)\right]^{1/2}$	$\left(\frac{\mu}{\rho}\right)^{1/2}$	$\left[\frac{1-2\sigma}{2(1-\sigma)}\right]^{1/2}$
(σ, λ)	$\lambda\frac{(1+\sigma)(1-2\sigma)}{\sigma}$		$\lambda\left(\frac{1+\sigma}{3\sigma}\right)$	$\lambda\left(\frac{1-2\sigma}{2\sigma}\right)$		$\left[\left(\frac{\lambda}{\rho\sigma}\right)(1-\sigma)\right]^{1/2}$	$\left[\frac{\lambda}{\rho}\left(\frac{1-2\sigma}{2\sigma}\right)\right]^{1/2}$	$\left[\frac{1-2\sigma}{2(1-\sigma)}\right]^{1/2}$
(k, μ)	$\frac{9k\mu}{3k+\mu}$	$\frac{3k-2\mu}{2(3k+\mu)}$			$k-2\mu/3$	$\left(\frac{k+4\mu/3}{\rho}\right)^{1/2}$	$\left(\frac{\mu}{\rho}\right)^{1/2}$	$\left(\frac{\mu}{k+4\mu/3}\right)^{1/2}$
(k, λ)	$9k\left(\frac{k-\lambda}{3k-\lambda}\right)$	$\frac{\lambda}{3k-\lambda}$		$\frac{3}{2}(k-\lambda)$		$\left(\frac{3k-2\lambda}{\rho}\right)^{1/2}$	$\left[\frac{3(k-\lambda)}{2\rho}\right]^{1/2}$	$\left[\frac{1}{2}\left(\frac{k-\lambda}{k-2\lambda/3}\right)\right]^{1/2}$
(μ, λ)	$\mu\left(\frac{3\lambda+2\mu}{\lambda+\mu}\right)$	$\frac{\lambda}{2(\lambda+\mu)}$	$\lambda+\frac{2}{3}\mu$			$\left(\frac{\lambda+2\mu}{\rho}\right)^{1/2}$	$\left(\frac{\mu}{\rho}\right)^{1/2}$	$\left(\frac{\mu}{\lambda+2\mu}\right)^{1/2}$
(α, β)	$\rho\beta^2\left(\frac{3\alpha^2-4\beta^2}{\alpha^2-\beta^2}\right)$	$\frac{\alpha^2-2\beta^2}{2(\alpha^2-\beta^2)}$	$\rho\left(\alpha^2-\frac{4}{3}\beta^2\right)$	$\rho\beta^2$	$\rho(\alpha^2-2\beta^2)$			

APPENDIX B: RELATIONSHIPS AMONG FRACTURE PARAMETERS

Table B.0.1. Relationships among fracture parameters in terms of fracture geometry. (After Reiss.[8])

Fracture structure	**Fracture network**	**General expression**				**Practical units***			
		f_s	ϕ_f	$k_f(\phi_f, a)$	$k_f(\phi_f, b)$	f_s **(cm^{-1})**	ϕ_f **(%)**	$k_f(\phi_f, a)$ **(Darcy)**	$k_f(\phi_f, b)$ **(Darcy)**
Sheets	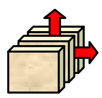	$\frac{1}{a}$	$\frac{b}{a}$	$\frac{a^2\phi_f^3}{12}$	$\frac{b^2\phi_f}{12}$	$\frac{1}{a}$	$\frac{b}{100a}$	$8.33a^2\phi_f^3$	$\frac{8.33b^2\phi_f}{10^4}$
Match-sticks	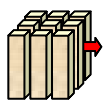	$\frac{1}{a}$	$\frac{2b}{a}$	$\frac{a^2\phi_f^3}{96}$	$\frac{b^2\phi_f}{24}$	$\frac{1}{a}$	$\frac{b}{50a}$	$1.04a^2\phi_f^3$	$\frac{4.16b^2\phi_f}{10^4}$
	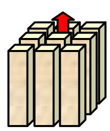	$\frac{2}{a}$	$\frac{2b}{a}$	$\frac{a^2\phi_f^3}{48}$	$\frac{b^2\phi_f}{12}$	$\frac{2}{a}$	$\frac{b}{50a}$	$2.08a^2\phi_f^3$	$\frac{8.33b^2\phi_f}{10^4}$
Cubes with one fracture plane impermeable	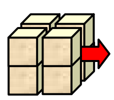	$\frac{1}{a}$	$\frac{2b}{a}$	$\frac{a^2\phi_f^3}{96}$	$\frac{b^2\phi_f}{24}$	$\frac{1}{a}$	$\frac{b}{50a}$	$1.04a^2\phi_f^3$	$\frac{4.16b^2\phi_f}{10^4}$
	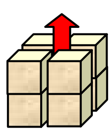	$\frac{2}{a}$	$\frac{2b}{a}$	$\frac{a^2\phi_f^3}{48}$	$\frac{b^2\phi_f}{12}$	$\frac{2}{a}$	$\frac{b}{50a}$	$2.08a^2\phi_f^3$	$\frac{8.33b^2\phi_f}{10^4}$
Cubes	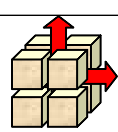	$\frac{2}{a}$	$\frac{3b}{a}$	$\frac{a^2\phi_f^3}{162}$	$\frac{b^2\phi_f}{18}$	$\frac{2}{a}$	$\frac{3b}{100a}$	$0.62a^2\phi_f^3$	$\frac{5.55b^2\phi_f}{10^4}$

* a in cm, b in microns (1µm=10^{-4} cm), ϕ_f in percent, k_f in darcies.

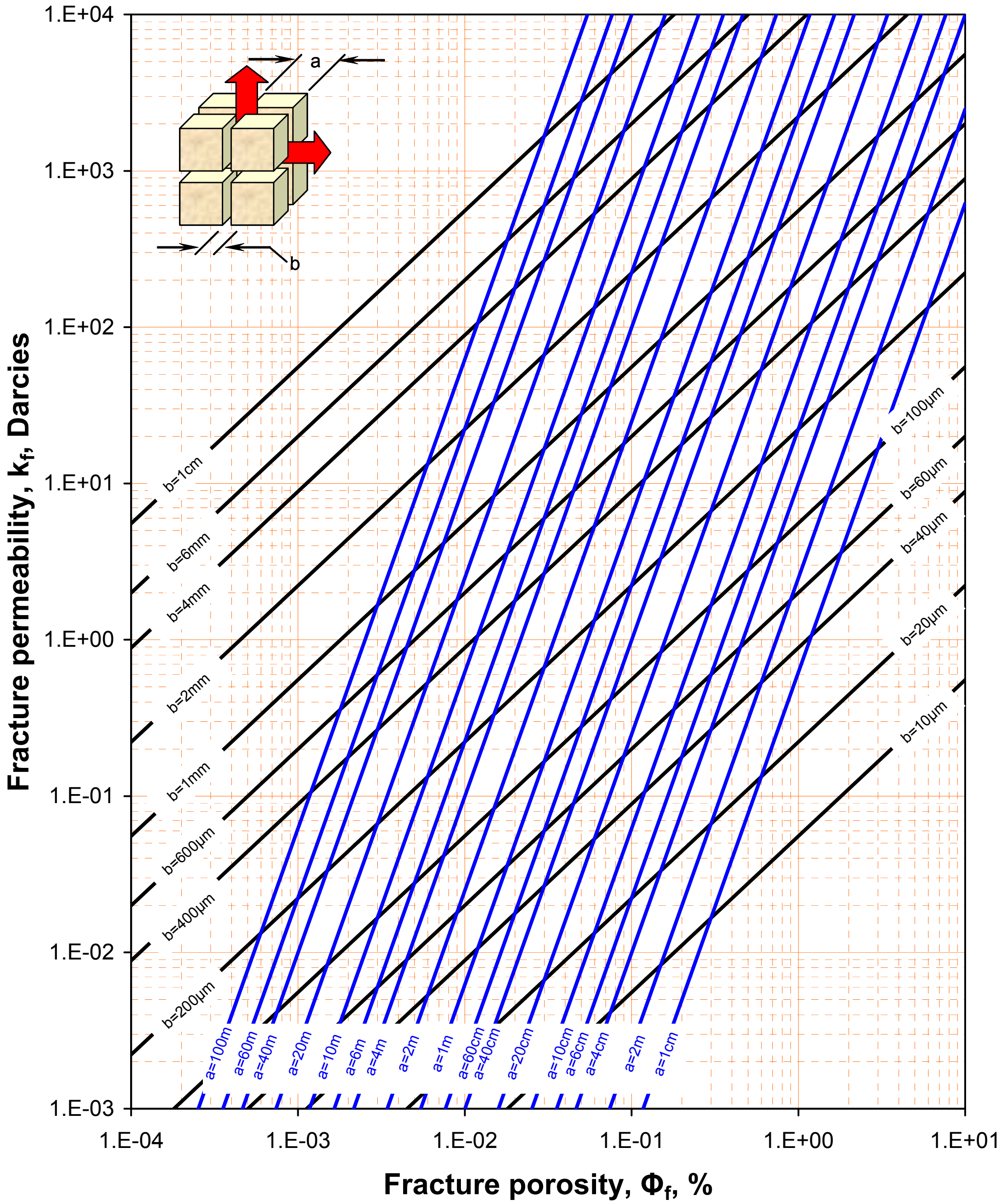

Figure B.0.1. Relationships among fracture permeability k_f, fracture porosity ϕ_f, fracture width b, and matrix size a for the sugar cube model. (After Reiss[8])

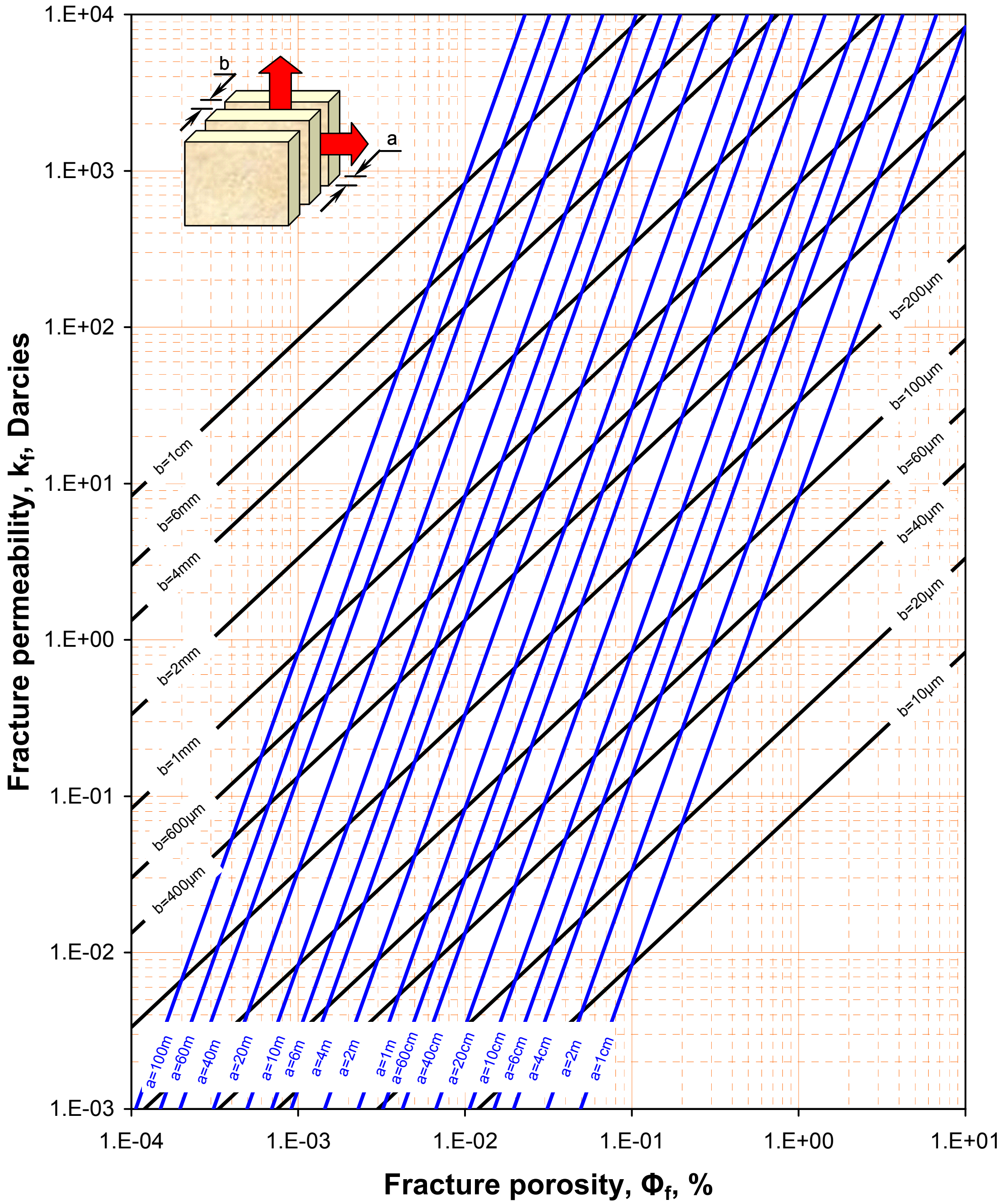

Figure B.0.2. Relationships among fracture permeability k_f, fracture porosity ϕ_f, fracture width b, and matrix size a for the sheets model. (After Reiss[8])

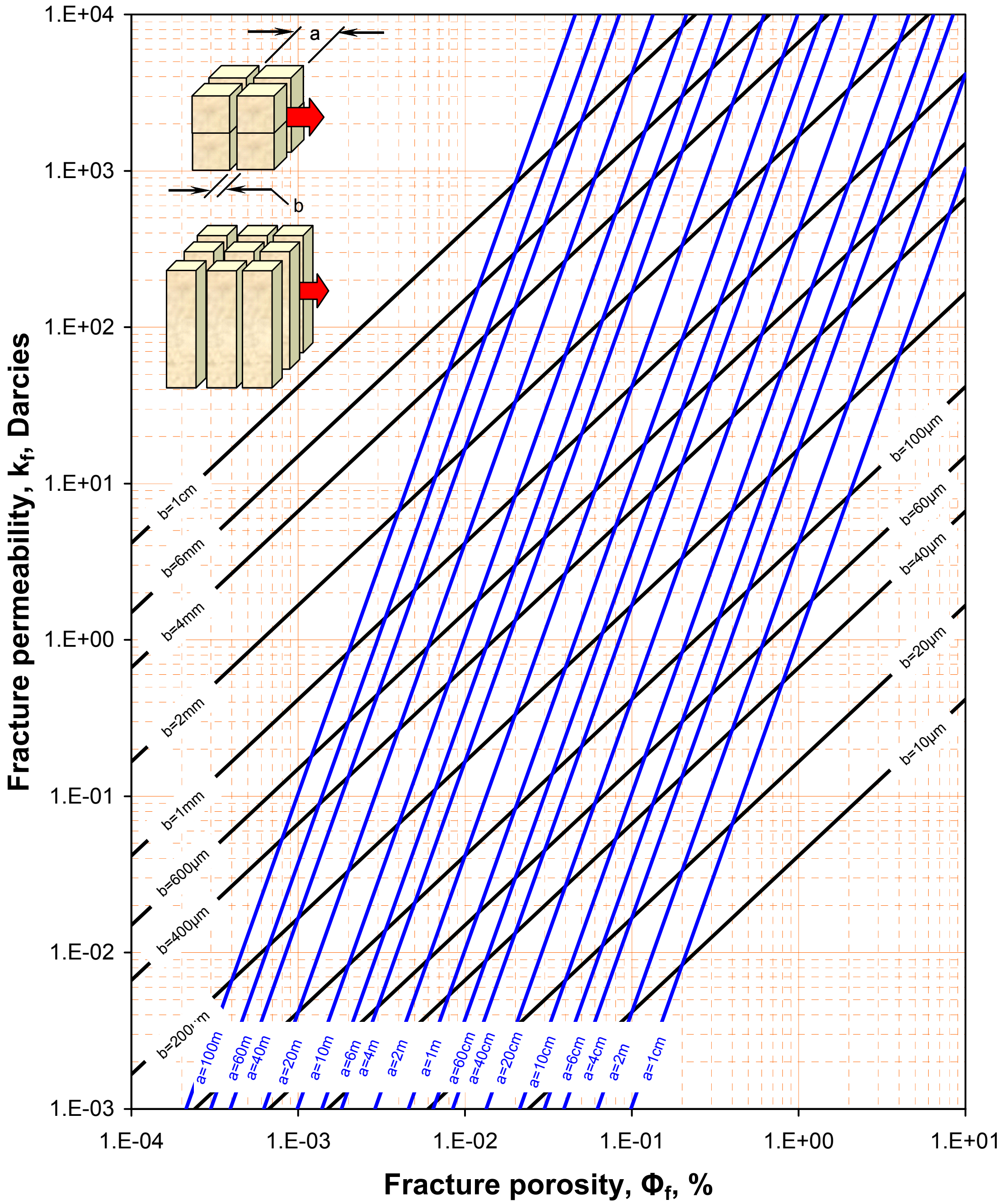

Figure B.0.3. Relationships among fracture permeability k_f, fracture porosity ϕ_f, fracture width b, and matrix size a for matches model with flow perpendicular to the matches axes.
(After Reiss[8])

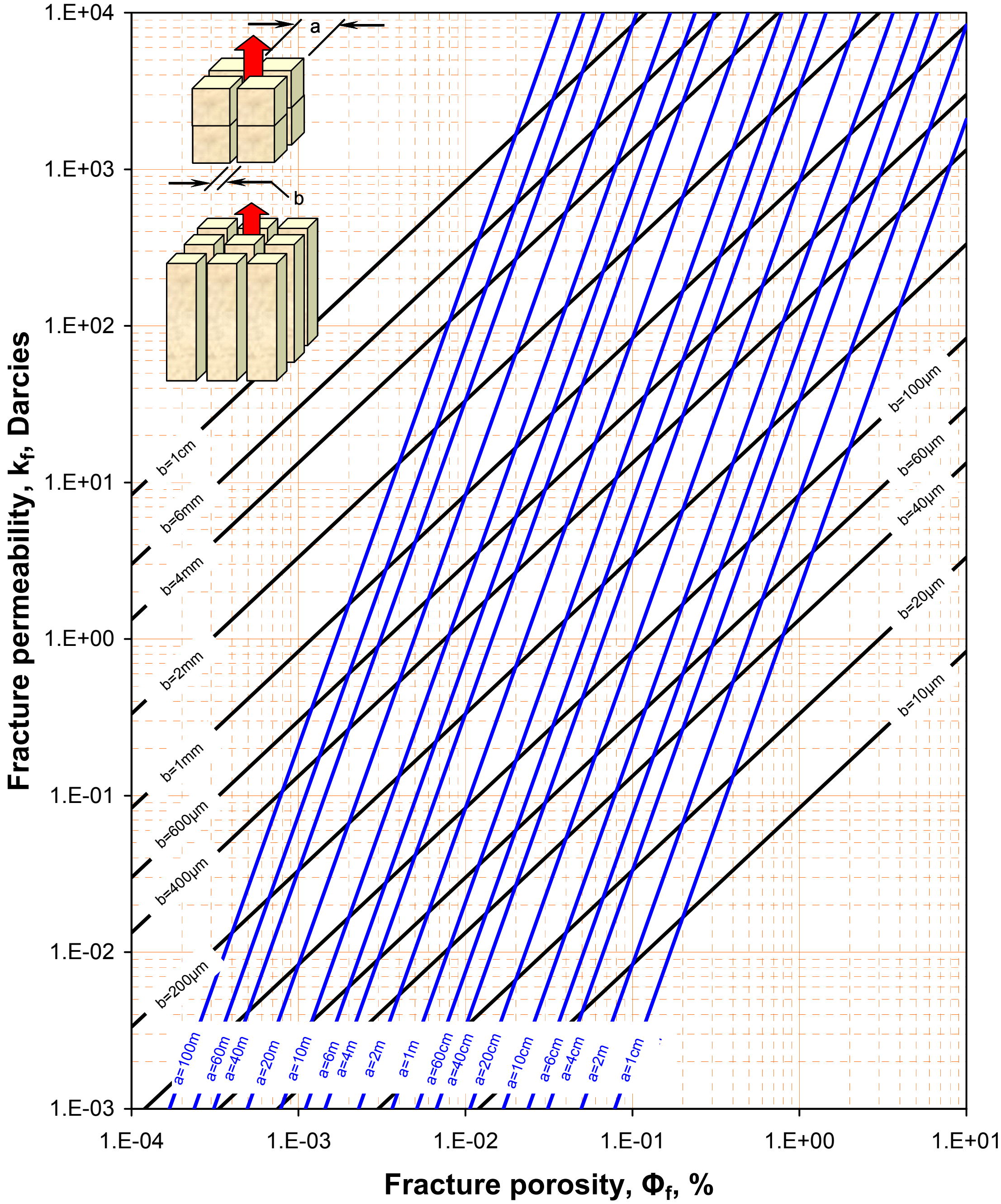

Figure B.0.4. Relationships among fracture permeability k_f, fracture porosity ϕ_f, fracture width b, and matrix size a for matches model with flow parallel to the matches axes.
(After Reiss[8])

APPENDIX C: PRESSURE DATA FOR THE EXAMPLE OF CHAPTER SIX

Table C.0.1. Pressure data for the example of chapter six.

***t*, hr**	***p_{ws}*, psia**	***Δp*, psi**	***t*Δp'*, psi**	**$(\Delta t+t_p)/\Delta t$**	***t*, hr**	***p_{ws}*, psia**	***Δp*, psi**	***t*Δp'*, psi**	**$(\Delta t+t_p)/\Delta t$**
0.00	3055.00	--	--	--	38.45	3603.24	548.24	163.89	1.418
0.05	3065.50	10.50	13.04	322.600	48.51	3643.76	588.76	168.90	1.331
0.10	3078.35	23.35	16.08	161.800	57.75	3669.80	614.80	164.39	1.278
0.17	3084.33	29.33	24.61	95.588	63.63	3690.12	635.12	160.28	1.253
0.24	3097.28	42.28	34.96	68.000	74.30	3712.38	657.38	155.14	1.216
0.28	3100.82	45.82	37.04	58.429	91.95	3745.91	690.91	131.30	1.175
0.37	3112.95	57.95	41.46	44.459	116.02	3772.86	717.86	106.94	1.139
0.44	3117.58	62.58	43.59	37.545	140.82	3789.41	734.41	83.69	1.114
0.51	3126.52	71.52	47.79	32.529	164.43	3803.26	748.26	70.26	1.098
0.60	3133.65	78.65	55.66	27.800	195.76	3811.46	756.46	58.22	1.082
0.70	3143.25	88.25	58.62	23.971	211.54	3817.57	762.57	49.94	1.076
0.80	3150.70	95.70	64.93	21.100	242.27	3821.44	766.44	42.82	1.066
0.90	3159.25	104.25	64.88	18.867	261.79	3826.59	771.59	41.18	1.061
0.91	3159.81	104.81	65.27	18.670	305.68	3830.48	775.48	33.16	1.053
1.07	3171.54	116.54	71.46	16.028	350.09	3835.49	780.49	29.26	1.046
1.20	3177.94	122.94	70.57	14.400	424.94	3840.10	785.10	27.61	1.038
1.37	3189.85	134.85	73.98	12.737	486.67	3844.51	789.51	27.90	1.033
1.60	3199.68	144.68	78.14	11.050	568.28	3847.76	792.76	29.77	1.028
1.95	3216.82	161.82	83.74	9.246	650.83	3852.62	797.62	32.61	1.025
2.32	3229.66	174.66	86.83	7.931	759.95	3857.16	802.16	42.15	1.021
2.70	3246.24	191.24	88.13	6.956	805.44	3860.72	805.72	46.91	1.020
3.55	3268.59	213.59	98.34	5.530	870.35	3863.25	808.25	51.64	1.018
4.39	3293.90	238.90	111.23	4.663	1056.44	3874.73	819.73	66.20	1.015
5.33	3313.28	258.28	118.58	4.017	1077.11	3876.92	821.92	67.03	1.015
6.47	3340.48	285.48	127.91	3.485	1209.90	3885.52	830.52	84.87	1.013
8.16	3366.75	311.75	136.64	2.971	1468.59	3901.24	846.24	96.07	1.011
9.16	3388.03	333.03	140.42	2.755	1681.93	3920.08	865.08	112.29	1.010
10.29	3400.95	345.95	142.17	2.563	2081.49	3940.27	885.27	131.76	1.008
11.79	3424.49	369.49	147.79	2.364	2526.53	3975.18	920.18	136.98	1.006
13.77	3442.24	387.24	144.90	2.168	3066.74	3997.31	942.31	144.80	1.005
15.77	3466.62	411.62	148.12	2.020	4101.13	4041.08	986.08	137.44	1.004
18.41	3485.24	430.24	153.02	1.873	5484.42	4077.17	1022.17	138.62	1.003
21.50	3513.63	458.63	150.95	1.748	6529.31	4106.21	1051.21	148.12	1.002
25.59	3537.12	482.12	160.82	1.628	8080.42	4135.37	1080.37	162.34	1.002
31.67	3574.65	519.65	159.44	1.508					

APPENDIX D: DEFINITIONS AND RELATIONSHIPS BETWEEN COMPRESSIBILITIES

Zimmerman's[29] notation has been adopted and complemented to take into account the fracture system. The first subscript indicates the relevant volume change (pore volume V_p or bulk volume V_b), the second subscript indicates the pressure which is varied (pore pressure, P_p, or confining pressure, P_c), the third subscript (after a comma) indicates the frame taken into account (matrix, *m*, fracture, *f*, or the total fracture system, (*f*+*m*)). For each system, the compressibility is defined as:

Table D.0.1. Definitions of compressibilities.

Matrix	Fracture	Total system, fracture + matrix
$c_{bc,m} = -\frac{1}{V_{b,m}}\left(\frac{dV_{b,m}}{dP_c}\right)_{P_p}$	$c_{bc,f} = -\frac{1}{V_{b,f}}\left(\frac{dV_{b,f}}{dP_c}\right)_{P_p}$	$c_{bc,(f+m)} = -\frac{1}{V_{b,(f+m)}}\left(\frac{dV_{b,(f+m)}}{dP_c}\right)_{P_p}$
$c_{bp,m} = \frac{1}{V_{b,m}}\left(\frac{dV_{b,m}}{dP_p}\right)_{P_c}$	$c_{bp,f} = \frac{1}{V_{b,f}}\left(\frac{dV_{b,f}}{dP_p}\right)_{P_c}$	$c_{bp,(f+m)} = \frac{1}{V_{b,(f+m)}}\left(\frac{dV_{b,(f+m)}}{dP_p}\right)_{P_c}$
$c_{pc,m} = -\frac{1}{\phi_m}\left(\frac{d\phi_m}{dP_c}\right)_{P_p}$	$c_{pc,f} = -\frac{1}{\phi_f}\left(\frac{d\phi_f}{dP_c}\right)_{P_p}$	$c_{pc,(f+m)} = -\frac{1}{\phi_T}\left(\frac{d\phi_T}{dP_c}\right)_{P_p}$
$c_{pp,m} = \frac{1}{\phi_m}\left(\frac{d\phi_m}{dP_p}\right)_{P_c}$	$c_{pp,f} = \frac{1}{\phi_f}\left(\frac{d\phi_f}{dP_p}\right)_{P_c}$	$c_{pp,(f+m)} = \frac{1}{\phi_T}\left(\frac{d\phi_T}{dP_p}\right)_{P_c}$

The total compressibility is defined as:

$$c_{t.m} = c_{pp,m} + c_F$$

$$c_{t.f} = c_{pp,f} + c_F$$

Where c_F is the average fluid compressibility, defined as:

$$c_F = c_o S_o + c_g S_g + c_w S_w$$

S_o, S_g, and S_w are the oil, gas, and water saturations expressed as fractions of the total fluid volume at reservoir conditions.

Relationships between compressibilities:

Zimmerman[29] presented the demonstrations to get the following relationships:

$$c_{bp} = c_{bc} - c_r$$

$$c_{pc} = (c_{bc} - c_r)/\phi$$

$$c_{pp} = \left[c_{bc} - (1+\phi)c_r\right]/\phi$$

$$c_{pp} = c_{pc} - c_r$$

Where c_r is the grain compressibility.

APPENDIX E: PRESSURE TRANSIENT ANALYSIS INTERPRETATION FOR THE GAS EXAMPLE OF CHAPTER SEVEN

For this analysis, the program Saphir© was used, and the model that best adjusted the pressure data is a dual porosity, closed system. Table E.0.1 presents the fluid and reservoir parameters that were used as input to the pressure transient analysis.

Table E.0.1. Reservoir parameters used as input in the pressure transient analysis.

Property	Value	Property	Value
Test date / time		Formation gas volume factor, B_g	0.00258585 cf/scf
Formation interval	XX	Gas compressibility, c_{gas}	4.57E-5 psi^{-1}
Perforated interval	YY	Gas density, ρ_g	0.26 g/cc
Gauge type / #	Quartz		
Gauge depth	86' above top of the pay zone	Total compressibility, c_t	4.67E-5 psi^{-1}
		Connate water saturation, S_{wc}	0 %
TEST TYPE	Standard		
		Selected model	
Porosity, ϕ	32 %	Model option	Standard model
Well radius, r_w	0.51 ft	Well	Vertical, variable skin
Pay zone, h	71 ft	Reservoir	Two porosity PSS
		Boundary	Rectangle, no flow
Water salinity	10000 ppm		
Formation compressibility, $c_{pp,(f+m)}$	1E-6 psi^{-1}	**Main model parameters**	
Reservoir temperature	178 °F	T_{Match}	57000 1/hr
Initial reservoir pressure, P_i	9472 psia	P_{Match}	9.06E-7 1/[psi^2/cp]
		Wellbore storage coefficient, C	0.00969 bbl/psi
FLUID TYPE	Gas	Total skin, s	31.5
		$k.h$, total	66900 md.ft
Gas specific gravity	0.56	average permeability, k	942 md
Pseudocritical pressure	673.405 psia	Initial reservoir pressure, P_i	9472 psia
Pseudocritical temperature	339.11 °R		

Property	Value	Property	Value
		Model parameters	
Sour gas composition		**Well and wellbore parameters (tested well)**	
Hydrogen sulphide	0	Wellbore storage coefficient, C	0.00969 bbl/psi
Carbon dioxide	9.999E-4	Mechanical skin, $s_m = s_{q=0}$	3.02
Nitrogen	0	Rate dependent skin gradient, ds/dq	3.5E-4 $[\text{Mscf/D}]^{-1}$
		Reservoir and boundary parameters	
Hydrocabon fraction(s)		Initial pressure, P_i	9472 psia
Methane	0.995995	$k.h$	66900 md.ft
Ethane	0.0020002	Average permeability, k	942 md
Propane	4.005E-4	Storage capacity ratio, ω	0.01
Iso-butane	3.007E-4	Interporosity flow parameter, λ	1.03E^{-7}
Iso-pentane	1.029E-4	S - No flow	318 ft
N-heptane	2.008E-4	E - No flow	1630 ft
		N - No flow	967 ft
Temperature	178 °F	W - No flow	15700 ft
Pressure	9472 psia		
		Derived and secondary parameters	
Properties @ reservoir conditions		Delta P (total skin)	89.08 psi
		Delta P ratio (total skin)	0.61 fraction
Gas		Average reservoir pressure	9421 psia
Gas deviation factor, Z	1.35842		
Gas viscosity, μ_g	0.0357591 cp		

Figure E.0.1 presents the pressure and production data history plot for this well, in which the shadowed areas correspond to the pressure buildup periods used in the analysis. Rate, pressure, superposition time, pseudopressure, and pseudopressure derivative data are tabulated in tables E.0.2 through E.0.11.

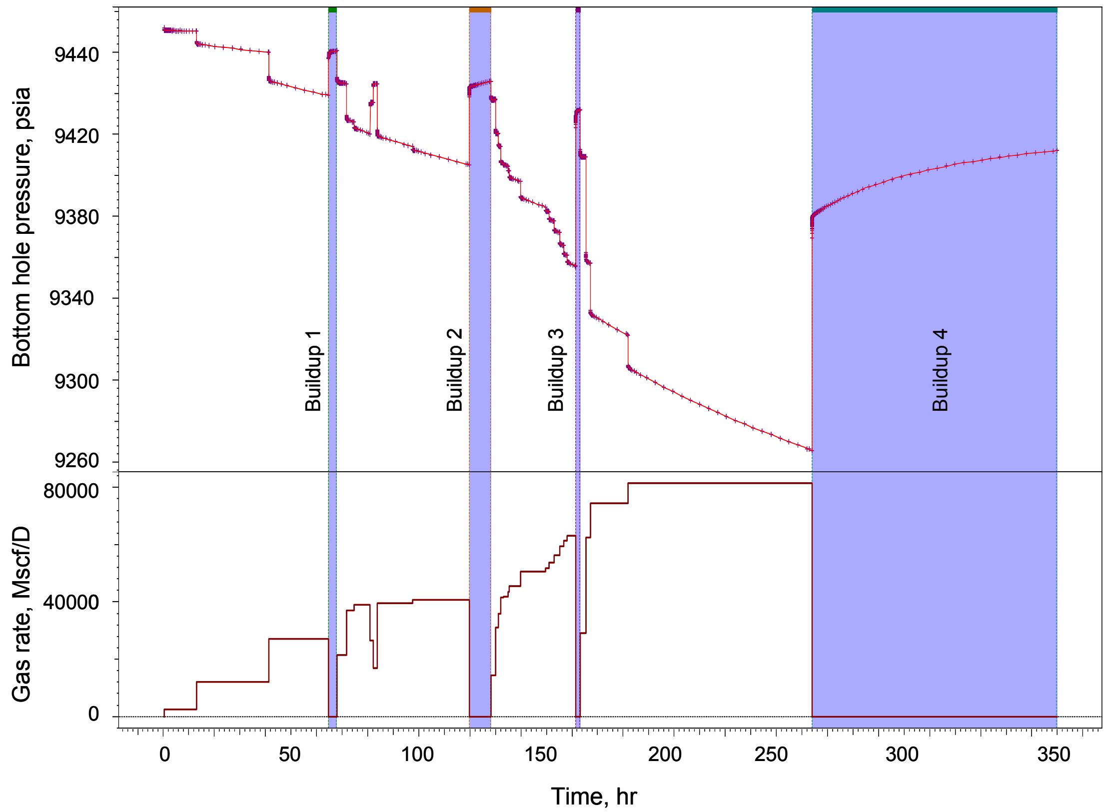

Figure E.0.1. *History pressure and production data plot.*

As shown in the semilog plot of Figure E.0.2, the analytical model is matching all the pressure buildups analyzed. Notice that the curves do not overlay each other, which indicates that the total skin is affected by the non-Darcy effect. From the model results, presented in Table 7.3, it is observed that mechanical skin is 3.02 and the rate dependant skin gradient is 3.54×10^{-4} $(\mathrm{Mscf/D})^{-1}$. Since all the curves are parallel each other, it indicates that no noticeable changes in average permeability have occurred during the first 350 hours of production.

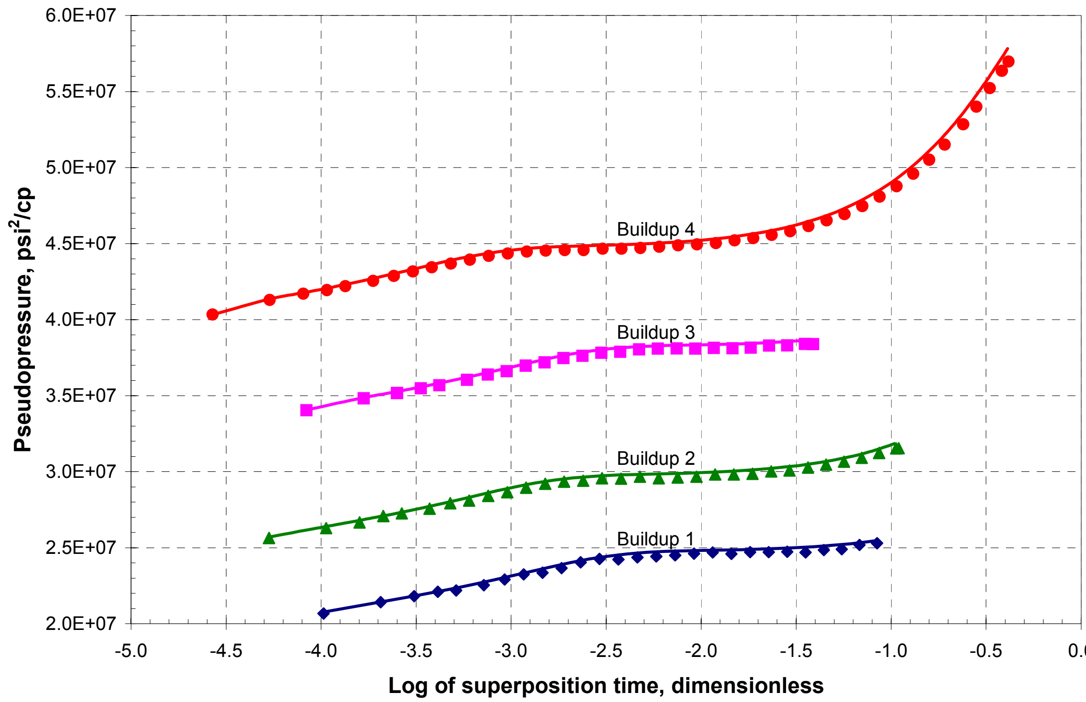

Figure E.0.2. Semilog analysis.

As shown in the pseudopressure derivative plot of Figure E.0.3, even though the data is noisy during the double porosity region (troughs in the pseudopressure derivative data), the analytical model presents a good match with the field data for all the buildups analyzed. Notice also that the first three pressure buildups are too short to reach radial or boundary effects, and that the pseudopressure curves do not overlay each other, which indicates that total skin is affected by the non-Darcy effect.

The late radial flow period is masked completely by the boundary effects. Furthermore, notice from figures 7.3 and E.0.3 that the dimensionless pressure derivative value of $\frac{t_D}{C_D}\ p_D' = \frac{1}{2}$ (dashed horizontal line in the plots) shows that the late radial flow period does not match the early radial portion of the derivative curves, indicating that the matrix blocks are not uniformly distributed, which makes it not possible for this case to use the *Tiab's Direct Synthesis Technique* as it is developed currently (for additional information see paper SPE 104056, reference 23, and for the definition of dimensionless pressure and dimensionless pressure derivative see Appendix F).

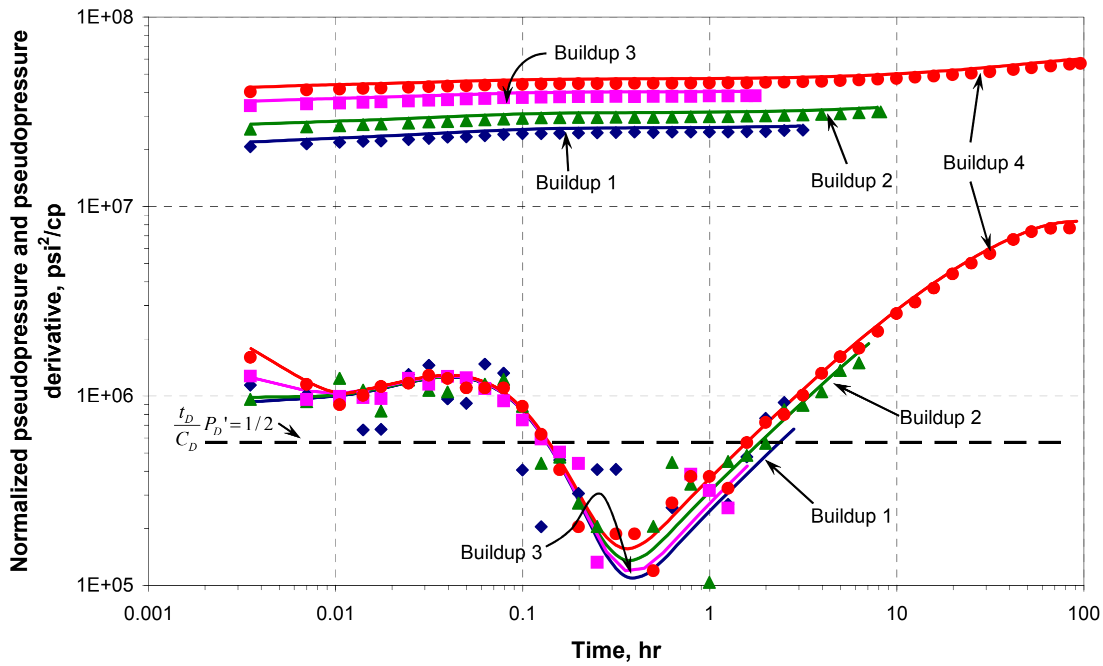

Figure E.0.3. Pseudopressure derivative overlays for the selected pressure buildups.

Table E.0.2. Gas rate data for Example 7.1.1.

Flow period number	***Duration, hr***	***Gas rate, Mscf/d***		***Flow period number***	***Duration, hr***	***Gas rate, Mscf/d***
1	12.75	2410		17	1.75	41925
2	28.25	12060		18	0.50	43442
3	23.50	27225		19	4.25	45578
4 (buildup 1)	3.25	0		20	10.00	50556
5	3.75	21565		21	1.25	51621
6	3.00	36892		22	2.00	53724
7	6.25	39067		23	2.25	56313
8	1.25	26538		24	1.50	59382
9	1.50	16972		25	1.25	61504
10	13.75	39633		26	3.50	63202
11	22.25	40720		27 (buildup 3)	1.75	0
12 (buildup 2)	8.50	0		28	2.25	28974
13	1.75	14415		29	1.75	62384
14	1.25	30950		30	14.75	74456
15	0.75	35753		31	72.00	81408
16	1.25	41506		32 (buildup 4)	96.00	0

Table E.0.3. Field pressure data for Example 7.1.1.

t, hr	***p_{ws}, psia***	***t, hr***	***p_{ws}, psia***	***t, hr***	***p_{ws}, psia***	***t, hr***	***p_{ws}, psia***
0.253889	9472.02	13.00389	9470.40	41.35882	9446.42	65.25277	9460.22
0.257386	9471.12	13.00739	9465.46	41.40790	9446.20	65.38195	9460.32
0.260884	9471.08	13.01089	9465.22	41.47994	9446.20	65.54457	9460.32
0.264381	9471.10	13.01438	9465.18	41.58569	9446.22	65.74930	9460.34
0.267879	9471.00	13.01929	9465.10	41.74091	9446.14	66.00703	9460.30
0.271376	9470.92	13.02650	9464.84	41.96874	9446.02	66.33150	9460.44
0.278371	9470.92	13.03707	9464.76	42.30314	9445.90	66.73999	9460.48
0.285366	9471.00	13.05259	9464.64	42.79398	9445.62	67.25424	9460.72
0.293517	9470.96	13.07537	9464.46	43.51443	9445.46	67.90164	9460.82
0.303777	9470.82	13.10882	9464.38	44.57191	9445.12	67.95277	9460.76
0.316695	9470.82	13.15790	9464.24	46.12408	9444.62	68.00389	9460.80
0.332957	9470.94	13.22994	9464.24	48.40235	9443.80	68.00739	9447.96
0.353429	9470.88	13.33569	9464.26	51.74639	9442.68	68.01089	9447.62
0.379203	9470.74	13.49091	9464.28	55.24389	9441.72	68.01438	9447.34
0.411650	9470.80	13.71874	9464.18	58.74139	9440.56	68.01788	9447.18
0.452499	9470.84	14.05314	9464.10	63.49639	9439.42	68.02138	9446.90
0.503924	9470.74	14.54398	9463.98	64.75389	9439.14	68.02837	9446.84
0.568664	9470.82	15.26443	9463.82	64.75739	9456.86	68.03537	9446.56
0.650167	9470.90	16.32191	9463.66	64.76089	9457.50	68.04352	9446.36
0.752774	9470.84	17.87408	9463.36	64.76438	9457.84	68.05378	9446.22
0.881948	9470.76	20.15235	9463.04	64.76788	9458.08	68.06670	9446.02
1.044568	9470.70	23.49639	9462.44	64.77138	9458.16	68.08296	9445.78
1.249295	9470.78	26.99389	9461.96	64.77837	9458.46	68.10343	9445.66
1.507031	9470.74	30.49139	9461.58	64.78537	9458.78	68.12920	9445.64
1.831501	9470.70	37.48639	9460.50	64.79352	9459.06	68.16165	9445.62
2.239985	9470.82	41.11889	9460.08	64.80378	9459.16	68.20250	9445.42
2.754236	9470.70	41.25389	9460.10	64.81670	9459.42	68.25392	9445.40
3.401639	9470.62	41.25739	9448.14	64.83296	9459.74	68.31867	9445.36
4.216671	9470.68	41.26089	9447.84	64.85343	9459.94	68.40017	9445.42
5.242737	9470.60	41.26438	9447.52	64.87920	9459.90	68.50277	9445.36
6.534476	9470.66	41.26929	9447.30	64.91165	9460.02	68.63195	9445.34
8.160680	9470.52	41.27650	9447.18	64.95250	9460.08	68.79457	9445.24
10.20795	9470.52	41.28707	9446.98	65.00392	9460.14	68.99930	9445.20
12.78531	9470.46	41.30259	9446.78	65.06867	9460.24	69.25703	9445.26
12.89460	9470.46	41.32537	9446.52	65.15017	9460.30	69.58150	9445.18

Cont.

t, hr	p_{ws}, *psia*	*t, hr*	p_{ws}, *psia*	*t, hr*	p_{ws}, *psia*	*t, hr*	p_{ws}, *psia*
69.98999	9445.16	75.46874	9422.82	82.96874	9444.74	97.6579	9412.44
70.50424	9445.08	75.80314	9422.68	83.30314	9444.76	97.72994	9412.42
71.15164	9444.92	76.29398	9422.32	83.52852	9444.76	97.83569	9412.40
71.64481	9444.78	77.01443	9422.04	83.75389	9444.72	97.99091	9412.34
71.75389	9444.76	78.07191	9421.68	83.75739	9422.14	98.21874	9412.34
71.75739	9429.18	79.62408	9420.98	83.76089	9421.56	98.55314	9412.08
71.76089	9428.84	81.00389	9420.32	83.76438	9421.22	99.04398	9412.04
71.76438	9428.68	81.00739	9434.18	83.76929	9421.00	99.76443	9411.70
71.76929	9428.44	81.01089	9434.44	83.77650	9420.76	100.8219	9411.28
71.77650	9428.28	81.01438	9434.56	83.78707	9420.38	102.3741	9410.80
71.78707	9428.12	81.01929	9434.78	83.80259	9420.06	104.6523	9410.02
71.80259	9427.74	81.02650	9434.92	83.82537	9419.86	107.9964	9408.98
71.82537	9427.54	81.03707	9435.18	83.85882	9419.46	111.4939	9407.76
71.85882	9427.34	81.05259	9435.26	83.90790	9419.26	114.9914	9406.56
71.90790	9427.38	81.07537	9435.50	83.97994	9419.18	119.1191	9405.34
71.97994	9427.18	81.10882	9435.56	84.08569	9419.26	119.7494	9405.20
72.08569	9427.06	81.15790	9435.64	84.24091	9419.18	119.7529	9438.20
72.24091	9427.06	81.22994	9435.68	84.46874	9419.06	119.7564	9439.04
72.46874	9427.04	81.33569	9435.58	84.80314	9418.86	119.7599	9439.52
72.80314	9426.78	81.49091	9435.56	85.29398	9418.72	119.7634	9440.06
73.29398	9426.72	81.71874	9435.66	86.01443	9418.32	119.7669	9440.28
74.01443	9426.26	82.05314	9435.52	87.07191	9418.02	119.7739	9440.68
74.75389	9426.00	82.25389	9435.56	88.62408	9417.30	119.7809	9441.14
74.75739	9423.28	82.25739	9443.64	90.90235	9416.44	119.7890	9441.36
74.76089	9423.28	82.26089	9443.82	94.24639	9415.12	119.7993	9441.76
74.76438	9423.18	82.26438	9443.84	95.87514	9414.58	119.8122	9442.06
74.76929	9423.18	82.26929	9444.06	97.50389	9414.02	119.8285	9442.44
74.77650	9423.32	82.27650	9444.08	97.50739	9412.72	119.8489	9442.78
74.78707	9423.24	82.28707	9444.28	97.51089	9412.56	119.8747	9442.96
74.80259	9423.10	82.30259	9444.32	97.51438	9412.56	119.9072	9443.04
74.82537	9423.20	82.32537	9444.50	97.51929	9412.68	119.9480	9443.24
74.85882	9423.08	82.35882	9444.56	97.52650	9412.66	119.9994	9443.20
74.90790	9423.08	82.40790	9444.62	97.53707	9412.52	120.0642	9443.36
74.97994	9422.94	82.47994	9444.70	97.55259	9412.64	120.1457	9443.24
75.08569	9422.96	82.58569	9444.72	97.57537	9412.62	120.2483	9443.30
75.24091	9422.84	82.74091	9444.62	97.60882	9412.58	120.3775	9443.36

Cont.

t, hr	p_{ws}, *psia*	*t, hr*	p_{ws}, *psia*	*t, hr*	p_{ws}, *psia*	*t, hr*	p_{ws}, *psia*
120.5401	9443.56	129.8315	9436.98	132.0109	9406.86	135.0265	9402.42
120.7448	9443.56	129.9177	9436.96	132.0144	9406.90	135.0371	9402.38
121.0025	9443.62	130.0039	9437.06	132.0193	9406.86	135.0526	9402.30
121.3270	9443.82	130.0074	9422.56	132.0265	9406.62	135.0754	9402.28
121.7355	9443.90	130.0109	9422.40	132.0371	9406.58	135.1088	9402.24
122.2497	9444.14	130.0144	9422.18	132.0526	9406.46	135.1579	9402.34
122.8972	9444.38	130.0193	9421.92	132.0754	9406.52	135.2300	9402.14
123.7122	9444.64	130.0265	9421.76	132.1088	9406.34	135.3357	9402.26
124.7382	9444.96	130.0371	9421.48	132.1579	9406.28	135.4909	9402.16
126.0300	9445.38	130.0526	9421.26	132.2300	9406.32	135.5039	9402.18
127.6562	9445.76	130.0754	9421.00	132.3357	9406.30	135.5074	9399.26
127.955	9445.78	130.1088	9420.90	132.4909	9406.12	135.5109	9399.04
128.2539	9445.96	130.1579	9420.70	132.7187	9406.10	135.5144	9399.14
128.2574	9438.56	130.2300	9420.70	133.0532	9405.98	135.5193	9399.02
128.2609	9438.28	130.3357	9420.54	133.2539	9405.80	135.5265	9399.00
128.2644	9438.16	130.4909	9420.58	133.2574	9405.20	135.5371	9399.08
128.2679	9438.04	130.7187	9420.46	133.2609	9405.24	135.5526	9398.98
128.2714	9438.04	131.0532	9420.30	133.2644	9405.36	135.5754	9398.84
128.2784	9437.82	131.2539	9420.34	133.2693	9405.30	135.6088	9398.92
128.2854	9437.58	131.2574	9415.10	133.2765	9405.18	135.6579	9398.80
128.2935	9437.62	131.2609	9414.94	133.2871	9405.32	135.7300	9398.72
128.3038	9437.44	131.2644	9414.84	133.3026	9405.26	135.8357	9398.82
128.3167	9437.40	131.2693	9414.68	133.3254	9405.24	135.9909	9398.66
128.3330	9437.22	131.2765	9414.76	133.3588	9405.24	136.2187	9398.66
128.3534	9437.08	131.2871	9414.70	133.4079	9405.24	136.5532	9398.52
128.3792	9437.12	131.3026	9414.58	133.4800	9405.24	137.0440	9398.30
128.4117	9436.96	131.3254	9414.58	133.5857	9405.06	137.7644	9397.82
128.4525	9436.90	131.3588	9414.42	133.7409	9405.04	138.8219	9397.44
128.5039	9436.96	131.4079	9414.40	133.9687	9404.88	139.7539	9397.12
128.5687	9436.90	131.4800	9414.32	134.3032	9404.86	139.7574	9389.76
128.6502	9436.86	131.5857	9414.30	134.7940	9404.58	139.7609	9389.64
128.7528	9437.02	131.7409	9414.36	135.0039	9404.48	139.7644	9389.66
128.882	9436.96	131.9687	9414.14	135.0074	9402.44	139.7693	9389.48
129.0446	9436.90	131.9863	9414.16	135.0109	9402.46	139.7765	9389.56
129.2493	9436.94	132.0039	9414.24	135.0144	9402.40	139.7871	9389.40
129.5070	9437.04	132.0074	9406.98	135.0193	9402.48	139.8026	9389.34

Cont.

t, hr	*p_{ws}, psia*	*t, hr*	*p_{ws}, psia*	*t, hr*	*p_{ws}, psia*	*t, hr*	*p_{ws}, psia*
139.8254	9389.22	151.0265	9378.84	155.3026	9366.56	158.1579	9357.70
139.8588	9389.08	151.0371	9378.72	155.3254	9366.50	158.2300	9357.66
139.9079	9389.12	151.0526	9378.62	155.3588	9366.56	158.3357	9357.52
139.9800	9389.04	151.0754	9378.68	155.4079	9366.44	158.4909	9357.50
140.0857	9388.92	151.1088	9378.62	155.4800	9366.36	158.7187	9357.36
140.2409	9388.98	151.1579	9378.58	155.5857	9366.32	159.0532	9357.18
140.4687	9388.88	151.2300	9378.44	155.7409	9366.16	159.5440	9356.82
140.8032	9388.68	151.3357	9378.40	155.9687	9366.20	160.2644	9356.40
141.2940	9388.42	151.4909	9378.34	156.3032	9365.90	161.3219	9355.86
142.0144	9388.16	151.7187	9378.24	156.5285	9365.86	161.5039	9355.66
143.0719	9387.62	152.0532	9378.22	156.7539	9365.76	161.5074	9423.36
144.6241	9386.90	152.5440	9377.82	156.7574	9361.92	161.5109	9424.90
146.9024	9385.70	153.0039	9377.64	156.7609	9361.94	161.5144	9425.60
148.3281	9385.08	153.0074	9373.42	156.7644	9361.80	161.5179	9426.22
149.7539	9384.44	153.0109	9373.42	156.7693	9361.78	161.5214	9426.62
149.7574	9382.82	153.0144	9373.48	156.7765	9361.88	161.5284	9427.34
149.7609	9382.88	153.0193	9373.38	156.7871	9361.82	161.5354	9428.02
149.7644	9382.76	153.0265	9373.26	156.8026	9361.74	161.5435	9428.46
149.7693	9382.76	153.0371	9373.30	156.8254	9361.76	161.5538	9429.18
149.7765	9382.84	153.0526	9373.26	156.8588	9361.66	161.5667	9429.60
149.7871	9382.74	153.0754	9373.16	156.9079	9361.60	161.5830	9430.18
149.8026	9382.76	153.1088	9373.06	156.9800	9361.64	161.6034	9430.46
149.8254	9382.68	153.1579	9373.16	157.0857	9361.58	161.6292	9430.86
149.8588	9382.72	153.2300	9373.10	157.2409	9361.34	161.6617	9431.00
149.9079	9382.60	153.3357	9373.04	157.4687	9361.26	161.7025	9431.32
149.9800	9382.70	153.4909	9372.94	157.8032	9361.14	161.7539	9431.40
150.0857	9382.58	153.7187	9372.86	158.0039	9361.06	161.8187	9431.44
150.2409	9382.48	154.0532	9372.60	158.0074	9358.06	161.9002	9431.42
150.4687	9382.44	154.5440	9372.34	158.0109	9357.86	162.0028	9431.52
150.8032	9382.30	155.2539	9372.08	158.0144	9357.94	162.1320	9431.46
150.9035	9382.20	155.2574	9366.98	158.0193	9357.82	162.2946	9431.54
151.0039	9382.22	155.2609	9366.74	158.0265	9357.88	162.4993	9431.80
151.0074	9378.86	155.2644	9366.82	158.0371	9357.76	162.7570	9431.82
151.0109	9378.92	155.2693	9366.66	158.0526	9357.70	163.0815	9432.02
151.0144	9378.90	155.2765	9366.60	158.0754	9357.68	163.2539	9432.00
151.0193	9378.88	155.2871	9366.58	158.1088	9357.62	163.2574	9412.44

Cont.

t, hr	p_{ws}, *psia*	*t, hr*	p_{ws}, *psia*	*t, hr*	p_{ws}, *psia*	*t, hr*	p_{ws}, *psia*
163.2609	9411.82	165.8357	9357.88	182.0754	9306.26	254.1617	9380.08
163.2644	9411.62	165.9909	9357.76	182.1088	9306.14	254.2025	9380.24
163.2679	9411.28	166.2187	9357.70	182.1579	9306.12	254.2539	9380.32
163.2714	9411.16	166.5532	9357.58	182.2300	9306.04	254.3187	9380.32
163.2784	9410.78	167.0440	9357.12	182.3357	9305.90	254.4002	9380.54
163.2854	9410.54	167.2539	9357.10	182.4909	9305.82	254.5028	9380.54
163.2935	9410.24	167.2574	9334.02	182.7187	9305.60	254.6320	9380.68
163.3038	9410.12	167.2609	9333.48	183.0532	9305.42	254.7946	9380.86
163.3167	9409.86	167.2644	9333.44	183.5440	9304.98	254.9993	9381.12
163.3330	9409.58	167.2693	9333.24	184.2644	9304.42	255.2570	9381.30
163.3534	9409.36	167.2765	9332.96	185.3219	9303.74	255.5815	9381.50
163.3792	9409.24	167.2871	9332.88	186.8741	9302.56	255.9900	9381.96
163.4117	9409.08	167.3026	9332.66	189.1524	9301.10	256.5042	9382.34
163.4525	9409.00	167.3254	9332.50	192.4964	9298.72	257.1517	9382.88
163.5039	9409.08	167.3588	9332.30	195.9939	9296.62	257.9667	9383.50
163.5687	9409.04	167.4079	9332.12	199.4914	9294.38	258.9927	9384.38
163.6502	9408.96	167.4800	9332.18	206.4864	9290.18	260.2845	9385.32
163.7528	9409.02	167.5857	9332.08	213.4814	9286.16	261.9107	9386.38
163.8820	9409.06	167.7409	9331.88	223.9739	9280.34	263.9580	9387.74
164.0446	9409.04	167.9687	9331.78	234.4664	9275.10	266.5353	9389.34
164.2493	9409.12	168.3032	9331.52	248.4564	9268.26	269.7800	9391.08
164.5070	9409.08	168.7940	9331.06	252.9789	9266.24	273.8649	9393.20
164.8315	9408.96	169.5144	9330.60	254.0039	9265.62	279.0074	9395.54
165.2400	9409.00	170.5719	9329.72	254.0074	9369.48	285.4814	9398.10
165.5039	9408.94	172.1241	9328.60	254.0109	9371.92	295.9739	9401.52
165.5074	9362.36	174.4024	9326.96	254.0144	9372.98	306.4664	9404.50
165.5109	9361.44	177.7464	9324.68	254.0179	9373.58	320.4564	9407.60
165.5144	9361.02	181.2439	9322.54	254.0214	9374.24	337.9439	9410.54
165.5193	9360.70	182.0039	9321.98	254.0284	9375.16	350.0039	9412.08
165.5265	9360.16	182.0074	9307.40	254.0354	9375.96		
165.5371	9359.74	182.0109	9306.82	254.0435	9376.74		
165.5526	9359.30	182.0144	9306.84	254.0538	9377.42		
165.5754	9358.68	182.0193	9306.60	254.0667	9378.04		
165.6088	9358.40	182.0265	9306.58	254.0830	9378.72		
165.6579	9358.18	182.0371	9306.38	254.1034	9379.34		
165.7300	9358.02	182.0526	9306.38	254.1292	9379.76		

Table E.0.4. Pseudopressure derivative data for buildup 1.

Field data for buildup 1				**Analytical model data for build up 1**		
Δt, hr	***m(p)-m(p@Δt=0), psi²/cp***	***Derivative, psi²/cp***		***Δt, hr***	***m(p)-m(p@Δt=0), psi²/cp***	***Derivative, psi²/cp***
0.003498	2.07E+07	1.14E+06		0.003525	2.19E+07	9.33E+05
0.006995	2.14E+07	1.01E+06		0.007050	2.26E+07	9.71E+05
0.010493	2.18E+07	9.76E+05		0.010576	2.30E+07	1.00E+06
0.013990	2.21E+07	6.61E+05		0.014101	2.33E+07	1.05E+06
0.017488	2.22E+07	6.67E+05		0.017752	2.35E+07	1.10E+06
0.024483	2.25E+07	1.30E+06		0.022348	2.38E+07	1.15E+06
0.031478	2.29E+07	1.45E+06		0.028135	2.41E+07	1.21E+06
0.039628	2.32E+07	9.64E+05		0.035420	2.44E+07	1.25E+06
0.049888	2.34E+07	9.14E+05		0.044591	2.46E+07	1.26E+06
0.062806	2.37E+07	1.47E+06		0.056137	2.49E+07	1.21E+06
0.079068	2.40E+07	1.32E+06		0.070672	2.52E+07	1.10E+06
0.099541	2.43E+07	4.06E+05		0.088971	2.54E+07	9.32E+05
0.125314	2.42E+07	2.04E+05		0.112007	2.56E+07	7.32E+05
0.157761	2.44E+07	4.58E+05		0.141009	2.58E+07	5.28E+05
0.198610	2.44E+07	3.06E+05		0.177520	2.59E+07	3.51E+05
0.250035	2.45E+07	4.09E+05		0.223484	2.59E+07	2.21E+05
0.314775	2.46E+07	4.09E+05		0.281350	2.60E+07	1.43E+05
0.396278	2.47E+07	-52343.1		0.354198	2.60E+07	1.12E+05
0.498885	2.46E+07	53147.96		0.445909	2.60E+07	1.13E+05
0.628059	2.47E+07	2.57E+05		0.561366	2.61E+07	1.36E+05
0.790679	2.47E+07	52243.26		0.706718	2.61E+07	1.72E+05
0.995406	2.47E+07	-53388.3		0.889706	2.61E+07	2.19E+05
1.253142	2.47E+07	2.68E+05		1.120073	2.62E+07	2.76E+05
1.577612	2.48E+07	4.76E+05		1.410088	2.63E+07	3.47E+05
1.986096	2.49E+07	7.62E+05		1.775196	2.63E+07	4.33E+05
2.500347	2.52E+07	9.24E+05		2.234839	2.64E+07	5.40E+05
3.147750	2.53E+07			2.813496	2.66E+07	6.68E+05
				3.044627	2.66E+07	

Table E.0.5. Pseudopressure derivative data for buildup 2.

Field data for buildup 2				Analytical model data for build up 2		
Δt, hr	***m(p)-m(p@Δt=0), psi^2/cp***	***Derivative, psi^2/cp***		***Δt, hr***	***m(p)-m(p@Δt=0), psi^2/cp***	***Derivative, psi^2/cp***
0.003498	2.56E+07	9.59E+05		0.003525	2.72E+07	9.85E+05
0.006995	2.63E+07	9.32E+05		0.007050	2.79E+07	9.92E+05
0.010493	2.67E+07	1.24E+06		0.010576	2.83E+07	1.02E+06
0.013990	2.71E+07	1.07E+06		0.014101	2.86E+07	1.06E+06
0.017488	2.73E+07	8.32E+05		0.017752	2.88E+07	1.11E+06
0.024483	2.76E+07	1.21E+06		0.022348	2.91E+07	1.16E+06
0.031478	2.79E+07	1.07E+06		0.028135	2.93E+07	1.22E+06
0.039628	2.81E+07	1.05E+06		0.035420	2.96E+07	1.26E+06
0.049888	2.84E+07	1.19E+06		0.044591	2.99E+07	1.26E+06
0.062806	2.86E+07	1.15E+06		0.056137	3.02E+07	1.21E+06
0.079068	2.89E+07	1.22E+06		0.070672	3.05E+07	1.10E+06
0.099541	2.92E+07	8.82E+05		0.088971	3.07E+07	9.40E+05
0.125314	2.93E+07	4.41E+05		0.112007	3.09E+07	7.41E+05
0.157761	2.94E+07	4.76E+05		0.141009	3.11E+07	5.39E+05
0.198610	2.96E+07	2.72E+05		0.177520	3.12E+07	3.64E+05
0.250035	2.95E+07	2.04E+05		0.223484	3.12E+07	2.37E+05
0.314775	2.97E+07	6.75E+04		0.281350	3.13E+07	1.63E+05
0.396278	2.96E+07	-1.02E+05		0.354198	3.13E+07	1.36E+05
0.498885	2.96E+07	2.05E+05		0.445909	3.13E+07	1.44E+05
0.628059	2.97E+07	4.46E+05		0.561366	3.14E+07	1.74E+05
0.790679	2.98E+07	3.42E+05		0.706718	3.14E+07	2.20E+05
0.995406	2.98E+07	1.04E+05		0.889706	3.15E+07	2.78E+05
1.253142	2.99E+07	4.51E+05		1.120073	3.15E+07	3.50E+05
1.577612	3.00E+07	4.86E+05		1.410088	3.16E+07	4.38E+05
1.986096	3.01E+07	5.62E+05		1.775196	3.17E+07	5.46E+05
2.500347	3.03E+07	8.48E+05		2.234839	3.19E+07	6.78E+05
3.147750	3.05E+07	8.92E+05		2.813496	3.20E+07	8.39E+05
3.962783	3.07E+07	1.05E+06		3.541982	3.22E+07	1.04E+06
4.988848	3.09E+07	1.36E+06		4.459091	3.25E+07	1.27E+06
6.280587	3.12E+07	1.50E+06		5.613663	3.28E+07	1.56E+06
7.906791	3.15E+07			7.067182	3.31E+07	1.89E+06
8.205645	3.15E+07			7.819544	3.33E+07	

Table E.0.6. Pseudopressure derivative data for buildup 3.

Field data for buildup 3				Analytical model data for build up 3		
Δt, hr	***m(p)-m(p@Δt=0), psi²/cp***	***Derivative, psi²/cp***		***Δt, hr***	***m(p)-m(p@Δt=0), psi²/cp***	***Derivative, psi²/cp***
0.003498	3.40E+07	1.27E+06		0.003525	3.60E+07	1.25E+06
0.006995	3.48E+07	9.60E+05		0.007050	3.68E+07	1.06E+06
0.010493	3.52E+07	9.94E+05		0.010576	3.72E+07	1.03E+06
0.013990	3.55E+07	9.81E+05		0.014101	3.75E+07	1.07E+06
0.017488	3.57E+07	9.71E+05		0.017752	3.78E+07	1.12E+06
0.024483	3.60E+07	1.24E+06		0.022348	3.80E+07	1.18E+06
0.031478	3.64E+07	1.15E+06		0.028135	3.83E+07	1.23E+06
0.039628	3.66E+07	1.27E+06		0.035420	3.86E+07	1.27E+06
0.049888	3.70E+07	1.25E+06		0.044591	3.89E+07	1.27E+06
0.062806	3.72E+07	1.09E+06		0.056137	3.92E+07	1.22E+06
0.079068	3.75E+07	9.42E+05		0.070672	3.94E+07	1.11E+06
0.099541	3.76E+07	7.46E+05		0.088971	3.97E+07	9.44E+05
0.125314	3.78E+07	5.93E+05		0.112007	3.99E+07	7.42E+05
0.157761	3.79E+07	5.06E+05		0.141009	4.00E+07	5.37E+05
0.198610	3.80E+07	4.40E+05		0.177520	4.01E+07	3.59E+05
0.250035	3.81E+07	1.32E+05		0.223484	4.02E+07	2.28E+05
0.314775	3.81E+07	2.19E+04		0.281350	4.02E+07	1.50E+05
0.396278	3.81E+07	8.95E+04		0.354198	4.03E+07	1.19E+05
0.498885	3.81E+07	4.38E+04		0.445909	4.03E+07	1.23E+05
0.628059	3.81E+07	2.35E+04		0.561366	4.03E+07	1.48E+05
0.790679	3.82E+07	3.86E+05		0.706718	4.03E+07	1.88E+05
0.995406	3.83E+07	3.17E+05		0.889706	4.04E+07	2.40E+05
1.253142	3.83E+07	2.56E+05		1.120073	4.05E+07	3.04E+05
1.577612	3.84E+07	7.12E+04		1.410088	4.05E+07	3.81E+05
1.750000	3.84E+07			1.586979	4.06E+07	4.27E+05
				1.763870	4.06E+07	

Table E.0.7. Pseudopressure derivative data for buildup 4.

Field data for buildup 4				Analytical model data for build up 4		
Δt, hr	***m(p)-m(p@Δt=0), psi²/cp***	***Derivative, psi²/cp***		***Δt, hr***	***m(p)-m(p@Δt=0), psi²/cp***	***Derivative, psi²/cp***
0.003498	4.03E+07	1.60E+06		0.003525	4.26E+07	1.78E+06
0.006995	4.13E+07	1.15E+06		0.007050	4.36E+07	1.19E+06
0.010493	4.17E+07	9.00E+05		0.010576	4.41E+07	1.04E+06
0.013990	4.19E+07	1.01E+06		0.014101	4.44E+07	1.08E+06
0.017488	4.22E+07	1.12E+06		0.017752	4.46E+07	1.13E+06
0.024483	4.26E+07	1.17E+06		0.022348	4.49E+07	1.19E+06
0.031478	4.29E+07	1.28E+06		0.028135	4.52E+07	1.24E+06
0.039628	4.32E+07	1.24E+06		0.035420	4.55E+07	1.28E+06
0.049888	4.34E+07	1.10E+06		0.044591	4.57E+07	1.28E+06
0.062806	4.37E+07	1.10E+06		0.056137	4.60E+07	1.23E+06
0.079068	4.39E+07	1.10E+06		0.070672	4.63E+07	1.12E+06
0.099541	4.42E+07	8.82E+05		0.088971	4.66E+07	9.55E+05
0.125314	4.43E+07	6.28E+05		0.112007	4.68E+07	7.55E+05
0.157761	4.45E+07	4.07E+05		0.141009	4.69E+07	5.52E+05
0.198610	4.45E+07	2.04E+05		0.177520	4.70E+07	3.77E+05
0.250035	4.46E+07	6.79E+04		0.223484	4.71E+07	2.51E+05
0.314775	4.46E+07	1.87E+05		0.281350	4.71E+07	1.79E+05
0.396278	4.47E+07	1.87E+05		0.354198	4.72E+07	1.56E+05
0.498885	4.47E+07	1.19E+05		0.445909	4.72E+07	1.69E+05
0.628059	4.47E+07	2.73E+05		0.561366	4.72E+07	2.05E+05
0.790679	4.48E+07	3.76E+05		0.706718	4.73E+07	2.59E+05
0.995406	4.49E+07	3.76E+05		0.889706	4.74E+07	3.27E+05
1.253142	4.49E+07	3.26E+05		1.120073	4.74E+07	4.10E+05
1.577612	4.50E+07	5.68E+05		1.410088	4.75E+07	5.12E+05
1.986096	4.52E+07	7.24E+05		1.775196	4.77E+07	6.37E+05
2.500347	4.54E+07	7.97E+05		2.234839	4.78E+07	7.89E+05
3.147750	4.56E+07	1.01E+06		2.813496	4.80E+07	9.75E+05
3.962783	4.58E+07	1.32E+06		3.541982	4.83E+07	1.20E+06
4.988848	4.62E+07	1.61E+06		4.459091	4.86E+07	1.47E+06
6.280587	4.65E+07	1.79E+06		5.613663	4.89E+07	1.79E+06
7.906791	4.69E+07	2.19E+06		7.067182	4.94E+07	2.17E+06
9.954060	4.75E+07	2.72E+06		8.897055	4.99E+07	2.60E+06
12.531419	4.81E+07	3.13E+06		11.200729	5.05E+07	3.10E+06
15.776122	4.88E+07	3.71E+06		14.100883	5.12E+07	3.66E+06
19.860960	4.96E+07	4.41E+06		17.626103	5.19E+07	4.25E+06
25.003468	5.05E+07	5.02E+06		21.151324	5.27E+07	4.78E+06
31.477501	5.15E+07	5.64E+06		24.676545	5.33E+07	5.24E+06
41.970001	5.28E+07	6.69E+06		28.201765	5.39E+07	5.65E+06
52.462502	5.40E+07	7.35E+06		31.726986	5.45E+07	6.02E+06

Field data for buildup 4		
Δt, hr	***m(p)-m(p@Δt=0), psi²/cp***	***Derivative, psi²/cp***
66.452502	5.52E+07	7.67E+06
83.940003	5.64E+07	7.69E+06
96.000000	5.70E+07	

Analytical model data for build up 4		
Δt, hr	***m(p)-m(p@Δt=0), psi²/cp***	***Derivative, psi²/cp***
35.252207	5.50E+07	6.35E+06
38.777427	5.54E+07	6.64E+06
42.302648	5.59E+07	6.90E+06
45.827869	5.63E+07	7.14E+06
49.353089	5.67E+07	7.35E+06
52.878310	5.71E+07	7.55E+06
56.403531	5.74E+07	7.71E+06
59.928751	5.77E+07	7.86E+06
63.453972	5.80E+07	7.98E+06
66.979193	5.83E+07	8.07E+06
70.504413	5.86E+07	8.15E+06
74.029634	5.88E+07	8.22E+06
77.554855	5.91E+07	8.25E+06
81.080075	5.93E+07	8.29E+06
84.605296	5.95E+07	8.32E+06
88.130517	5.97E+07	8.34E+06
91.655738	5.99E+07	8.36E+06
95.180958	6.01E+07	

Table E.0.8. Semilog analysis data for buildup 1.

Field data for buildup 1		Analytical model data for build up 1	
Log of superposition time	**m(p), psi²/cp**	**Log of superposition time**	**m(p), psi²/cp**
-3.987697	2.07E+07	-3.987697	2.08E+07
-3.686716	2.14E+07	-3.686716	2.14E+07
-3.510673	2.18E+07	-3.510673	2.18E+07
-3.385783	2.21E+07	-3.385783	2.21E+07
-3.288921	2.22E+07	-3.285833	2.24E+07
-3.142890	2.25E+07	-3.185896	2.26E+07
-3.033843	2.29E+07	-3.085976	2.29E+07
-2.933955	2.32E+07	-2.986076	2.32E+07
-2.834097	2.34E+07	-2.886202	2.35E+07
-2.734276	2.37E+07	-2.786360	2.38E+07
-2.634501	2.40E+07	-2.686560	2.40E+07
-2.534784	2.43E+07	-2.586811	2.43E+07
-2.435140	2.42E+07	-2.487127	2.44E+07
-2.335587	2.44E+07	-2.387524	2.46E+07
-2.236150	2.44E+07	-2.288023	2.47E+07
-2.136857	2.45E+07	-2.188651	2.48E+07
-2.037746	2.46E+07	-2.089440	2.48E+07
-1.938861	2.47E+07	-1.990430	2.48E+07
-1.840261	2.46E+07	-1.891674	2.48E+07
-1.742016	2.47E+07	-1.793234	2.49E+07
-1.644214	2.47E+07	-1.695189	2.49E+07
-1.546964	2.47E+07	-1.597635	2.49E+07
-1.450397	2.47E+07	-1.500694	2.50E+07
-1.354676	2.48E+07	-1.404509	2.51E+07
-1.259997	2.49E+07	-1.309260	2.52E+07
-1.166592	2.52E+07	-1.215158	2.53E+07
-1.074737	2.53E+07	-1.122457	2.54E+07
		-1.091047	2.54E+07

Table E.0.9. Semilog analysis data for buildup 2.

Field data for buildup 2			Analytical model data for build up 2	
Log of superposition time	**m(p), psi^2/cp**		**Log of superposition time**	**m(p), psi^2/cp**
-4.274373	2.56E+07		-4.274373	2.57E+07
-3.973369	2.63E+07		-3.973369	2.64E+07
-3.797304	2.67E+07		-3.797304	2.68E+07
-3.672391	2.71E+07		-3.672391	2.71E+07
-3.575507	2.73E+07		-3.572418	2.73E+07
-3.429430	2.76E+07		-3.472451	2.76E+07
-3.320337	2.79E+07		-3.372494	2.79E+07
-3.220398	2.81E+07		-3.272547	2.82E+07
-3.120473	2.84E+07		-3.172614	2.85E+07
-3.020569	2.86E+07		-3.072699	2.87E+07
-2.920689	2.89E+07		-2.972805	2.90E+07
-2.820840	2.92E+07		-2.872939	2.93E+07
-2.721030	2.93E+07		-2.773108	2.94E+07
-2.621269	2.94E+07		-2.673320	2.96E+07
-2.521570	2.96E+07		-2.573587	2.97E+07
-2.421948	2.95E+07		-2.473922	2.98E+07
-2.322424	2.97E+07		-2.374345	2.98E+07
-2.223022	2.96E+07		-2.274875	2.98E+07
-2.123773	2.96E+07		-2.175542	2.99E+07
-2.024717	2.97E+07		-2.076380	2.99E+07
-1.925901	2.98E+07		-1.977432	2.99E+07
-1.827386	2.98E+07		-1.878752	3.00E+07
-1.729247	2.99E+07		-1.780406	3.01E+07
-1.631575	3.00E+07		-1.682478	3.02E+07
-1.534485	3.01E+07		-1.585069	3.03E+07
-1.438114	3.03E+07		-1.488303	3.04E+07
-1.342631	3.05E+07		-1.392334	3.06E+07
-1.248236	3.07E+07		-1.297344	3.08E+07
-1.155171	3.09E+07		-1.203553	3.10E+07
-1.063715	3.12E+07		-1.111219	3.13E+07
-0.974193	3.15E+07		-1.020645	3.17E+07
-0.959974	3.15E+07		-0.981494	3.18E+07

Table E.0.10. Semilog analysis data for buildup 3.

Field data for buildup 3		Analytical model data for build up 3	
Log of superposition time	**m(p), psi^2/cp**	**Log of superposition time**	**m(p), psi^2/cp**
-4.076603	3.40E+07	-4.076603	3.41E+07
-3.775648	3.48E+07	-3.775648	3.49E+07
-3.599632	3.52E+07	-3.599632	3.53E+07
-3.474768	3.55E+07	-3.474768	3.56E+07
-3.377933	3.57E+07	-3.374846	3.58E+07
-3.231955	3.60E+07	-3.274943	3.61E+07
-3.122960	3.64E+07	-3.175066	3.64E+07
-3.023134	3.66E+07	-3.075220	3.67E+07
-2.923353	3.70E+07	-2.975415	3.69E+07
-2.823628	3.72E+07	-2.875659	3.72E+07
-2.723973	3.75E+07	-2.775966	3.75E+07
-2.624407	3.76E+07	-2.676351	3.77E+07
-2.524952	3.78E+07	-2.576835	3.79E+07
-2.425635	3.79E+07	-2.477442	3.81E+07
-2.326492	3.80E+07	-2.378203	3.82E+07
-2.227563	3.81E+07	-2.279157	3.83E+07
-2.128903	3.81E+07	-2.180349	3.83E+07
-2.030575	3.81E+07	-2.081839	3.83E+07
-1.932656	3.81E+07	-1.983696	3.83E+07
-1.835240	3.81E+07	-1.886005	3.84E+07
-1.738441	3.82E+07	-1.788869	3.84E+07
-1.642390	3.83E+07	-1.692409	3.85E+07
-1.547241	3.83E+07	-1.596769	3.85E+07
-1.453173	3.84E+07	-1.502114	3.86E+07
-1.411212	3.84E+07	-1.453975	3.86E+07
		-1.411212	3.87E+07

Table E.0.11. Semilog analysis data for buildup 4.

Field data for buildup 4		Analytical model data for build up 4	
Log of superposition time	**m(p), psi^2/cp**	**Log of superposition time**	**m(p), psi^2/cp**
-4.571115	4.03E+07	-4.571115	4.03E+07
-4.270098	4.13E+07	-4.270098	4.14E+07
-4.094019	4.17E+07	-4.094019	4.18E+07
-3.969093	4.19E+07	-3.969093	4.21E+07
-3.872196	4.22E+07	-3.869106	4.23E+07
-3.726094	4.26E+07	-3.769123	4.26E+07
-3.616975	4.29E+07	-3.669144	4.29E+07
-3.517004	4.32E+07	-3.569171	4.32E+07
-3.417042	4.34E+07	-3.469204	4.35E+07
-3.317089	4.37E+07	-3.369246	4.38E+07
-3.217149	4.39E+07	-3.269298	4.40E+07
-3.117224	4.42E+07	-3.169365	4.43E+07
-3.017318	4.43E+07	-3.069448	4.45E+07
-2.917436	4.45E+07	-2.969554	4.46E+07
-2.817586	4.45E+07	-2.869686	4.47E+07
-2.717773	4.46E+07	-2.769852	4.48E+07
-2.618010	4.46E+07	-2.670062	4.48E+07
-2.518307	4.47E+07	-2.570326	4.49E+07
-2.418681	4.47E+07	-2.470657	4.49E+07
-2.319151	4.47E+07	-2.371074	4.49E+07
-2.219742	4.48E+07	-2.271599	4.50E+07
-2.120484	4.49E+07	-2.172258	4.51E+07
-2.021417	4.49E+07	-2.073086	4.51E+07
-1.922588	4.50E+07	-1.974127	4.53E+07
-1.824057	4.52E+07	-1.875432	4.54E+07
-1.725899	4.54E+07	-1.777069	4.55E+07
-1.628204	4.56E+07	-1.679119	4.57E+07
-1.531086	4.58E+07	-1.581685	4.60E+07
-1.434684	4.62E+07	-1.484890	4.63E+07
-1.339164	4.65E+07	-1.388887	4.66E+07
-1.244730	4.69E+07	-1.293859	4.71E+07
-1.151623	4.75E+07	-1.200027	4.76E+07
-1.060126	4.81E+07	-1.107651	4.82E+07
-0.970568	4.88E+07	-1.017038	4.89E+07
-0.883322	4.96E+07	-0.931235	4.97E+07
-0.798800	5.05E+07	-0.862850	5.04E+07
-0.717447	5.15E+07	-0.806404	5.10E+07
-0.620962	5.28E+07	-0.758637	5.16E+07
-0.550592	5.40E+07	-0.717447	5.22E+07

Field data for buildup 4	
Log of superposition time	m(p), psi^2/cp
-0.480776	5.52E+07
-0.416935	5.64E+07
-0.382685	5.70E+07

Analytical model data for build up 4	
Log of superposition time	m(p), psi^2/cp
-0.681405	5.27E+07
-0.649493	5.32E+07
-0.620962	5.36E+07
-0.595245	5.40E+07
-0.571904	5.44E+07
-0.550592	5.48E+07
-0.531031	5.51E+07
-0.512994	5.54E+07
-0.496294	5.57E+07
-0.480776	5.60E+07
-0.466308	5.63E+07
-0.452779	5.66E+07
-0.440094	5.68E+07
-0.428169	5.70E+07
-0.416935	5.72E+07
-0.406329	5.74E+07
-0.396296	5.76E+07
-0.386788	5.78E+07

APPENDIX F: DEFINITION OF DIMENSIONLESS VARIABLES

The following dimensionless variables are defined for convenience:

The dimensionless pressure:

$$P_D = \frac{kh\Delta P}{141.2 q\mu B}$$

The dimensionless time:

$$t_D = \left(\frac{0.0002637k}{\phi\mu c_t r_w^{\ 2}}\right)t$$

The dimensionless wellbore storage coefficient:

$$C_D = \left(\frac{0.8935}{\phi\mu c_t h r_w^{\ 2}}\right)C$$

The dimensionless derivative of pressure:

$$P_D^{'} = \left(\frac{26.856\phi\mu c_t h r_w^{\ 2}}{qB}\right)\Delta P^{'}$$

The ratio t_D/C_D:

$$\frac{t_D}{C_D} = \left(2.95x10^{-4} \frac{h}{\mu} \right)$$

The dimensionless pressure derivative:

$$t_D P_D^{'} = \left(\frac{kh}{141.2q\mu B} \right) t * \Delta P^{'}$$